

Biomechanical mechanisms of neural tube closure

Young-June Cho

Thesis submitted to University College London for the degree of
Doctor of Philosophy

2015

Developmental Biology of Birth Defects Section
Institute of Child Health
UCL

Declaration

I, Young-June Cho, confirm that the work presented in this thesis is my own.

Where information has been derived from other sources, I confirm that this has been indicated in the thesis.

Abstract

Neural tube defects (NTDs) are amongst the commonest birth defects, affecting 1 in 1000 pregnancies. During neurulation, failure of neural tube closure in the low spinal region (at the posterior neuropore, PNP) results in spina bifida.

Mechanical force relationships in the normally closing neural tube and in the NTD-developing neural tube were investigated through incision of the most recently closed neural tube roof, in order to eliminate tension in the closed region. After incision in wild-type embryos, immediate springing apart (re-opening) of the elevating neural folds was observed, associated with partial relaxation of the bending degree of the Dorsolateral Hinge Points (DLHP) and the Median Hinge Point (MHP) in transverse sections. When incision was performed on *Zic2* mutant embryos developing spina bifida, a larger re-opening of neural folds was observed than in wild-type controls.

These findings coincided with measurements of the elastic modulus of the mutant NPs using Atomic Force Microscopy, which revealed that the dorsal NP of the mutant embryos is stiffer than wild-type. Finite Element Method (FEM) modelling also showed that a larger closing force is required for a stiffer NP.

Moreover, in unincised embryos, nuclei were found to be more elongated in the wild-type NP, where DLHPs are present, than in the mutant NP, where DLHPs are absent, suggesting possible roles of cell packing in DLHP formation.

In conclusion, apposition of the NFs is an elastic process exogenously driven by the force field that originates from the most recently closed point. DLHP formation, however, is a partially plastic process, closely related to cell packing within the dorsal NP as an endogenous event. In *Zic2* mutant embryos, a stiffer NP and the absence of cell-packing in the dorsal NP region are perhaps the main mechanical causes of spinal neurulation failure.

Acknowledgements

I would like to thank my supervisors Andrew Copp, Nicholas Greene, and Guillaume Charras for their kind supervision throughout the Ph.D course. Foremost, my primary supervisor Andrew Copp gave me invaluable help in carrying out the project in the right direction with his extensive expertise. Apart from his academic advices, I would also like to thank him for his generous understanding of difficult situations that I encountered during the course, and his thorough and patient help with English during the thesis writing-up. I am also grateful to my secondary supervisor Nick Green for his helpful advices on the project in addition to Andy's advices. Guillaume Charras, as my secondary supervisor for AFM part of my project, was always willing to sort out numerous technical issues together that arose during the AFM measurement, which I feel deeply thankful for. I would also never forget about his kind effort to make me feel at home in his lab by inviting me to his lab's social events. Ryo Torii in mechanical engineering department is another unforgettable figure that I would like to thank. He gave me enormous help with FEM not even as an officially denominated supervisor as if I was his student.

Ana Rolo in our lab gave me detailed guidance on the project by kindly showing and planning various biological experimental procedures for me. I am also deeply grateful for her time and sharing of expertise in my regular meeting with Andy.

I would like to thank all other BDRC members for their kind sharing of their knowledge and skills. In particular, I thank Dawn Savery for her well-organised maintenance of our mice colonies, and for checking plugs of mice on behalf of me numerous times. Sandra Castro thankfully showed me many miscellaneous lab skills and kept me updated with the latest movie information. I also appreciate Katrin Danielsen for her sharing of GFP constructs whenever it ran out on me.

My last thanks go to my family, who always support me even though they are far away from me.

Overall, I spent invaluable time at BDRC, Institute of Child Health, in cooperative and friendly atmospheres. Among the great people, apart from academic knowledge and experimental skills, I was able to develop communication/interpersonal skills by interacting with many different people from various cultural/academic backgrounds.

Table of contents

Declaration	2
Abstract	3
Acknowledgements	4
Table of contents	5
List of Figures	9
List of Tables	10
Abbreviations	11
1. General introduction	12
1.1. Neural tube formation	12
1.2. Neural tube defects	13
1.3. Changes in morphology of the NP during spinal neurulation	14
1.4. Genetic requirements for neurulation	14
1.5. Molecular regulation of neurulation	16
1.5.1. Planar polarity pathway	16
1.5.2. Signalling pathways that regulate NP bending	17
1.6. Apical constriction in diverse organisms	19
1.7. MHP and cell wedging	21
1.8. Cytoskeletal factors in cell wedging and NP bending	23
1.9. Possible mechanical mechanisms of dorsolateral NP bending	25
1.10. Experimental approaches to understanding the mechanics of morphogenesis	28
1.11. <i>Zic2</i> gene and its role in neurulation	30
1.12. Overview of the thesis	31
2. Material and methods	32
2.1. Mouse embryology	32
2.1.1. <i>Kumba</i> mice	32
2.1.2. Balb/c	33
2.1.3. <i>Grhl3^{cre/+}; ROSA^{YFP/+}</i>	33
2.1.4. Embryo collection	33
2.1.5. Culture technique	33

2.2. DNA and protein methods	34
2.2.1. <i>Kumba</i> genotyping	34
2.2.2. Electroporation.....	35
2.2.3. Immunohistochemistry	36
2.3. Incision techniques.....	37
2.4. Histology and imaging	37
2.4.1. Cryosections.....	37
2.4.2. Paraffin wax sections.....	38
2.4.3. Haematoxylin and eosin staining	39
2.4.4. Imaging	39
2.5. Atomic Force Microscopy (AFM).....	39
2.5.1. Sample preparation	39
2.5.2. Measurement.....	40
2.5.3. Young's modulus calculation.....	40
2.6. Finite Element Modelling (FEM)	41
3. The effects of mechanical manipulation on tissue morphology and cellular shape in the neural plate	44
3.1. Introduction	44
3.1.1. Elastic deformation and force relationships during neural tube closure	44
3.2. Results.....	47
3.2.1. Tissue morphology change after incision.....	47
3.2.2. Cellular shape change after incision	56
3.3. Discussion.....	66
3.3.1. Tissue morphology change after incision.....	66
3.3.2. Cellular shape change after incision	69
4. Tissue and cellular morphologies in spinal neurulation defect developing <i>Zic2</i>^{Ku/Ku}	73
4.1. Introduction	73
4.2. Results.....	75
4.2.1. Tissue morphology differences between <i>Zic2</i> ^{Ku/Ku} and <i>Zic2</i> ^{+/+}	75

4.2.2.	Tissue morphology change after neural tube incision in <i>Zic2^{Ku/Ku}</i> embryos	79
4.2.3.	Cell shape differences between <i>Zic2^{Ku/Ku}</i> and wild-type embryos.....	85
4.3.	Discussion.....	93
4.3.1.	Tissue morphology differences between <i>Zic2^{Ku/Ku}</i> and wild-type.....	93
4.3.2.	Tissue morphology change after incision on <i>Zic2^{Ku/Ku}</i> embryos.....	94
4.3.3.	Cell shape differences between <i>Zic2^{Ku/Ku}</i> and wild-type.....	95
5.	<i>Kumba</i> NP stiffness measurement.....	99
5.1.	Introduction.....	99
5.1.1.	Atomic Force Microscopy working principles.....	99
5.1.2.	Factors affecting stiffness.....	99
5.2.	Results.....	103
5.2.1.	Sample immobilisation method and tissue viability.....	103
5.2.2.	AFM measurement.....	105
5.3.	Discussion.....	110
5.3.1.	Sample immobilising method and tissue viability.....	110
5.3.2.	AFM measurements.....	111
6.	Modelling of neural tube closure using the Finite Element Method (FEM) ...	114
6.1.	Introduction.....	114
6.1.1.	The uses of FEM in understanding neural tube closure.....	114
6.2.	Results.....	116
6.2.1.	Distribution of dorsal closing force along the longitudinal axis and stress profiles during neural tube closure.....	116
6.2.2.	DLHP bending degree change during FEM-simulated closure.....	120
6.2.3.	<i>Kumba</i> morphology and its effect on dorsal closing force.....	122
6.2.4.	Relationship between elasticity and dorsal closing force.....	124
6.3.	Discussion.....	125
7.	General discussion.....	129
7.1.	Summary of the findings.....	129
7.2.	Origin of the NP pull-in force.....	130
7.3.	Motors for continuing closure of the neural tube.....	132

7.4. Mechanical mechanisms of DLHP formation	133
7.5. Molecular basis of the increased stiffness in <i>Kumba</i> mutant embryos	134
7.6. Application of NT closing mechanisms to other morphogeneses	134
7.7. Limitations of the studies.....	135
7.8. Conclusion.....	136
8. Bibliography	137

List of Figures

Figure 1.1. Propagation of closure during neurulation and transverse sections of the PNP at different stages.	15
Figure 1.2. Signalling interactions between Shh, Noggin and Bmp2, and their relations to DLHP formation.	18
Figure 1.3 Interkinetic Nuclear Migration (IKNM) and wedging of cells in MHP.	22
Figure 1.4 Effect of colchicine on wedge-shape cells in the Mexican salamander.	24
Figure 1.5. NP cells in <i>Xenopus</i> morphants lose wedge-shape but hinge points are maintained.	25
Figure 1.6 Spatial distribution of cell cycle-related protein expression during NP bending.	26
Figure 2.1 Schematic of GFP-electroporation in E8.5 embryos	36
Figure 2.2 Example of displacement conditions applied to the modelling.....	43
Figure 3.1 Force relationships in neural tube closure and its corresponding models.....	46
Figure 3.2. The NP springs apart rapidly after incision.	50
Figure 3.3. Dorsal transverse opening varies with incision length, and becomes attenuated caudally along the PNP.	51
Figure 3.4. DLHP bending degree and MHP bending angle reduce after incision.	55
Figure 3.5. Cellular and nuclear shape changes after incision.	58
Figure 3.6. Cell shape becomes less curved after incision particularly in the dorsal NP.	59
Figure 3.7 The relationship between circularity and the Feret diameter of a nucleus	63
Figure 3.8 Nuclear circularity decreases after incision.	64
Figure 3.9 Surface ectoderm in contact with NP reduces in length after incision.	65
Figure 4.1 Morphology difference between <i>Zic2</i> ^{+/+} and <i>Zic2</i> ^{Ku/Ku} E9.5 embryos.	74

Figure 4.2 Morphology of <i>Kumba</i> embryos at the onset of spinal neurulation defect.....	78
Figure 4.3 NF re-opening at previously closing level of <i>Kumba</i> embryos.....	82
Figure 4.4 Curvature of the trunk of <i>Kumba</i> embryos.	84
Figure 4.5 <i>Kumba</i> NP cell curvature.....	88
Figure 4.6 <i>Kumba</i> nuclear circularity and dorsolateral bending degree	92
Figure 5.1. Schematic of AFM working principles and force-distance curve analysis.....	102
Figure 5.2. Schematic of NP immobilisation method and test of NP viability..	104
Figure 5.3 AFM of <i>Kumba</i> embryos: NP region excised and elasticity data	107
Figure 5.4 NP elasticity comparison between ss16-17 and ss18-23 <i>Kumba</i> NP.	109
Figure 6.1 Temporal and spatial profiles of dorsal closing force.....	118
Figure 6.2 Stress profiles during neural tube closure	119
Figure 6.3 DLHP bending degree change in FEM after simulated closure.....	121
Figure 6.4 Effects of variation in basal NP width on the required dorsal closing force.	123
Figure 6.5 Effects of variation in NP thickness on the required dorsal closing force	123
Figure 6.6 Closing forces for NPs with different elasticity values	124
Figure 7.1 Summary diagram of force relationships in <i>Zic2</i> ^{+/+} and <i>Zic2</i> ^{Ku/Ku} embryos.....	131

List of Tables

Table 2.1 Yolk sac circulation and heart beat scoring criteria.....	34
Table 6.1 Comparison of basal NP width, NP thickness, and NP elasticity between measured values, simulation-input, and dorsal closing forces for wild-type and mutant.....	127

Abbreviations

AFM	atomic force microscopy
AIP	anterior intestinal portal
ANOVA	analysis of variance
BMP	bone morphogenetic protein
CD	Cytochalasin D
DAPI	4',6-diamidino-2-phenylindole
DLHP	dorsolateral hinge point
DMEM	Dulbecco's Modified Eagle Medium
dNTP	deoxynucleoside triphosphate
E	embryonic day
ENU	N-ethyl-N-nitrosourea
FEM	finite element method
H&E	haematoxylin and eosin
Hyaluronan	HA
MHP	median hinge point
NFs	neural folds
NP	neural plate
NT	neural tube
NTDs	neural tube defects
PBS	phosphate-buffered saline
PBT	phosphate-buffered saline containing 0.1% Tween-20
PCP	Planer cell polarity
PCR	polymerase chain reaction
PFA	paraformaldehyde
PI	propidium iodide
PNP	posterior neuropore
SE	surface ectoderm
Shh	sonic hedgehog
ss	somite stage

1. General introduction

1.1. Neural tube formation

Neurulation is the process of neural plate bending, which leads to the formation of the neural tube (Schoenwolf and Smith 2000). At the beginning of neurulation, the ectoderm differentiates into the neural plate that undergoes thickening by columnarisation of the epithelial cells. The boundary between the neural plate and the non-neural ectoderm starts to fold bilaterally (i.e. elevation of the neural folds). The apposition of the neural folds in the midline leads to formation of the neural tube, with separation of the neuroepithelium from the surface ectoderm. Subsequently, cells at the boundary between the neural tube and surface ectoderm become neural crest cells, which migrate away from the midline to form a variety of tissue types throughout the embryo (Bronner and LeDouarin 2012).

Neurulation is divided into two phases: primary and secondary neurulation. Primary neurulation is responsible for formation of the whole brain and most of the spinal cord. Closure in mice initiates at the hindbrain/cervical boundary (closure point 1) on embryonic day (E) 8.5, and it proceeds in both caudal and rostral directions (Golden and Chernoff 1993). Two other closure points arise at the forebrain/midbrain boundary (closure 2) and rostral extremity of the forebrain (closure 3), propagating in caudorostral and caudal directions, respectively (Figure 1.1 A) (Golden and Chernoff 1993). The progression of fusion of the neural folds (NFs) forms the anterior neuropore between closure 2 and 3 points, the hindbrain neuropore between closure 2 and closure 1, and the posterior neuropore (PNP) between closure 1 and the caudal extremity of the spinal region. All of the neuropores eventually close, upon completion of primary neurulation along the body axis. In the mouse, PNP closure is completed at approximately E10, around 40 hours after its initiation.

Secondary neurulation occurs at more caudal levels, following closure of the PNP. Stem cell-like mesenchymal cells in the dorsal part of the tail bud condense and form a neuroepithelium with a cavity in the centre (Schoenwolf 1984). The lumen of the secondary neural tube then comes in contact with the lumen of the primary neural tube through 'canalisation', and the sacro-caudal tube develops into the sacral and coccygeal vertebrae. In the mouse embryo, the tail originally contains a secondary neural tube along its entire length, but this degenerates during later development, so there is no

neural tube in the mature tail. In human embryos, not only the neural tube but all other tail tissues degenerate, following completion of secondary neurulation (Lemire 1969).

1.2. Neural tube defects

Failure of primary neurulation at any region along the body axis causes neural tube defects (NTDs), and this happens in humans with a frequency of 1 in 1000 pregnancies worldwide (Mitchell 2005). Failure of closure 1 causes craniorachischisis, the most severe and yet a rare type of NTDs, leaving nearly the entire region of the neural tube open (from midbrain to the lower spinal region). This congenital malformation is lethal in every case. Disruption of closure 2 (cranial region) causes exencephaly, in which the neuroepithelial tissue degenerates because of its continued exposure to the amniotic fluid, leading to anencephaly by late gestation. Anencephaly is accompanied by the absence of a major portion of the skull and brain. Incomplete closure 3 causes a split-face malformation together with anencephaly affecting at least the forebrain.

Spina bifida is a common form of NTD, with a similar frequency as anencephaly; it occurs when spinal neurulation fails to be completed. Spina bifida has three types: myelomeningocele, meningocele, and closed spina bifida. Myelomeningocele is the most common form of spina bifida, in which the spinal cord protrudes through the unclosed caudal region (mostly the lumbosacral region), enclosed by a meningeal sac. Myelomeningocele-affected individuals usually have neuronal disabilities and orthopaedic abnormalities. On the other hand, meningocele involves herniated meninges, not protrusion of the spinal cord, and so results in less severe disabilities than myelomeningocele. Lastly, closed spina bifida (spinal dysraphism) is the mildest condition of spina bifida, where only a small portion of vertebral arches is malformed, without any protrusion of the spinal cord. Since it has normal coverage of skin over the lesion and may be asymptomatic, the diagnosis is easily missed. Sometimes it presents a weakness or urination problems in young children, or sometimes it is an incidental finding when spinal X-rays are taken. Unlike 'open' NTDs that arise from the defects in primary neurulation (e.g. craniorachischisis, anencephaly, and myelomeningocele), closed spina bifida is caused by a defect of secondary neurulation (Copp and Greene 2013).

1.3. Changes in morphology of the NP during spinal neurulation

Transverse sections of the PNP show different morphologies, depending on the rostro-caudal level. At every spinal level, the developing neural plate (NP) progresses from a 'flat' state, at the caudal end of the PNP, where NP bending is being initiated, to an 'elevated' state at the rostral end of the PNP, where the NFs are coming into apposition for completion of closure. In addition, along the body axis, the pattern of bending varies markedly, from upper spine to lower spine, and has been classified into three different 'modes' (Figure 1.1 B): at mode 1 (E8.5), the midline of the NP bends, forming the median hinge point (MHP), and this is the only point of bending in the entire NP; at mode 2 (E9.0-9.5), not only the MHP but also both dorsolateral aspects of the NP bend, forming the dorsolateral hinge points (DLHPs); at mode 3 (E10.0), only DLHPs form, and the MHP is no longer visible (Shum and Copp 1996; Ybot-Gonzalez and Copp 1999).

1.4. Genetic requirements for neurulation

The clinical importance of human NTDs, and the difficulties of studying human embryos during neurulation, has made studies of neural tube closure in mice very popular. Also, there are many close similarities between the neurulation process in mice and humans. More than 240 mouse mutants with NTDs have been described (Harris and Juriloff 2010) demonstrating the need for a large number of genes to ensure normal neurulation. These genes belong to many different molecular pathways, and function in a variety of cellular functions.

Harris and Juriloff (2007) showed that, while 20% of the NTD-associated genes in mice develop exencephaly and/or spina bifida, 70% and 5% develop solely exencephaly or spina bifida, respectively. In their updated report with 50 newly found NTD mutants in mice (Harris and Juriloff 2010), those that develop only exencephaly, were nearly 4 times as frequent as those that develop either spina bifida alone or spina bifida plus exencephaly. In comparison to the striking dominance of exencephaly-

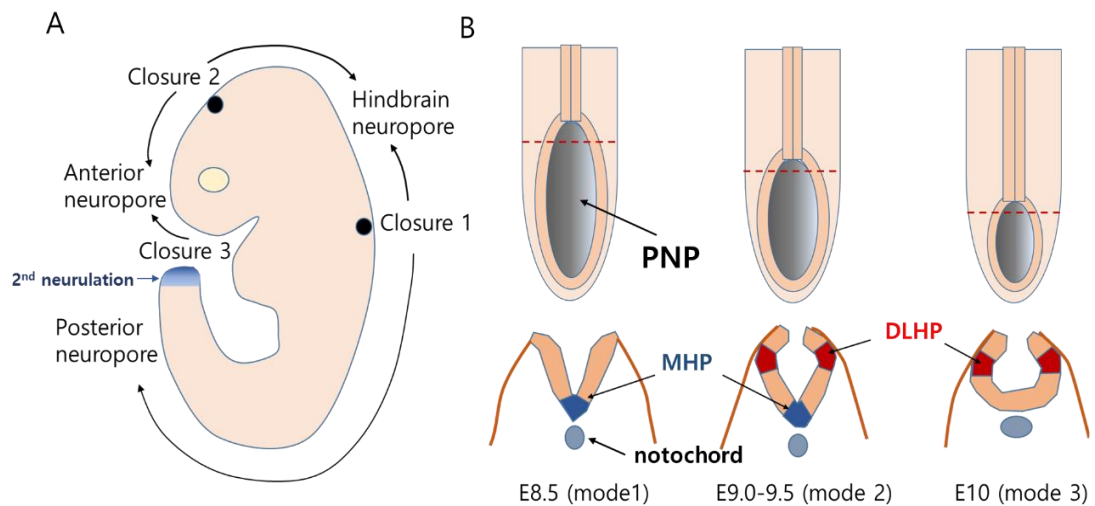


Figure 1.1. Propagation of closure during neurulation and transverse sections of the PNP at different stages.

(A) Schematic of closure progression. Closures 1, 2 and 3 occur sequentially in mice, at E8.5-E9.0. Failure of closure 1 leads to craniorachischisis. Failure of closure 2, or incomplete closure of the anterior/hindbrain neuropores, result in anencephaly. Failure of closure 3 leads to open forebrain and often split face. The PNP appears after closure 1 has occurred, and fusion is propagating caudally along the spinal region. Failure of PNP closure leads to open spina bifida. Failure of secondary neurulation (blue region at the caudal tip) causes closed, skin-covered defects in which the vertebrae are often split dorsally, and the spinal cord is tethered to other tissues within the vertebral canal.

(B) Morphologies of the elevated NFs at three different stages of spinal neurulation. Transverse sections of the PNP at the red dashed line (NP-elevated level) show that the median hinge point (MHP) is present in the early PNP, at E8.5, whereas dorsolateral hinge points (DLHPs) appear only during later spinal neurulation, from E9.0 onwards. Only DLHPs are present at the end of spinal neurulation, at E10. Figures modified from (Copp et al. 2003)

related genes over spina bifida-related genes in mice, relatively equal prevalence of cranial and caudal NTDs is observed in humans (Botto et al. 1999; Li et al. 2006; Bower et al. 2009). A possible cause for this could be, according to the explanation by Harris and Juriloff (2010), that the mouse brain is proportionately larger than the human brain during neurulation stages (Copp 2005), suggesting perhaps the need for a larger number of genes in formation of the mouse brain. In this context, it is interesting to note that the human brain does not appear to have a closure 2 event (O'Rahilly and Muller 2002), unlike the mouse, consistent with a 'simpler' process of human brain formation.

1.5. Molecular regulation of neurulation

1.5.1. Planar polarity pathway

One signalling pathway that appears particularly important for neurulation is the planar cell polarity (PCP) pathway. The mouse mutant *loop-tail* has long been known to cause craniorachischisis (Stein and Rudin 1953) and more recently it was discovered to have a mutation in the planar polarity-regulating gene, *Vangl2* (Copp et al. 1994; Kibar et al. 2001; Murdoch et al. 2001a; Montcouquiol et al. 2003). Additionally, mutations of several other PCP genes have been found in mice developing craniorachischisis: *Celsr1* in *Crash* mice, *Scrib* in *circletail* mice, *dishevelled-1/2* (digenic), *frizzled-3/6* (digenic), and *protein tyrosine kinase 7 (Ptk7)* (Curtin et al. 2003; Murdoch et al. 2003; Lu et al. 2004; Wang et al. 2006a; Wang et al. 2006b). Compound heterozygotes of *Vangl2* with other genes (e.g. *Vangl2*^{+/-}; *Celsr1*^{+/-} and *Vangl2*^{+/-}; *Scrb1*^{+/-}) were also reported to cause failure in closure 1 (Murdoch et al. 2001b; Murdoch et al. 2014). A number of reports of human NTD cases with mutations in PCP genes have also appeared in the last few years (Juriloff and Harris 2012).

At the onset of neurulation, planar cell polarity (PCP) signalling pathway plays a crucial role in convergent extension, in which cells undergo medially directed migration and intercalation with others in the midline, leading to elongation and narrowing of the body axis (Keller et al. 2008). Convergent extension seems to be essential for the NFs being aligned closely enough for the initiation of closure 1; mutation of the core PCP gene, *Vangl2*, creates shortened and widened embryos, followed by failure of closure initiation (Ybot-Gonzalez et al. 2007b). Similar results were observed with mutation of other PCP-related genes: *Celsr1*, *Scrib*, *Dvl1/2*, *Fzd3/6*, and *Ptk7*.

The PCP pathway comprises a signalling cascade through transmembrane frizzled receptors and the cytoplasmic protein dishevelled, independently of β -catenin, and hence it is often termed non-canonical Wnt signalling. The PCP pathway regulates the polarity of cells in the plane of a tissue, not in the apical-basal axis. PCP functions have been characterized particularly in *Drosophila* wings and eyes (Gubb and Garcia-Bellido 1982; Vinson and Adler 1987; Zheng et al. 1995). When PCP genes are disrupted, hairs on the wing grow from the centre of cells and exhibit swirling patterns, in contrast to the wild-type, where cells grow out in one direction, from the distal vertex (Wong and Adler 1993). Similarly, in the eyes of PCP mutants, chirality and rotation degree of ommatidia (photoreceptors) are disrupted during development (Zheng et al. 1995). In addition, mitotic spindle alignment in *Drosophila* (Bellaiche et al. 2001), polarity of inner ear hair cells in mice (Curtin et al. 2003), macro-hair patterning in mice (Guo et al. 2004), and ciliogenesis in *Xenopus* (Park et al. 2006) are also related to PCP pathway. Therefore, PCP signalling plays an important role in the morphogenesis of various organs across species.

1.5.2. Signalling pathways that regulate NP bending

Molecular signals that regulate MHP and DLHP formation are well established. MHP formation is induced by signals from the notochord (Smith and Schoenwolf 1989; Ybot-Gonzalez et al. 2002). These notochordal signals include sonic hedgehog (Shh) (Marti et al. 1995; Roelink et al. 1995) as well as BMP antagonists including Chordin (Patten and Placzek 2002). Shh shows a declining expression pattern along the spinal region, with the gradual appearance of DLHPs as neurulation progresses down the spinal axis (Ybot-Gonzalez et al. 2002). It was confirmed that Shh is necessary and sufficient for inhibiting DLHP formation, and further study revealed that the DLHPs are antagonistically controlled by Bone morphogenetic protein 2 (Bmp2), secreted from the surface ectoderm (SE) (Ybot-Gonzalez et al. 2007a). The signalling mechanisms differ between the upper spine and lower spine: as neurulation is occurring in the upper spine, expression of the BMP antagonist Noggin is inhibited by abundant Shh, resulting in strong Bmp2 signal, which leads to the inhibition of DLHP formation. When the PNP reaches the lower spinal level, the Noggin signal is strongly expressed in the absence of Shh, Bmp2 signalling is inhibited, and DLHP formation occurs.

Interestingly, DLHP formation is inhibited by complete removal of the SE (Ybot-Gonzalez et al. 2002), even though this causes loss of the inhibitory Bmp2 signal, which is derived from the SE. In the same study, when only a small fragment of the SE was left attached, while most of the SE was removed, DLHPs were still able to form. It appears, therefore, that the SE is required for DLHP formation, irrespective of BMP signalling. Moreover, while MHP is unable to form after removal of the notochord (Smith and Schoenwolf 1989; Ybot-Gonzalez et al. 2002), DLHPs form in the absence of both Shh and BMP inhibitory signals (Ybot-Gonzalez et al. 2007a), suggesting that the DLHP formation is a 'default' behaviour of the NP, even in the absence of key biomolecular signalling pathways.

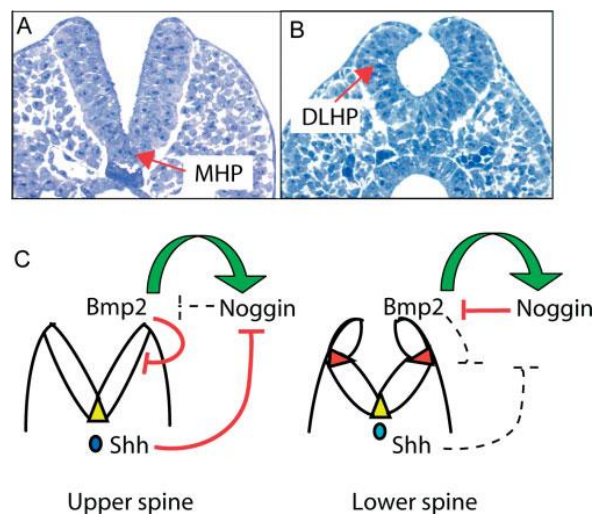


Figure 1.2. Signalling interactions between Shh, Noggin and Bmp2, and their relations to DLHP formation.

DLHP formation is opposed by Bmp2, whose antagonist Noggin is in turn negatively controlled by Shh at upper spinal levels. When Shh weakens in the lower spine, Noggin synthesis is de-repressed, Bmp2 action is blocked and DLHP formation can go ahead. In this way, the signal interaction mechanisms differ between the upper and lower spine. Figures adapted from (Copp and Greene 2010).

1.6. Apical constriction in diverse organisms

Apical constriction is a morphogenetic event, prevalently seen during the bending of a cell sheet in a variety of organisms. Actomyosin contraction has been long known to be the main mechanisms for apical constriction, and its study has been well established in *Drosophila* gastrulation.

Gastrulation of fruit flies initiates with the internalization of the tissue at the ventral furrow, the future mesoderm which forms a tube later on (Leptin and Grunewald 1990). During the internalization, cells on the apical side of the furrow narrow its surfaces, elongate their apico-basal lengths, and expand their basal surfaces (Leptin and Grunewald 1990; Sweeton et al. 1991). While maintaining the apically constricted shape, the cells return to the original apico-basal length (Sweeton et al. 1991), pushing the ventral furrow cells laterally. Concomitantly, cells become clearly wedge-shaped, which might facilitate further furrowing and positioning of the ventral furrow beneath the epidermis (Costa et al. 1993). The lateral epidermis covering the mesodermal tube is then detached from the overlying ectoderm to finish the process.

Biomolecular signals involved in *Drosophila* gastrulation has been also thoroughly studied. Cell fate for mesoderm is determined by the maternal transcription factor Dorsal, which leads to activation of the zygotic transcription factor Twist. Then, Twist target protein Folded Gastrulation (Fog), which is both necessary and sufficient for apical localization of myosin (Dawes-Hoang et al. 2005), induces apical localization of RhoGEF2, via G α protein Concertina (Cta) signaling (Barrett et al. 1997; Rogers et al. 2004). RhoGEF2 can be also apically localized by direct binding of another Twist target protein T48 (the transmembrane protein) to the Rho GTPases regulator (Kolsch et al. 2007). Then, RhoGEF2 affects Rho1 activation, followed by Rho kinase activation (Barrett et al. 1997). Finally, MLCK induces myosin activation by phosphorylating myosin II regulatory light chain, which leads to apical constriction. It was also found that RhoGEF2 directly governs accumulation and localization of myosin (Nikolaidou and Barrett 2004). Aside from myosin activity/localization, correct F-actin localization is also required for apical constriction. Abelson (Abl), a non-receptor tyrosine kinase (Fox and Peifer 2007), and the formin protein Diaphanous (Dia) (Homem and Peifer 2008) are implicated in apical constriction.

Apical constriction is also occurring in amnioserosal cells during *Drosophila* dorsal closure, while the cells are changing its shape from squamous type to columnar type

(Rugendorff et al. 1994). Apical constriction of amnioserosal cells is playing a major role in sealing the hole, in parallel with contraction of supracellular actin cable in the leading edge of the advancing epidermis (Kiehart et al. 2000). These two mechanisms work redundantly, but dorsal closure is impaired when those two type of cells are both severed by laser ablation (Kiehart et al. 2000). Actin/myosin regulators — Rac GTPase, Rho1, and Dia — are known to be associated with apical constriction of the amnioserosal cells (Harden 2002; Homem and Peifer 2008).

During the primary invagination of sea urchin, apical constriction of cells is observed in the vegetal plate. Computer modelling demonstrated that the apical constriction of cells (cell shape change) was sufficient to drive the bending of the plate (Davidson et al. 1995). Moreover, apically enriched actin microfilaments, which are connected through apical adherence junctions, were commonly thought to play main contractile roles (Ettensohn 1984). However, treatment of Cytochalasin (F-actin depolymeriser) did not affect the invagination (Lane et al. 1993), which suggests that other mechanisms of invagination are involved. Lane et al. (1993) proposed, as an alternative mechanism for primary invagination of sea urchin, swelling (hydration) of extracellular matrix in the vegetal plate could drive bending of the tissue, which also involves cell shape change.

During *C.elegans* gastrulation, endodermal progenitor cells adopt apical constriction before internalisation. At around the same time, myosin II becomes apically accumulated (Nance and Priess 2002) and activated by phosphorylation of myosin regulatory light chain (Somlyo and Somlyo 2003; Lee et al. 2006). For successful internalization of the progenitor cells, apical actin localization is also necessary; disruption of Arp2/3 actin-nucleating complex leads to failure in internalization (Severson et al. 2002; Roh-Johnson and Goldstein 2009).

Finally, apical constriction is also a crucial event during vertebrate neurulation. For both chick (Schoenwolf and Franks 1984) and mouse (Smith et al. 1994), particularly in the MHP of the neural plate, apically constricted cells (i.e. wedge-shaped cells) were predominantly observed, compared with the lateral non-bending regions, where majority of the cells adopt spindle-shape. In the next chapter, wedge-shaping mechanisms of a cell will be discussed in detail.

1.7. MHP and cell wedging

'Wedging' is a cellular morphological change which involves narrowing of the cell apex and expansion of the cell base. It can occur by apical constriction, for example through contraction of apically located actin microfilaments, or through localization of nuclei basally in cells that undergo Interkinetic Nuclear Migration¹ (IKNM). It is widely accepted that cell wedging acts as a biomechanical driver for MHP formation. Cells in the midline of the NP go through an extensive S-phase (Smith and Schoenwolf 1987, 1988), induced by notochordal signals (Smith and Schoenwolf 1989; Ybot-Gonzalez et al. 2002) resulting in the majority of nuclei in the midline becoming basally localised, leading to the adoption of a wedged cell shape (Figure 1.3 A,B). Such striking wedge-shaping in the MHP is however not observed in the lateral non-bending regions. For example, in chick embryos, 70% of the cells in the MHP and 55% of the cells in the DLHP regions are wedge-shaped, while only less than 35% of the cells in the lateral non-bending region are wedge-shaped by the end of NP bending (Schoenwolf and Franks 1984). In E8.0 mouse embryos, when bending of the NP starts to occur, the mean percentage of wedge-shaped cells in MHP (65%) is twice as large as that in lateral regions (32%) in the future forebrain, hindbrain, and spinal cord levels (Smith et al. 1994).

The finding that the midline cells become mostly wedge-shaped compared with other regions, also coincided with a recent nuclear position analysis conducted in our lab (McShane et al. unpublished). In this study, after NF elevation, the proportion of the basally-located nuclei in the midline was found to be significantly greater than in either the lateral or dorsolateral regions for E8.5 embryos, and greater than in the lateral region for E9.5 embryos. This result implies that the majority of midline cells enter an extensive S-phase during NP elevation, which leads to wedge-shaping of the cells. The extensive S-phase of MHP cells is associated with a long cell cycle, whereas the DLHP region shows a very short cell cycle, suggesting that different mechanisms are involved in DLHP bending.

Even though it was found that wedge-shaping of the midline NP cells plays an important role in MHP formation, the causal relationship between wedge-shaping and

¹ . Interkinetic Nuclear Migration: In the neuroepithelium, nuclei oscillate up and down depending on cell cycle phase. For example, during S-phase nuclei are basally located, whereas they reach the apical surface during mitosis (M-phase).

actual bending of the midline tissue remains elusive. In isolated midline strips of the chick neuroepithelium, cells were able to go through wedge-shaping without the adjacent bending tissue, suggesting that wedge-shaping of cells is not the consequence of tissue bending, but an active event prior to bending (Schoenwolf 1988). Likewise, tissue bending could still occur without cell wedge-shaping. When a notochord was removed throughout the caudal axis of a chick embryo, 8 out of the 13 embryos showed successful neural tube closure even without MHP formation and wedge-shaping in this region, suggesting that cell-wedging is not required for midline bending of the NP (Smith and Schoenwolf 1989). In mice, closure in the absence of a notochord has been shown to occur by 'ectopic' DLHPs, which are formed earlier in development than normal as a result of the lack of Shh inhibitory influence from the notochord (Ybot-Gonzalez et al. 2002). Therefore, there is strong evidence from both chick and mouse that cell-wedging plays a primary role in determining the furrow-lining characteristic of the MHP.

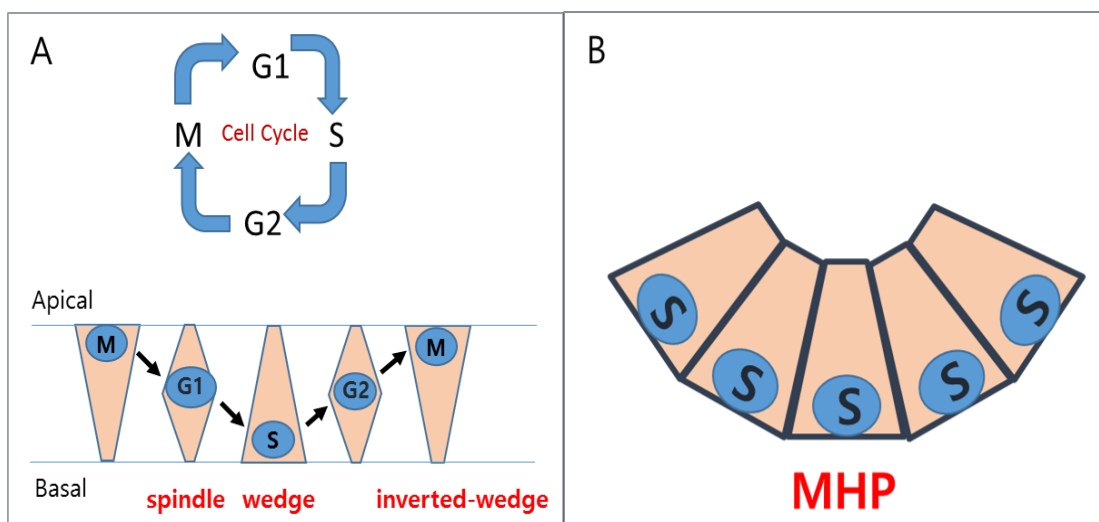


Figure 1.3 Interkinetic Nuclear Migration (IKNM) and wedging of cells in MHP.

(A) Cell cycle dependent nuclear movement in the neuroepithelium. During S-phase a cell becomes wedge-shaped with its nucleus located in the basal region. During mitosis, it forms an inverted wedge-shape, as the nucleus takes up an apical location during division. During G1 or G2 phase, a cell becomes spindle-shaped with its nucleus located in the middle region.

(B) Wedge-shaping of the cells in the MHP. In the midline region of the NP, the majority of cells become wedge-shaped due to prolonged S-phase, followed by MHP formation.

1.8. Cytoskeletal factors in cell wedging and NP bending

Wedging and apical constriction are both driven by cytoskeletal regulators: the distribution of actin (Hildebrand and Soriano 1999; Haigo et al. 2003; Hildebrand 2005) and myosin (Hildebrand 2005; Rolo et al. 2009), myosin II activity and Rho-associated protein kinase (ROCK) (Hildebrand 2005) are key factors in apical constriction, while cell cycle dependent IKNM (Smith and Schoenwolf 1988; Smith et al. 1994), and microtubule function (Kee et al. 2008; Suzuki et al. 2010) determine nuclear position and, hence, cell wedging.

Moreover, the three main factors: actomyosin contractility, IKNM, and microtubules, are functionally connected to each other. Shortening of microtubules activates RhoA, followed by activation of Rho Kinase that promotes myosin II contraction by increasing its phosphorylation (Ridley 2001). Microtubule shortening also activates the formin, mDia, which induces nucleation of unbranched F-actin (Pruyne et al. 2002; Sagot et al. 2002). Also, cell cycle dependent IKNM is closely associated with microtubule organisation, the microtubule-associated proteins Tpx2 and kinesin, and actomyosin (Del Bene 2011; Kosodo et al. 2011). It was found that inhibition of microtubule function results in IKNM failure in mouse (Umeshima et al. 2007) and in chick (Messier and Auclair 1973). Overall, the interdependent relationship between the cytoskeletal factors suggests that more than one may be at play during wedge-shaping of the cells in the NP.

In the cranial region, disrupted F-actin (Hildebrand and Soriano 1999; Haigo et al. 2003; Hildebrand 2005) and microtubules (Kee et al. 2008; Suzuki et al. 2010) cause imperfect bending of the NP with loss of wedge-shaped cells, followed by a neural tube defect. Moreover, it was found that Cytochalasin D (CD: F-actin polymerisation inhibitor) treatment induces a delay in chick NF elevation, particularly in the cranial region (Schoenwolf et al. 1988). In the presence of CD, 66% of embryos lacked DLHPs, with a predominance of spindle-shaped cells in the dorsolateral region. On the other hand, wedge-shaping in the midline still occurred, and hence the MHP was still able to form. Unlike cranial neural tube closure, however, spinal neural tube closure does not seem to be dependent on F-actin contractility. Ybot-Gonzalez and Copp (1999) found that, in the mouse spinal region, both MHP and DLHP formation can occur in the presence of CD, while cranial neural tube closure was severely affected and was not completed.

While the wedging of cells plays a major role in MHP formation, it may not always be required for DLHP formation. When Mexican salamander embryos were treated with

the microtubule-depolymeriser, colchicine, wedge-shaped cells disappeared from hinge points adjacent to the NFs (equivalent to DLHPs in mice) (Figure 1.4) (Brun and Garson 1983). A similar result was also observed in *Xenopus* morphants for Neogenin (an axon guidance receptor)(Figure 1.5) in which microtubule organisation was disrupted (Kee et al. 2008). However, in both cases, hinge points were still surprisingly able to form and fuse in the posterior region despite perturbed NF elevation. These results suggest that microtubules can affect cell wedging and, more importantly, that hinge points are able to form irrespective of this cell shape change in amphibians.

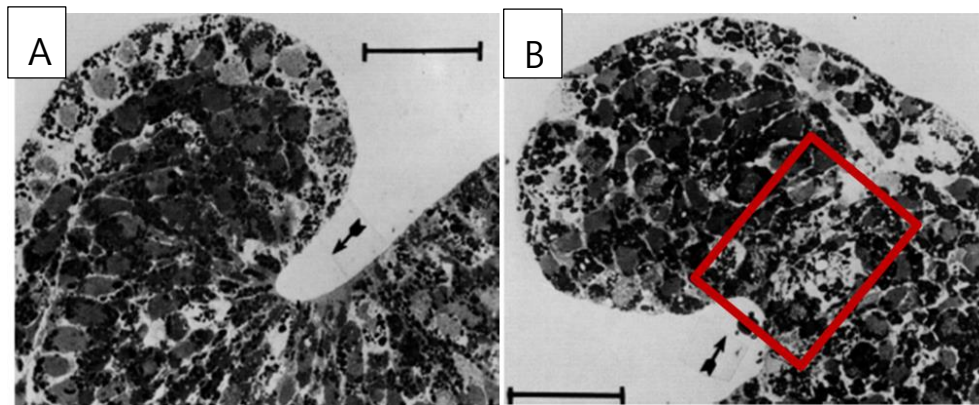


Figure 1.4 Effect of colchicine on wedge-shape cells in the Mexican salamander.

(A) Control embryo at stage 18. Constricted zone (wedge-shape, arrow) is apparent.

(B) Stage 18 embryo after colchicine treatment at stage 13-14. The constricted zone disappeared from the dorsolateral region, but hinge points were still formed (red box).

Both figures are from the anterior region (figure for the posterior region not available).

Figures adapted from (Brun and Garson 1983)

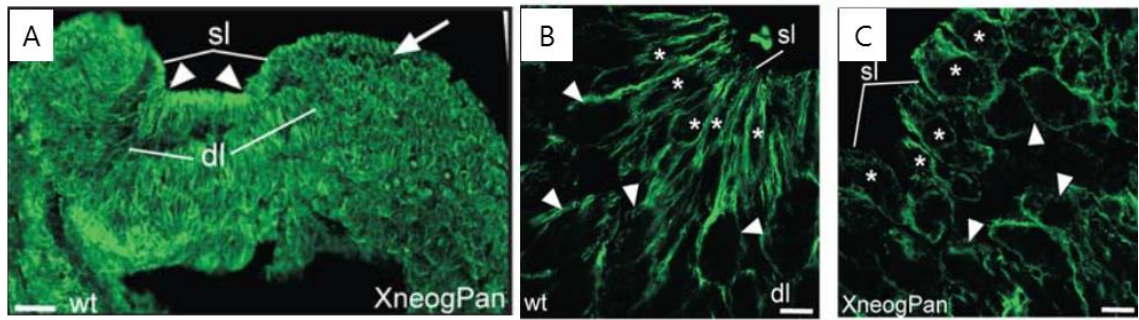


Figure 1.5. NP cells in *Xenopus* morphants lose wedge-shape but hinge points are maintained.

(A) The anterior NP of a *Xenopus* embryo. Morpholino for *Neogenin* (*Xneog*) was unilaterally injected on the right side, while the wild-type (left) side was untreated. Hinge points formed correctly (arrow heads) on the both sides, despite the perturbed elevation of the NF on the morphant side (arrow).

(B-C) Magnification of the hinge points on the wild-type (B) and morphant (C) sides. While cells are wedge-shaped in the superficial layer (sl) of the wild-type hinge point, they are more rounded in the sl of the morphant hinge point, along with the loss of Intercalation with deep layer cells (arrow heads). Figures adapted from (Kee et al. 2008).

1.9. Possible mechanical mechanisms of dorsolateral NP bending

A large number of studies of amphibian and avian embryos have investigated mechanical roles of the SE in dorsolateral NP bending. Jacobson et al. (1986) described a 'cortical tractor' model of amphibian neurulation in which NP cells moved medially by 'tractoring' on the SE. In the Mexican salamander, it was postulated that the extending SE curls the neuroepithelium inward, thus leading to hinge point formation (Brun and Garson 1983). Alvarez and Schoenwolf (1992) suggested that the SE of chick embryos plays a similar role in dorsolateral hinge formation by its medial-ward expansion. The possible causes of the SE movement could be cell shape changes - increasing width with decreasing height - in prospective SE cells in chick (Schoenwolf and Alvarez 1991), caudomedial convergent-extension movements in chick (Schoenwolf and Sheard 1990), and non-randomly oriented cell division in the neuroepithelium and SE for both chick and mouse (Sausedo et al. 1997). However, in a mouse study, where most of the SE was removed while only a small fragment of the SE was left, DLHPs were still able to form (Ybot-Gonzalez et al. 2002), suggesting that the extrinsic force of the SE is unlikely to be the factor in DLHP formation.

It seems that the paraxial mesoderm is also dispensable as a mechanical factor in DLHP formation. When the paraxial mesoderm was surgically removed, leaving the dorsal-most SE intact in mouse embryos, DLHPs still formed and neural tube closure progressed normally (Ybot-Gonzalez et al. 2002). A similar result was also confirmed in chick embryos (Alvarez and Schoenwolf 1992).

In a recent study from our lab, the SE was completely removed and the proliferation rate of neuroepithelium was monitored (Figure 1.6 B,C) (McShane et al. unpublished). On the side where the SE was removed, cell proliferation significantly decreased (Figure 1.6 C). In conjunction with a previous study that, upon complete removal of the SE, the existing DLHP vanished and new DLHP formation was also prevented (Ybot-Gonzalez et al. 2002), this result implies that cell proliferation in the NP may be required for DLHP formation. The same study also showed that there is a difference in proliferation rate between the dorsal and ventral halves of the NP, with the former being more proliferative (Figure 1.6 B, arrow), and this difference may play a mechanical role in dorsolateral bending. In support of this type of mechanism, a higher rate of proliferation was observed in the part of the avian gut endoderm that undergoes highly hinged folding (Miller et al. 1999). Just like the gut endoderm, regional proliferation rate differences in the neuroepithelium may cause a pressure imbalance within the tissue, which contributes to tissue bending.



Figure 1.6 Spatial distribution of cell cycle-related protein expression during NP bending.

(A-C) Immunohistochemistry for Cdk4 (A), and Cyclin D1 in control (B) and in SE-depleted (C) embryos. The signal is most intense in the dorsolateral NP adjacent to SE for both Cdk4 and Cyclin D1 (arrows in A-C). After surgical removal of the SE unilaterally from the PNP region (dashed line in C), the gradient expression of cyclin D1 is lost within half an hour. no: notochord. Figures adapted from (McShane et al. unpublished).

Extracellular matrix (ECM) has also been implicated in bending of the NP. ECM is present mainly at tissue interfaces (basement membranes) along the dorso-ventral axis during NF elevation. For example, ECM lies between the SE and the NP in the dorsal region where the NFs form, and between the paraxial mesoderm and the NP more ventrally.

ECM expansion in the mesenchyme underlying the NP is thought to contribute to NP bending and NF elevation during cranial neurulation (Morris-Wiman and Brinkley 1990). At the onset of NF elevation in the cranial region in mice, mesenchymal cells underlying the NP become highly polarized, with an increase in mesenchymal cell density. At this time, hyaluronan (HA), a matrix carbohydrate polymer which exists abundantly in the ECM between mesenchymal cells, also increases its concentration. Then, expansion of the HA-rich ECM in the central mesenchyme, presumably due to its hydration (Solursh and Morriss 1977; Morriss and Solursh 1978), causes an enlargement of the volume under the NP, which finally gives rise to elevation and medial-ward movement of the NFs. However, inhibitor studies in this experiment turned out to be flawed, as the inhibitor (diaz-oxo-norleucin) also affected other surrounding tissues, and so its effect in inhibiting cranial NF elevation may not have been specific (Zohn and Sarkar 2012). Meanwhile, exencephaly is observed in mouse embryos with mutations in the helix-loop-helix transcription factor, *Twist*, or in the homeobox transcription factor *Cart1*, both of which are expressed in the cranial mesenchyme during morphogenesis (Chen and Behringer 1995; Zhao et al. 1996). In both cases, mesenchymal expansion is defective prior to exencephaly, suggesting that cranial mesenchyme expansion is indeed essential for cranial NF elevation.

Similar ECM-driven epithelial bending has been observed in sea urchin primary invagination (Lane et al. 1993). In this model, calcium-regulated secretion of ECM components from vegetal plate cells form a bilaminar matrix apically, comprising an inner hyaline layer (recently-deposited) and an outer hyaline layer (previously-deposited). When the newly formed layer undergoes swelling by hydration, it starts to bend, which results in bending of the whole epithelium. This bending model is analogous to the bending of a bimetallic strip in a thermostat, in which two different metal layers go through different thermal expansion given the same heat amount.

1.10. Experimental approaches to understanding the mechanics of morphogenesis

Mechanical properties of embryonic tissues have been studied with various experimental approaches. Atomic Force Microscopy (AFM) is an increasingly commonly used instrument for measuring Young's modulus (i.e. elastic modulus or stiffness) of samples across many fields of science. AFM enables measurement of tissue stiffness by detecting a change in a laser path that is caused by deflection of highly sensitive cantilever upon its contact with the sample. Similar but modified versions of AFM are also often used, depending on the properties of tissue or the characteristics of experiments. For example, in one study, an AFM cantilever, which normally has a sharp tip (probe), was attached with a glass-bead to measure/compare the elastic properties of neural retina and retinal pigment epithelium during the optic cup (retinal primordium) morphogenesis (Eiraku et al. 2011). The round contact structure of the bead enables the gradual application of a force, and hence soft tissue could be indented in more delicately controlled manner.

In a study by Zhou et al. (2009), a custom-designed instrument (nanoNewton force measurement device) was used to measure the mechanical properties of three different germ layers in the dorsal tissue of frog embryos, at different stages. The working principle of the instrument follows the basic principle of AFM: laser-based detection of the deflection level of a probe. Upon the sample's contact with an optical fiber probe, the compression level of tissue can be optically detected and recorded over time, from which the resistive tissue force can be calculated. Then, Young's modulus could be calculated from the temporal profiles of resistive force and the compressive strain of the tissue.

Slightly differently, Wiebe and Brodland (2005) used a tissue-stretching device to test the tensile properties of amphibian embryo epithelia. Two cantilevers were glued onto the explant in parallel, and one of the cantilevers was pulled apart from the other by a computer-controlled motor. By measuring the lateral displacement of the moving cantilever, the tensile force of the tissue was calculated. Then, the area of the tissue that went through uniform strain was identified by digital image tracking, with use of a superimposed electronic grid to enable changes in the images to be tracked during stretching. Elastic modulus was calculated from the tensile force and strain values.

The aspiration of tissue into an apposed pipette has also been used to measure tissue deformation ability (i.e. stiffness). In *Xenopus* embryos, when a bulge of NP tissue

reached a fixed size in the aspirating pipette, the magnitude of the negative pressure applied was recorded and compared for control and myosin-II β morpholino-treated embryos (Rolo et al. 2009). It was found that a reduced degree of negative pressure was needed for myosin II β -depleted embryos, suggesting that myosin-II β regulates deformability of tissue.

The incision and excision of tissues is another, indirect approach to understanding the mechano-biological roles of embryonic tissues. This approach has been extensively used in chick embryos to answer questions about the mechanical role of each tissue layer in neurulation. In one study, even though the midline region in the cranial part was excised, NF elevation, convergence, and fusion were still able to occur, suggesting that midline bending is not crucial for neural tube closure (Smith and Schoenwolf 1991). Similarly, In the brain region of chick embryos, when mesoderm and endoderm were removed, leaving only the SE intact, NP bending and fusion still occurred (Alvarez and Schoenwolf 1992). Direct evidence that the SE is required for neurulation was provided in a study by Hackett et al. (1997), in which NF elevation was observed to be inhibited when the epidermal ectoderm (surface ectoderm) adjacent to the NP was removed, leaving other lateral tissues intact.

Finite Element Method (FEM) is a computational simulation method to investigate the dynamics of an object. FEM has been increasingly used in a variety of biological research fields to predict the motion, or to calculate the mechanical parameters, of cells and tissues. For example, during heart tube formation in chick embryos, FEM was used to determine whether the endoderm or mesoderm layer is more contractile in the bilayered structure of the anterior intestinal portal. Each layer in the modelling was given a different stiffness value, and the computed motion of the layers after a simulated cut was compared with the actual mechanical response of the tissue to incision (Varner and Taber 2012). FEM has also been widely used in neurulation modelling. While the simulations of the late 20th century were mostly limited to 2D or pseudo-3D, Chen and Brodland (2008) first used 3D simulation of neurulation in the whole amphibian embryo. In their 2008 study, based on real 3D geometrical data and mechanical properties of the embryonic tissue, the effects of Shroom-dependent ridge formation and lamellipodium force profiles across the NP width were studied, by changing the related mechanical parameters.

1.11. *Zic2* gene and its role in neurulation

The *Zic* genes are the vertebrate orthologues of the *Drosophila* pair rule gene *odd-paired*, which regulates the activation of the segment polarity genes, *engrailed* and *wingless*, in a timely manner (Aruga et al. 1996). The *Zic* genes consist of a group of genes encoding zinc finger proteins that are expressed in the cerebellar granule cells in the adult mouse (*Zic*, zinc finger protein of the cerebellum) (Aruga et al. 1994). In mice, there are five *Zic* genes (*Zic1-5*) that are highly homologous to each other in the entire zinc finger domain (Aruga et al. 1996). The five genes have partially overlapping, but spatially distinct patterns in the dorsal neural tube, dorsal paraxial mesenchyme and limb bud (Nagai et al. 1997; Gaston-Massuet et al. 2005). The *Zic* genes are usually divided into two groups, according to their related functions: *Zic1* and *Zic4* are both required for cerebellar development and, due to their adjacent genomic location on human chromosome 3q, have been implicated in a contiguous gene deletion syndrome that causes the hindbrain defect, Dandy Walker syndrome (Grinberg et al. 2004). Members of the other group: *Zic2*, *Zic3* and *Zic5*, are strongly implicated in early nervous system development, including neurulation, as NTDs form part of the mutant phenotype for all three genes (Houtmeyers et al. 2013).

During neurulation, *Zic2* is strongly expressed throughout the neuroepithelium of the PNP, but on completion of closure, transcripts become restricted to the roof plate and the region laterally adjacent to the NP (Gaston-Massuet 2004; Gaston-Massuet et al. 2005). *Zic2*-knockdown mice exhibit holoprosencephaly, spina bifida, and some skeletal abnormalities with the delay in the neurulation process, which suggests that *Zic2* is required for the progression of neurulation (Nagai et al. 2000). It was further found from a loss-of-function allele, that *Zic2* also regulates neural crest production and hindbrain patterning along with both cranial and spinal neurulation (Elms et al. 2003).

Kumba (*Ku*) is a loss-of-function allele of *Zic2* isolated from an ENU (N-ethyl-N-nitrosourea) mouse mutagenesis experiment (Nolan et al. 2000). The ENU-induced point mutation is in the 4th zinc finger, abolishing the function of the entire zinc finger domain (Elms et al. 2003). On our background (mixed C3H and C57BL/6), *Zic2^{Ku/Ku}* mice show spinal neurulation defects with a 100% frequency. Cranial defects are present in most embryos but can be either holoprosencephaly or exencephaly. *Zic2^{Ku}* heterozygotes generally develop normally, although a low frequency of spina bifida has been reported (Elms et al. 2003).

1.12. Overview of the thesis

This thesis aims to elucidate extrinsic (tissue-level) and intrinsic (cellular-level) forces that drive DLHP formation during neural tube closure, and to understand the underlying biomechanical mechanisms of spina bifida in *Kumba* mutant mice.

Chapter 3 focuses on the gross and tissue-level morphological changes that follow incision of the most recently closed neural tube roof in wild-type embryos. From these experiments, I was able to conclude that NP bending during PNP closure is partially elastic, and I inferred the origin of the 'external' force that causes NP bending. Cell shape and nuclear morphology in the NP were investigated at different caudo-rostral levels of the PNP, in order to determine the relationship between the cellular changes and DLHP formation. Lastly, the effect of incision on the cellular morphology was studied.

Chapter 4 examines the possible mechanical factors involved in spinal neurulation failure in *Kumba* mice. Morphological differences between the mutant and wild-type were compared at the level of PNP closure, and at the stage of onset of the spinal neurulation defects. Then, by incising the recently closed neural tube roof of mutant and wild-type embryos, using the same method as in Chapter 3, the NF re-opening distance was compared. This experiment revealed a striking increase in the degree of tension (i.e. opposition to the closing force) at the PNP closing point in *Kumba* mutants compared with wild-type. Cellular morphology differences were also compared between the different genotypes.

In Chapter 5, I used AFM, to measure NP stiffness and compare the findings between *Kumba* mutant and wild-type embryos. This test provides evidence that the tension difference observed in Chapter 4 at the closing point of the PNP in mutant embryos originates from elevated stiffness in the NP.

Finally, in Chapter 6, I performed FEM-based simulation to calculate the force required to effect NF closure in the PNP region. I compared the required closure forces for *Kumba* mutant and wild-type embryos, after inputting physical parameters that were measured experimentally in Chapters 4 and 5. This FEM analysis confirms that the *Kumba* mutant requires a greater amount of force to achieve closure than wild-type embryos, probably accounting for the development of spinal NTDs in this genotype.

2. Material and methods

2.1. Mouse embryology

All mice were maintained in the Biological Services Unit at the UCL Institute of Child Health, complying with the regulations set by the Home Office and covered by Project Licence PPL 70/7469. Mice were mated twice per day. Morning matings were set up at 09:00, and plugs were checked at 17:00. In this case, 12:00 was designated embryonic day E0. Evening matings were set up at 17:00, and plugs were checked at 09:00 following day. In this case, 24:00 was designated embryonic day E0. All mice used in this thesis were fed/watered *ad libitum*, and were on a 24-hour light/dark cycle (light from 08:00 to 20:00).

2.1.1. *Kumba* mice

The *Kumba* mouse mutant carries a *Zic2* loss-of-function allele. Our *Kumba* mouse colony was initially kept on a congenic C57BL/6 background, but due to the severity of the *Zic2*^{Ku/Ku} phenotype, *Zic2*^{+/Ku} mice were outcrossed to a congenic C3H/HeH background for a couple of generations (Raza-Knight et al. unpublished PhD thesis). The frequencies of *Kumba* genotypes obtained on this mixed C3H/C57BL/6 background were not recorded during my experiment, but recognized as being roughly corresponding to Mendelian ratios (i.e. +/+ : 25%, +/Ku : 50%, Ku/Ku : 25%). On this background, the phenotype of the heterozygous embryos seemed identical to that of the wild-type littermates that were developing normally. At E9.5, the latest stage of embryos collected for my study, spina bifida appeared in the homozygous mutant with a 100% frequency (see Chapter 4). The cranial region of the mutant embryos also remained open in a great majority of the embryos while it was closed for the heterozygous and wild-type embryos. The detailed phenotypes of the mutant on this background were not recorded. However, according to previous work in our lab (Raza-Knight et al. unpublished PhD thesis), on the same mixed C3H/C57BL/6 background, failure of spinal neurulation in the mutant led to fully penetrant spina bifida and 41% tail flexion defects, whereas failure of cranial neurulation led to 74% exencephaly and 22% holoprosencephaly. According to the same unpublished work, litter size was 8.17 ± 0.21 , there were 0.49 ± 0.09 resorptions per litter, and non-pregnant females occurred at 16.2% frequency.

2.1.2. Balb/c

Embryos of non-mutant Balb/c background were used for investigating the effect of incision on the re-opening of the wild-type neural tube.

2.1.3. *Grhl3*^{cre/+};*ROSA*^{YFP/+}

In a study by Camerer et al. (2010), *Grhl3*^{cre/+} mice were crossed to the mice carrying YFP Cre excision reporter alleles driven from *ROSA26* locus (Srinivas et al. 2001) at E8, in order to examine Cre recombinase activity. The same study showed that the reporter expression is first observed in the midline, and it spreads laterally in the surface ectoderm, ultimately covering the whole embryo. Later in our lab, it was experimentally found that *Grhl3*^{cre/+};*ROSA*^{YFP/+} mice show a mosaic pattern of YFP expression in the NP at E9.0-E9.5.

2.1.4. Embryo collection

Once vaginal plugs were found, pregnant females were kept in separate cages in the ICH animal facility. On a scheduled date, pregnant females were culled by cervical dislocation, followed by decapitation. A V-shaped incision was made in the lower abdomen of the mouse, and the uterus was removed by cutting below the ovaries and by cutting through the cervix where the two uterine horns join. For dissection, uteri were transported to the lab in a 7 ml capacity bijou bottle filled with GIBCO® high glucose Dulbecco's Modified Eagle Medium (DMEM, catalogue number 42430, Invitrogen) containing 10% GIBCO® certified, sterile-filtered foetal bovine serum (FBS, Invitrogen). Embryos were dissected with two pairs of watchmaker's forceps (no.5) in 37°C warmed solution of DMEM + 10% FBS. FBS had been heat-inactivated at 58°C for half an hour prior to being aliquoted and stored at -20°C. Embryos were then processed according to their use.

2.1.5. Culture technique

All the dissection procedures were performed in DMEM + 10% FBS, pre-warmed to 37 °C. Implantation sites were carefully removed from uterine horns, and the decidual tissue was dissected away until the trophoblast-covered conceptus appeared. The trophoblast layer together with the underlying Reichert's membrane were removed, except that the ectoplacental cone trophoblast was left intact, as it was necessary for

preservation of an intact yolk sac around the embryo. The embryos, enclosed in yolk sac and amnion, were then transferred to rat serum in a 50 ml round-bottomed culture tube. At least 0.3 ml of rat serum was used per embryo, with serum being equilibrated for at least 20 min using a gas mixture containing: 5% CO₂, 5% O₂, 90% N₂. The tube was gassed with 5% CO₂, 5% O₂, 90% N₂ for E8.5 embryos, or 5% CO₂, 20% O₂, 75% N₂ for E9.5 embryos and sealed with vacuum grease (Glisseal). Then, the tube was placed in a rotating, light-protected 37 °C incubator overnight or for longer if necessary. The tubes were gassed every 6 -12 hours. The following day, yolk sac circulation and heart-beat rate were scored using the criteria in the Table 2.1. Embryos scored as '0' for either yolk sac circulation or heart beat were excluded from analyses.

Table 2.1 Yolk sac circulation and heart beat scoring criteria.

	++	+	±	0
Yolk sac circulation	Vibrant and constant pulsatile flow	Vibrant with a little delay in the flow	Weak with a long delay in the flow	No circulation
Heart beat	Fast, regular beating	Beating with a little delay in the interval	Slow, occasional beating	No beating

2.2. DNA and protein methods

2.2.1. *Kumba* genotyping

DNA extraction

Embryonic heads were collected for DNA extraction before the remainder of the body was fixed. Genomic DNA-releasing reagent, DNARELEASE™(Anachem), was diluted 1:5 in Milli-Q water, and 20 µl of the solution was added to the sample. Then, the tubes were placed in a thermal cycler with a heated lid on the following lysis programme: 65°C for 15 min; 96°C for 2 min; 65°C for 4 min; 96°C for 1 min; 65°C for 1 min; 96°C for 30 sec; 20°C for 10 min. After lysis, samples were either processed for PCR or stored at -20°C.

Kumba genotyping

Kumba primers were prepared as described by a former lab member (Raza-Knight et al. unpublished PhD thesis). Primers were designed from the D14Mit107 locus

(chromosome 14), owing to its extremely tight linkage to the *Zic2* gene (< 0.2 cM; Mouse Genome Informatics: www.informatics.jax.org). The primers were:

(left: 5'-AAATGGTCATCCCTGAAAAGA-3'; right: 5'-CAGGCCTCTCCAAAGTACCA-3').

Two microlitres of genomic DNA was mixed with 5 µl of 10x PCR buffer, 1.5 µl of MgCl₂ (50 mM), 5 µl of dNTP (2 mM), 0.3 µl of *Kumba* primers, 0.25 µl of Taq polymerase, and 35.95 µl of Milli-Q water to a final volume of 50 µl. PCR was performed in a thermal cycler (MJ Research PTC-200) on the following programme: 94°C for 4 min; 94°C for 2 min, 58°C for 1 min, 72°C for 1 min, 35 cycles; 72°C for 10 min. For gel electrophoresis, 3% agarose was mixed with TAE buffer (1X solution: 40mM Tris, 20mM acetic acid, and 1mM EDTA buffer(pH 8.0)), and 0.003% ethidium bromide was added before the molten gel solidified. PCR products were electrophoresed at 120 V for roughly 20 min, with DNA Hyperladder V (Bioline) as size reference. The wild-type *Kumba* allele is in coupling linkage with a D14Mit107 allele of band size 150 bp, whereas the mutant *Kumba* allele is linked to a 176 bp allele of D14Mit107. Heterozygous mice exhibit both bands.

2.2.2. Electroporation

Cytoplasmic GFP plasmid vector (PCAG_IRESGFP) was concentrated at 3000 ng/µl, and 2.5 µl of the GFP construct was mixed with 1 µl of Fast Green (2%, diluted 1:4 in PBS) for injection. The GFP-Fast Green solution was sucked up into a glass micro-needle using a mouth-controlled micro-injector (aspirator tube assemblies for calibrated microcapillary pipettes, Sigma Aldrich). Roughly half of the amniotic volume of an E8.5 embryo was filled with the GFP-Fast Green mixture, and the embryo was left for one minute, until the GFP construct became uniformly distributed within the amniotic cavity. Electrodes (Harvard Apparatus, Inc, model 508, straight Genetrode 5mm, Gold Plated catalog #45-0113) were positioned directly above an agarose mould (3% in PBS) in a PBS-filled dish, and each GFP-injected embryo was positioned between the electrodes with the ventral side of the PNP region facing the (+) electrode. This had the effect of directing DNA transfection towards the apical surface of the caudal NP.

It was easier to immobilise the embryo if the agarose mould had a small hole made with a pipette tip so that the ectoplacental cone could be gently fitted inside (Figure 2.1). This way, the ventral surface of the embryo could be seen down the

stereomicroscope, and the GFP construct could be electroporated into the caudal region with greatest accuracy.

After applying voltage (23 V, 5 pulses with 50 msec pulse length, interval 950 msec), embryos were immediately transferred to DMEM + 10% FBS, and then to equilibrated rat serum, as described in Section 2.1.5. GFP expression could usually be detected after overnight culture, although longer culture periods were used if necessary.

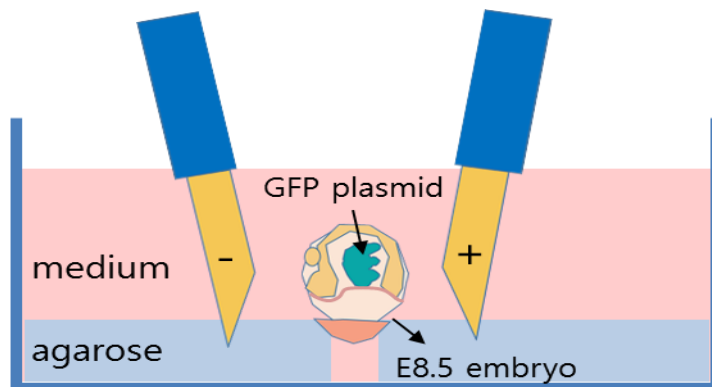


Figure 2.1 Schematic of GFP-electroporation in E8.5 embryos.

GFP plasmid vector was injected into the amniotic cavity of an E8.5 embryo, which was then positioned in an agarose hole, with the ventral side of the embryo facing upwards. Electric pulses were applied, with the (+) electrode positioned next to the caudal region of the embryo.

2.2.3. Immunohistochemistry

GFP and YFP signals on cryosections (see details in 2.4.1) were further enhanced with Alexa Fluor® 488 conjugated rabbit α -GFP antibody (Life technologies). Cryosections were incubated in PBS in a water bath (37 °C) for at least half an hour to remove gelatin. After pouring away the PBS solution, new PBS was added and gently shaken for 10 minutes. PBST (10% sheep serum in PBS with 0.1% Triton x-100) was applied to the slides for blocking, and the slides were incubated at room temperature for at least 2 hours. After removing the remaining PBST on the slides by gentle tapping, Alexa Fluor® 488 GFP-conjugated rabbit antibody (Invitrogen) was applied at 1:1500 in PBST. Parafilm was gently laid on the slides to ensure uniform application of the antibody to the sections. Then, the slides were incubated at 4 °C overnight after sealing the slide boxes with aluminum foil and putting water-soaked tissues inside for hydration. The following day,

the slides were washed three times in PBS for 5 min each, DAPI was applied at 1:10000 in PBS, if necessary, and incubation was continued for 3 min at room temperature. Slides were washed twice in PBS for 5 min, mounted with Mowiol, and left in a cold room overnight.

2.3. Incision techniques

Labelling with Dil

CellTracker™ CM-Dil (Molecular Probes) was used to label the embryonic surface ectoderm just next to the closing PNP level. Dil powder was dissolved in 25 µl of dimethylsulfoxide (DMSO), and 5 µl of it was added to 45 µl of 0.3M sucrose. A micro glass needle connected to a mouth-injector (aspirator tube assemblies for calibrated microcapillary pipettes, Sigma-Aldrich) was filled with Dil solution, and was inserted just beneath the surface ectoderm. Dil was gently expelled until focal staining of the ectoderm was visible.

Incision methods

Incision of the most recently closed neural tube roof was performed using a hand-held fine glass needle. This was inserted into the dorsal midline of the closed neural tube, followed by a caudalward slicing movement up to the closing point of the PNP to incise the neural tube roof and overlying surface ectoderm. Then, the incised embryos were left at least for a minute in medium (DMEM + FBS) in order for them to reach a static state (equilibrium state). After a brief wash in PBS, the embryos were fixed in either Bouin's solution for tissue morphology analysis or 4% paraformaldehyde (PFA) in PBS for cell shape analysis. Dorsal views of the fixed embryos were imaged in PBS to record the incision length and dorsal transverse opening. For the time-lapse live-imaging of the re-opening of the PNP, Openlab (imaging software from PerkinElmer) was used at 1 frame per second, while holding the embryos (in medium) with forceps.

2.4. Histology and imaging

2.4.1. Cryosections

Cryosections were mainly used for cell shape analysis. Embryos were fixed in 4% PFA in PBS for no more than 3 days at 4 °C. Embryos were washed in PBS and left in 15%

sucrose in PBS overnight. Then, embryos were incubated at 37 °C in 7.5% gelatin (bovine skin) with 15% sucrose in PBS for at least half an hour, and put in a fridge for half an hour for the gelatin to solidify, after orienting the tissue to achieve the appropriate sectioning plane. The gelatin sample block was placed on an OCT-applied cork disc block, with its cutting-face upwards. The sample was transferred in an isopentane-filled beaker that had been submerged in -70°C liquid nitrogen-filled container. After a couple of minutes, the sample was taken out and stored at -80 °C. A Leica cryostat was used for sectioning, with thickness maintained at 20 µm for *Grhl3^{cre/+};ROSA^{YFP/+}* embryos, and at 25 µm for *Kumba* embryos. During sectioning, temperature was maintained at around -22 °C. The section(s) containing the Dil mark, were located using a bright-field or fluorescence microscope (green filter) before doing any immunostaining or H&E staining.

2.4.2. Paraffin wax sections

Paraffin wax sections were mainly used for the morphological analysis of incised embryos. Embryos were fixed in Bouin's solution (Sigma Aldrich), and kept at room temperature. Samples were not stored in Bouin's solution for more than 7 days as Dil marks started fading. Embryos were washed in PBS for more than 3 hours on a gently rotating shaker. They were transferred sequentially through 25%, 50%, 70%, 95%, and 100% ethanol, for 20 min each. Then, they were transferred to HistoClear-filled glass moulds, left for 30 min at room temperature, and immersed in fresh HistoClear solution in a 60 °C oven for the same duration. After removing the HistoClear solution from the moulds, molten paraffin wax was applied and left in the 60 °C oven for 45 min. This process was repeated twice. After changing into new paraffin wax, the embryos were oriented at appropriate angle under a bright field stereomicroscope, and then the wax was allowed to solidify. Sectioning was performed at 12 µm section thickness, using a Microm HM 325 microtome (Leica). After floating the sections on water-covered glass slides at 37°C to ensure full expansion of the wax, the water was removed and slides were left in 37 °C oven overnight until they had completely dried. Section(s) containing the Dil mark, were located using a bright-field or fluorescence microscope (green filter) before doing any immunostaining or H&E staining.

2.4.3. Haematoxylin and eosin staining

Slides were incubated in Histoclear for 10 min twice to dissolve wax on slides, followed by an ethanol series: 100% twice, 95%, 70%, 50% and 25% ethanol, each for 2 min for rehydration of sections. Then, the slides were put in Milli-Q water for 2 min. Slides were incubated in filtered Mayer's haematoxylin for 1 min, followed by washing under tap-water for 5 min. Next, slides were incubated in filtered aqueous eosin for 3 min, and washed under tap-water for 2 min. For dehydration of tissues, slides were rinsed quickly in 70%, and 100% ethanol, and mounted with DPX. Slides were left in a fume hood overnight for DPX solidification.

2.4.4. Imaging

For cell shape analysis (cell curvature and nuclear circularity), confocal laser microscope (Zeiss LSM 710) was used to create a z-stack image with x63 oil-immersion lens. The microscope-controlling software was ZEN2009. When imaging H&E stained sections for NP bending degree analysis, a Zeiss AxioCam HRc camera connected to a Zeiss Axioplan2 microscope was used with Axiovision software. For imaging the whole embryos, a Leica DFC490 camera connected Zeiss Stemi SV11 stereomicroscope was used with CS3 Photoshop. Cell shape analysis methods are described in Chapters 3 and 4.

2.5. Atomic Force Microscopy (AFM)

2.5.1. Sample preparation

In the lid of a 35 mm petri dish, 0.5 ml of 3% agarose in PBS was spread thinly and solidified. Then, a half of the agarose was removed by making a sloped-cut in the middle of the dish with a scalpel. Cellulose tape was attached to the agarose-free area of the dish, and its edge, which was truncated in a 'v' shape using a scalpel, was gently laid against the sloping border of the agarose. The dish was then filled with 1.5 ml of DMEM + 10% FBS. If necessary, 3.5 μ l of propidium iodide (1 mg/ml, Invitrogen) was added.

During dissection of each embryo, the ventral midline of the PNP was bisected with a micro glass needle. The body axis was transected at the level, reasonably rostrally distant from the closing point, to create a pair of 'NP halves'. One of the NP pairs was then gently laid on the sloping-agarose mould with its apical surface facing upwards, and

the 'v'-shape-truncated edge of the tape was gently laid over the sample, leaving the NP surface exposed for access by the AFM probe (see details in Chapter 5).

2.5.2. Measurement

The AFM instrument was a JPK NanoWizard® and the silicon cantilever was a C triangular MLCT (Bruker), which has the lowest spring constant (nominal resonant frequency: 7 kHz; nominal spring constant: 0.01 N/m). Before measurement, cantilever calibration was performed on a clean glass slide to obtain sensitivity and spring constant values of the cantilever. Then, on one side of the slide, a small amount of UV-curing glass bond (3M) was applied and thinly spread. A small quantity of glass beads (diameter $\leq 106 \mu\text{m}$, Sigma Aldrich) were spread on the other side of the slide. Using the AFM instrument, the cantilever tip was levelled down until it gently touched the bond, and quickly retracted. The adhesive-applied cantilever tip was then levelled down until it gently pressed on an isolated single glass bead of mean diameter 60-70 μm . The moment that the cantilever tip touched the glass bead was marked by the change in the photodiode signal. Then, the glass bead-attached cantilever was further cured with UV-light for approximately 1 min. Afterwards, the sensitivity of the glass bead-attached cantilever was re-measured. During AFM measurements on the NP, the relative set point was 10 nN, and the approach and retraction delays were set at 4 sec and 3 sec, respectively. Full piezo-range (15 μm) was used. The sample was probed with an interval of 12.5 μm using a grid function in JPK SPM data processing software. All measurements were performed at room temperature.

2.5.3. Young's modulus calculation

The output of the AFM measurement, a force-distance curve, was then analysed using JPK data processing software (Figure 5.1 B). Hertzian contact mechanics (a curve-fitting method for a spherical probe) was taken into account in the calculation of Young's modulus of the sample, with respect to the 'approaching' curve. The indenting force F is then expressed as:

$$F = \frac{4}{3}ER^{1/2}d^{3/2}$$

where F is the applied force, E is Young's modulus of the sample, R is the radius of the spherical probe, and d is the indentation depth. While selecting the range of the curve for the fitting process, the indentation depth was kept at no more than $5\ \mu\text{m}$, which is within 10% of the mean NP thickness $50\ \mu\text{m}$ (data not shown); If indentation is too deep (e.g. over 20% of the sample thickness), the rigidity of the substrate could affect the measurement (Harris and Charras 2011). The quality of curve-fitting tested by calculating the residual RMS (root-mean-square) value, and only curves for which residual RMS value did not exceed $150\ \text{pN}$ were considered. For each region of the NP, data outliers were defined as values that fell within the top or bottom 5% of the number of the measured values. For example, if there were 32 measured values for the ventral side of the NP, the largest 2 and the lowest 2 values were disregarded.

2.6. Finite Element Modelling (FEM)

ANSYS v14.5 software was used for the FEM simulation. A $300\ \mu\text{m}$ long open region of neural tube, without any peripheral tissues attached (e.g. surface ectoderm and paraxial mesoderm), was drawn in the 'Geometry' part of the programme (see Chapter 5). In the 'Model' part, a mesh was drawn in a 'Hex Dominant' form onto the structure, and the MHP at one end of the open tube was chosen as a "Fixed Support".

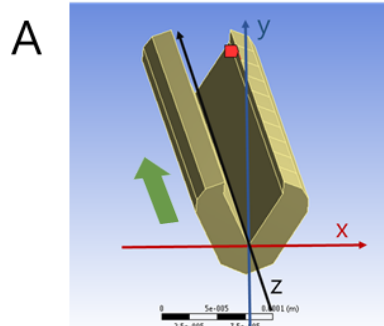
Then, the open tube was designed to become progressively closed, starting from one end, by applying time-dependent displacement conditions to the x co-ordinate points along the NF dorsal edge (points were symmetrical in the medio-lateral axis). The y co-ordinate points (i.e. in the dorso-ventral axis) were 'ignored'. Hence, points at $(-27\ \mu\text{m}, y_1)$ and $(27\ \mu\text{m}, y_1)$ along the z -axis were set to become $(0\ \mu\text{m}, y_2)$ at different times, whereas the y_2 value was left as a blank ('ignored') (Figure 2.2 B). In this way, the dorso-ventral behaviour of the NP during neural tube closure could be modelled naturally, without confining the y axis values (post-closure) of the NF tips to certain values. Otherwise, the modelling could happen in a mechanically unfavourable manner.

The dorsal NF tip on one side of the open tube was divided into ten segments along the longitudinal axis (Figure 6.1), and the complete (end to end) time of zippering was set at 2.2 sec, with a time step of 0.01 sec. Hence, in the simulation, it took 0.2 sec for the NF tips to come into apposition at the closure-initiating end of the open tube, and sequentially 0.2 sec for the completion of each segment's closure. To estimate the

force needed for closure within each segment, the component of the forces that points towards the opposite NF edge face (i.e. dorsal closing force) was taken into account. Force profiles could be plotted, by choosing 'FVECTORS' in the expression part and choosing 'Force' in the output unit, after creating 'User Defined Result' in the 'Solution' part.

Due to the material discontinuity at the longitudinal ends of the modelled tube, valid dorsal closing forces for analysis were only taken from the middle part of the longitudinal axis (i.e. 4th to 7th or 5th to 8th segments).

The analysis of dorsal closing force profiles in the normally closing tube was performed with the following conditions: a 30 μm initial NF tip-to-tip distance across the midline; a 54 μm NP thickness; a NP stiffness of 100 Pa. As this modelling was based on E9.5 embryos, DLHP shape was also included in order to mimic the real morphology of the embryo at this stage. To determine the effect of the reduced *Kumba* basal NP width (see Chapter 4) on the calculated dorsal closing force, the mutant and wild-type open neural tubes were drawn with the same shape, the only difference being the length of the non-bending (straight) lateral NP region, which was 60 μm for mutant and 90 μm for wild-type. The values for initial NF tip-to-tip distance (54 μm), NP thickness (30 μm) and NP stiffness (100 Pa) were not varied for mutant and wild-type. Similarly, when studying the effect of NP thickness, the geometry of the mutant was used as a template and only the NP thickness was varied, from 30 μm to 25 μm , while keeping the other measures unchanged, except that the shape of NF tips was slightly altered to accommodate the change in NP thickness. For the analysis of NP stiffness effects, only NP stiffness was varied, with values of 100, 200, and 300 Pa, while other aspects of the mutant NP geometry were kept unaltered.



B

Right side NP																									
X	Y	Z	X0	DX1	DY1	DX2	DY2	DX3	DY3	DX4	DY4	DX5	DY5	DX6	DY6	DX7	DY7	DX8	DY8	DX9	DY9	DX10	DY10	DX11	DY11
27	65	0	0	-27		-27		-27		-27		-27		-27		-27		-27		-27		-27		-27	
27	65	30	0	-24		-27		-27		-27		-27		-27		-27		-27		-27		-27		-27	
27	65	60	0	-22		-24		-27		-27		-27		-27		-27		-27		-27		-27		-27	
27	65	90	0	-19		-22		-24		-27		-27		-27		-27		-27		-27		-27		-27	
27	65	120	0	-16		-19		-22		-24		-27		-27		-27		-27		-27		-27		-27	
27	65	150	0	-14		-16		-19		-22		-24		-27		-27		-27		-27		-27		-27	
27	65	180	0	-11		-14		-16		-19		-22		-24		-27		-27		-27		-27		-27	
27	65	210	0	-8.1		-11		-14		-16		-19		-22		-24		-27		-27		-27		-27	
27	65	240	0	-5.4		-8.1		-11		-14		-16		-19		-22		-24		-27		-27		-27	
27	65	270	0	-2.7		-5.4		-8.1		-11		-14		-16		-19		-22		-24		-27		-27	
27	65	300	0	0		-2.7		-5.4		-8.1		-11		-14		-16		-19		-22		-24		-27	
Left side NP																									
X	Y	Z	X0	DX1	DY1	DX2	DY2	DX3	DY3	DX4	DY4	DX5	DY5	DX6	DY6	DX7	DY7	DX8	DY8	DX9	DY9	DX10	DY10	DX11	DY11
-27	65	0	0	27		27		27		27		27		27		27		27		27		27		27	
-27	65	30	0	24.3		27		27		27		27		27		27		27		27		27		27	
-27	65	60	0	21.6		24.3		27		27		27		27		27		27		27		27		27	
-27	65	90	0	18.9		21.6		24.3		27		27		27		27		27		27		27		27	
-27	65	120	0	16.2		18.9		21.6		24.3		27		27		27		27		27		27		27	
-27	65	150	0	13.5		16.2		18.9		21.6		24.3		27		27		27		27		27		27	
-27	65	180	0	10.8		13.5		16.2		18.9		21.6		24.3		27		27		27		27		27	
-27	65	210	0	8.1		10.8		13.5		16.2		18.9		21.6		24.3		27		27		27		27	
-27	65	240	0	5.4		8.1		10.8		13.5		16.2		18.9		21.6		24.3		27		27		27	
-27	65	270	0	2.7		5.4		8.1		10.8		13.5		16.2		18.9		21.6		24.3		27		27	
-27	65	300	0	0		2.7		5.4		8.1		10.8		13.5		16.2		18.9		21.6		24.3		27	

Figure 2.2 Example of displacement conditions applied to the modelling.

(A) Image of the mutant NP. The initial NF tip-to-tip distance is 54 μm throughout the longitudinal axis (z-axis, black line). The longitudinal length of the structure is 300 μm . The origin (0, 0, 0) of the axes is located at the MHP of the NP image. The green arrow indicates the direction of closure.

(B) Displacement data of the (x, y, z) coordinates of NF tips at different times. The upper table and the lower table are for the displacement data of the NF tips located on the +ve x-axis (right hand side) and -ve x-axis (left hand side), respectively. The first three columns represent NP (x, y, z) coordinates of the NF tips. A series of 'DX' and 'DY' represents the displacement amount for each x and y at different times. For example, at time step 1, right hand side and left hand side NF tips at z=0 move on the x-axis by -27 and +27, respectively, resulting in the joint of the two NF tips at x=0. At the same time, other points along the z-axis also move with a spatial gradient. Each point also changes with a temporal gradient. Note that DY values are left blanks for 'ignore' function of the modelling.

3. The effects of mechanical manipulation on tissue morphology and cellular shape in the neural plate

3.1. Introduction

3.1.1. Elastic deformation and force relationships during neural tube closure

The application of stress to most materials, including visco-elastic biological tissues, causes them to go through elastic deformation, followed by plastic deformation as the amount of stress increases. Elastic deformation describes the material property of returning to an initial deformation-free state (i.e. reversible deformation) after removal of the stress. In elastic deformation, stress and strain have a proportional relationship (blue arrows in Figure 3.1A), and elastic recoil reveals the existence of a 'recovery force'. Upon applying a larger amount of stress, however, materials become permanently deformed, even after the removal of the stress. Hence, this response is called plastic deformation (i.e. irreversible deformation; orange arrows in Figure 3.1A). If the applied stress continues to increase, then eventually the material comes to the point of rupture.

Neurulation requires the initially flat neural plate (NP) to bend and eventually form a tubular shape after its closure. If the NP goes through a bending process involving elastic deformation, then it should have the property of returning to the initial 'unbent' state through its recovery force. However, if the NP goes beyond the elastic deformation range, and exhibits plastic deformation, then the recovery force will be mostly lost, owing to the presence of permanent deformation. As the neural folds (NFs) come into apposition in the dorsal midline, if the NP is truly under elastic deformation, there should be another force, hereafter defined as the 'NP pull-in force', that pulls the NFs towards each other, counteracting the recovery force that pulls the NFs apart.

A widely accepted model of neural bending involves apical constriction of neuroepithelial cells within the NP (Sawyer et al. 2010). Actomyosin contraction constricts the cell apices causing the apical NP surface area to become reduced relative to the basal area, leading to inward bending of the NP. Previous work in our lab attempted to reverse this potentially elastic deformation, by blocking actin assembly with the drug cytochalasin D. However, no elastic recoil was observed, and the NP continued to close in the spinal region (Ybot-Gonzalez and Copp 1999). This result suggested that the mouse spinal NP may in fact undergo permanent, plastic deformation during closure.

Despite this finding with cytochalasin D, I considered further whether the NP may be under elastic or plastic deformation. Other sources of 'NP pull-in force' might exist that were not affected by the inhibitor. Neural tube closure can be compared to folding of a sheet of paper (Figure 3.1 D) on the assumption that the NP is a homogenous continuous single layer like a sheet of paper. When two adjacent corners of the paper are brought together by folding, it is observed that the rest of the paper partially rolls up, similar to the bending NP. If the folding is released, the paper unrolls owing to the elastic properties of the paper (Figure 3.1 E). Applying this idea to the NP bending, if the NP is under elastic deformation, the NP could return to a more flat state if the closed point (equivalent to the folded junction in the paper model) is re-opened. Based on this prediction, a 'NP pull-in force' might originate from the most recently closed region of neural tube, and function to draw together the elastic NFs in the open NP region.

It is quite difficult to find exactly matching mechanical models for the closing neural tube, but one model, from fracture mechanics, would be a cylinder with a full-thickness crack (elliptical hole) in its wall in which the PNP could be compared to the elliptical hole (Figure 3.1 B). Figure 3.1 C shows the stress magnitude along the major planar axis; at the edge of the elliptical hole the stress (σ_{yy}) is exerted maximally, diminishing with distance from the hole (Boresi and Schmidt 2003). The figure shows only the stress distribution in a planar model, but in a cylinder model the stress distribution would be expected to be closely similar, except that the stress σ would be a function of the wall thickness of the cylinder, the inner radius of the cylinder, and the stiffness of the wall.

Collectively, from the two models (paper folding and cracked cylinder), it can be assumed that the largest amount of stress is imposed on the closing point of the neural tube, and that the stress diminishes with distance towards the caudal end where the NP is increasingly flat. To test this hypothesis, I designed an experiment in which the most recently closed neural tube roof was incised. I hypothesised that if the NP is under elastic deformation then the NP at the closing level of the PNP would spring apart most, whereas the more caudal NP would show proportionately less recoil. The analysis was based on gross measurements of NF proximity ('dorsal transverse opening') in the dorsal midline, the bending degree at the dorsolateral and median hinge points of the NP, and cell morphologies at different dorso-ventral and rostro-caudal levels of the NP. In all

cases, the comparison were made on individual embryos, before and after neural tube incision.

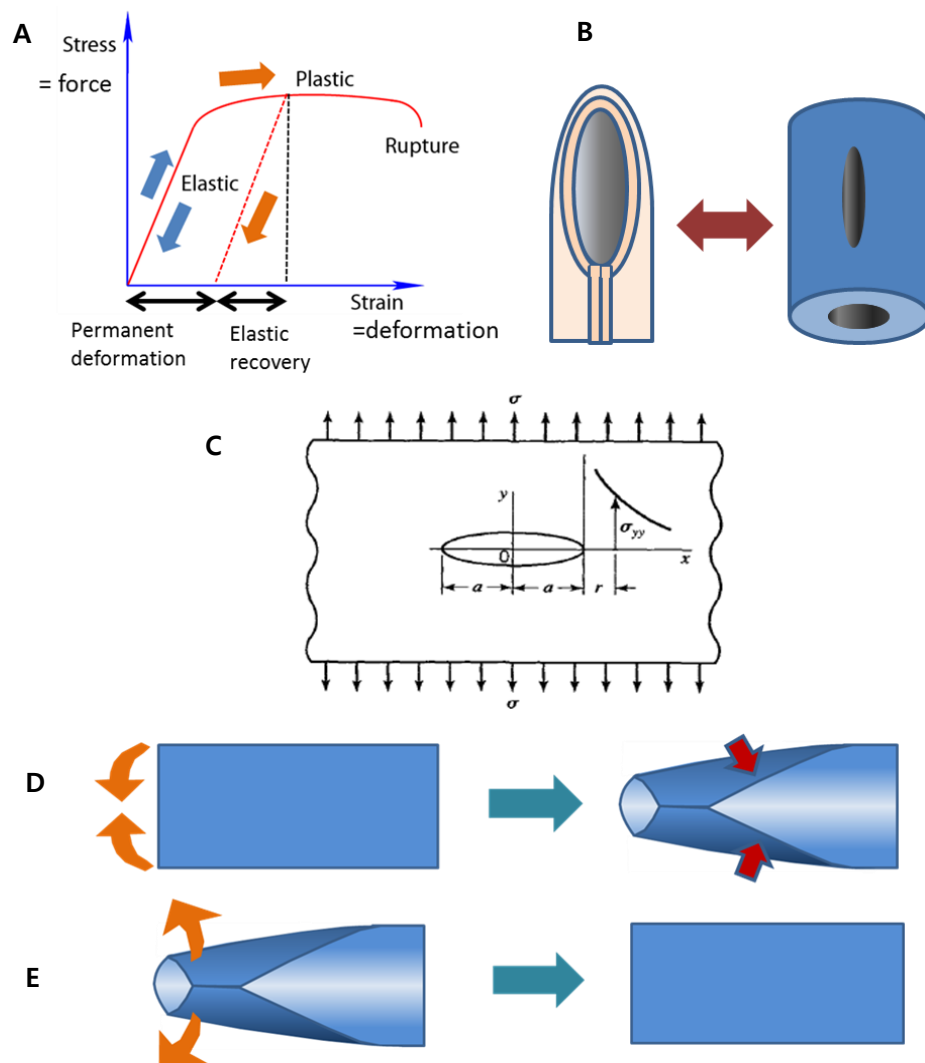


Figure 3.1 Force relationships in neural tube closure and its corresponding models.

(A) Stress vs Strain diagram.

(B) Analogy between a cylinder that has an elliptical hole through the wall and the closing neural tube.

(C) Stress along the major axis of an elliptical hole in an infinite plane that is being pulled with uniform stress σ . Figure adopted from (Boresi and Schmidt 2003).

(D-E) Paper folding model that can be compared to neural tube closure. When the paper is folded at one end (orange arrows), non-closed regions (red arrows) also roll up (D). When the folding is released, the paper becomes flat as before if the paper sheet is elastic (E).

3.2. Results

3.2.1. Tissue morphology change after incision

3.2.1.1. The neural plate is elastic and its bending depends in part on a 'pull-in force' from the recently closed neural tube

The DLHPs appear in E9.5 wild-type embryos, and their formation is thought to play a crucial role in neural tube closure because E9.5 *Kumba* mouse NP does not develop DLHP and fail to close. Therefore, mechanistic properties of the NP were investigated on E9.5 wild-type embryos in this chapter, and the analysis results were compared with E9.5 *Kumba* embryos afterwards (Chapter 4).

Embryos were fully dissected from their extraembryonic membranes and the rostral-caudal position of the neural tube closure point was labelled using small, bilateral Dil marks made by injecting Dil just beneath the surface ectoderm with a micro-pipette. This allowed the morphology of the NP at the closing level of the PNP to be compared before and after incision. Incision was performed using a fine glass needle which was inserted in the dorsal midline of the closed neural tube, followed by a caudal ward slicing movement up to the closing point of the PNP to incise the neural tube roof and overlying surface ectoderm (Figure 3.2A-C).

Time lapse imaging was performed during the incision experiment, in order to determine how rapidly, and to what extent, the closing NFs might spring apart from each other following incision. Curvature of the body axis can alter the rate of spinal closure in both chick and mouse embryos (van Straaten et al. 1993), perhaps by affecting the tension in the neural tube roof. To determine whether curvature might be a factor influencing the outcome of incision experiments, I performed incisions not only on whole embryos but also on isolated caudal regions, which had been detached from the body by cutting approximately at the level with the most recently formed somite. In both groups, immediately after the incision ($t = 0$ in Figure 3.2 D), the NFs were observed to spring apart to a distance of 30-40 μm , and then to slowly increase their distance from each other to a further 10 μm over the subsequent 45 sec. In whole embryos, that had a fully curved trunk, the initial NF distance increase was greater than in isolated caudal regions (Figure 3.2 D). However, elastic re-opening was also found in the isolated caudal region, arguing that curvature effects are responsible for only a small part of the observed elastic recoil.

Incision length was varied and its effect on the re-opening of the neural tube was investigated. NF tip-to-tip distance was measured, with 12 μm longitudinal intervals, on the image of the whole embryo that was fixed in Bouin's solution after incision. Longer incisions generated greater springing apart of the NFs, although a 'short cut' of 321 μm produced 70% as much recoil as a 'long cut' of 669 μm (Figure 3.3 A). This suggests it is the most recently closed neural tube that is the site of the major NP pull-in force. It was noticeable that the dorsal transverse opening of long cut, short cut and unincised embryos all converged towards a similar value, about 170 μm caudal to the closing point (Figure 3.3 A). This corresponds to approximately half-way along the PNP, and indicates that the mechanical effects of the incision become attenuated with distance.

Figure 3.2 The NP springs apart rapidly after incision.

(A) Schematic of incision experiments and force relationships in the NP before and after incision. If the NP is under elastic deformation, a recovery force that pulls apart the neural folds (light blue arrows) will act upon the bent NP. This recovery force should be balanced by an equal and opposite NP pull-in force (dark blue arrows) for the neural folds to be stably elevated. Post-incision, the NP pull-in force is mostly lost, leaving the recovery force unopposed, leading to elastic springing apart of the folds.

(B-C) NF distance at the Dil-marked closing level before and after incision. NF distance (yellow dashed line) 40 sec after incision (C) is longer than the initial NF distance (B).

(D) NF distance change (NF distance after incision - NF distance before incision) at the closing level over time (sec) for the whole embryo (blue line) and for the isolated caudal region (red line). Note that most of the distance change occurs in just a few seconds. N: the number of embryos analysed.

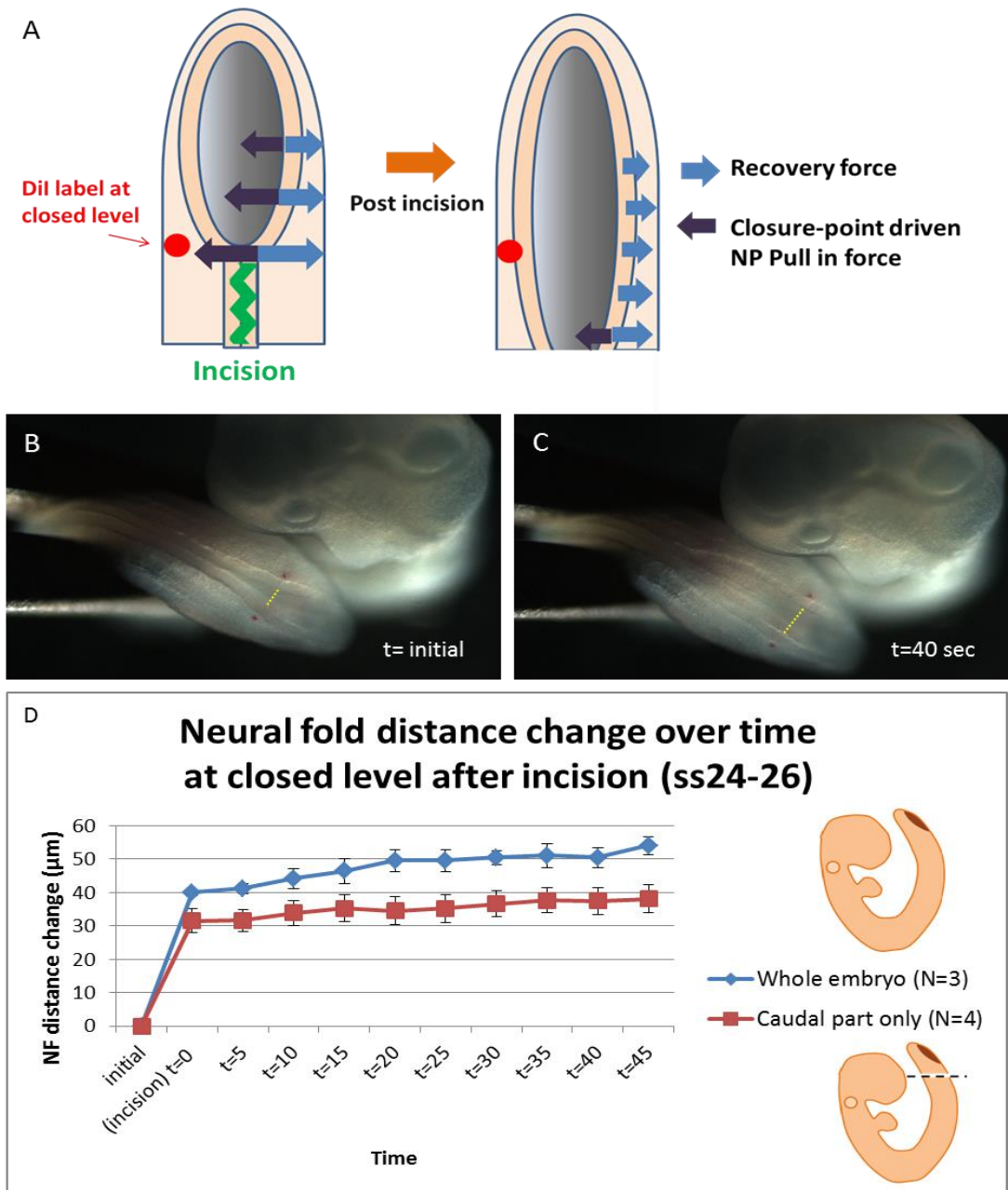


Figure 3.2. The NP springs apart rapidly after incision.

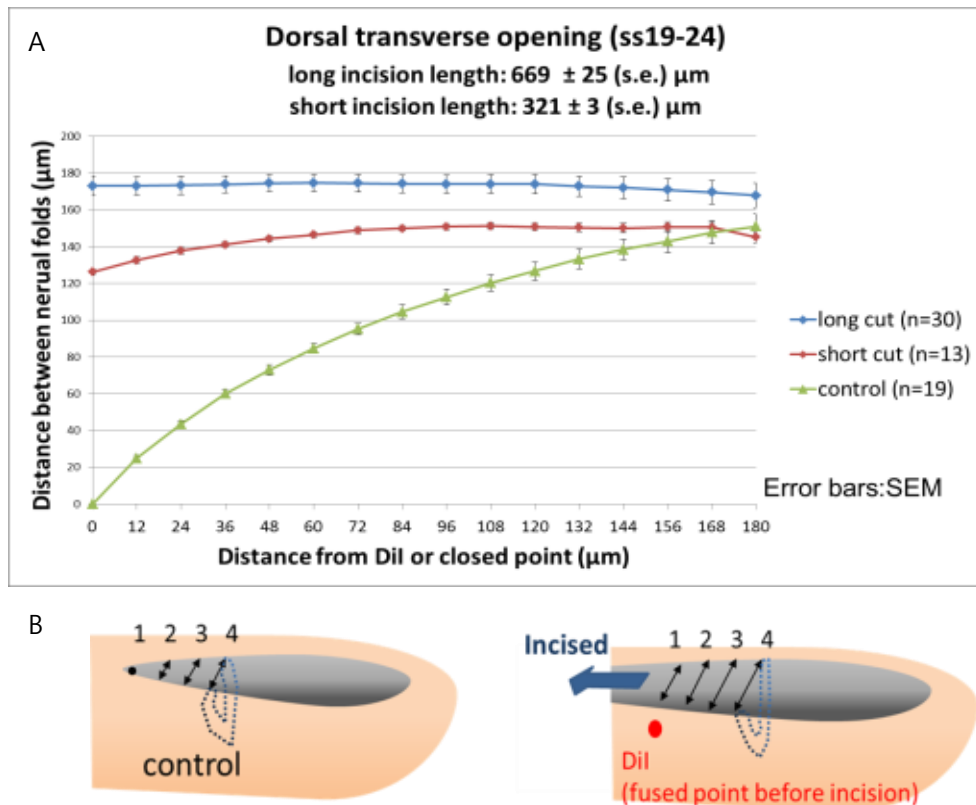


Figure 3.3. Dorsal transverse opening varies with incision length, and becomes attenuated caudally along the PNP.

(A) Dorsal transverse opening for control and incised embryos from the closing (Dil-labelled) level towards the caudal end. Short cut (incision) embryos showed a smaller re-opening than long cut (incision) embryos. n: the number of embryos analysed.

(B) Schematic of control and incised embryos.

3.2.1.2. Dorsal fusion process affects dorsolateral bending and midline bending

Based on the finding of instantaneous dorsal transverse re-opening after neural tube roof incision, it can be inferred that a recovery force exists within the bent NP, matched by a NP pull-in force that counteracts the recovery force, and which could be eliminated by incising the neural tube roof. Therefore, it appears that the NP pull-in force originates from most recently closed neural tube roof.

To determine whether the NP pull-in force is necessary for NP bending, ss19-24 (E9.5) embryos, where both MHP and DLHPs are present, were collected, and the degree of bending at the MHP and DLHPs was measured on sections of embryos fixed after incision, or in controls that were unincised. While it was straightforward to measure the angle of MHP bending, the DLHP was not bent sharply enough for its angle to be measured conventionally (Figure 3.4 A). Therefore, the area (A) encompassed by an outline of the apical surface of the NP and the line connecting the NF tip with the MHP was measured, and then divided by the length of the NF tip-to-MHP line (d). The value A/d was defined as the bending degree (β) (Figure 3.4 C).

Incision length was measured for each individual embryo and the mean (\pm SEM) values were: 275 ± 18 (SEM) μm for short incision and 670 ± 42 μm for long incision for DLHP analysis; 270 ± 16 μm for short incision and 696 ± 41 μm for long incision for MHP analysis. The reason for these slight differences was that either DLHP or MHP could not be measured in a small number of the embryos.

Following incision, both DLHP and MHP were found to lose a significant amount of bending degree and bending angle, respectively (Figure 3.4 E-H). In particular, DLHP bending was greatly reduced even after short incision, with similar results obtained in long incision embryos (Figure 3.4 E,G). In contrast, MHP bending angle reduced roughly in proportion to the length of the incision, with short incisions producing a less marked effect than long incisions (Figure 3.4 F,H).

Moreover, while DLHP bending degree in long incision, short incision and control embryos converged towards the caudal end of the PNP, MHP bending angles did not show similar convergence. Instead, the differential effects of the long and short incision lengths were maintained along the PNP axis. Hence, at 100 μm from the closure point,

the difference in MHP angle was almost as marked between groups as at the closure point itself (Figure 3.4 F).

In conclusion, the incision experiments show that the closing NP exhibits elastic properties: it can return to its initially less bent state once the NP pull-in force is removed, so that the recovery force is unopposed. Concomitantly, the recently closed neural tube roof creates a force field that counteracts the recovery force and partly contributes to NF apposition and bending of the NP (both at DLHPs and MHP) in a distance-dependent manner along the PNP. Strikingly, however, even after incising the neural tube roof, both the dorsolateral and medial NP still exhibit some degree of bending (Figure 3.4 B), which suggests that endogenous changes (i.e. plastic changes) have occurred within the NP during neural tube closure.

Figure 3.4 DLHP bending degree and MHP bending angle reduce after incision.

(A) Section at closing level of an unincised embryo (ss22). The angle of DLHP bending (yellow) is harder to measure in a conventional way than that of MHP (red), since only the latter forms a sharp angle.

(B) Section of previously closing level of an incised embryo (ss22). Red-circled region indicates that DLHP is still present after incision.

(C-D) DLHP bending degree (C) and MHP bending angle (D) measurement methods.

(E) Change in DLHP bending degree after incision. From the Dil point, the bending degree of both short and long cut embryos were markedly reduced compared with the unincised control. The bending degree of all three groups converged towards the caudal end.

(F) Change in MHP bending angle after incision. The response to incision is quite different from the DLHP: there is a consistently greater effect of long cut than short cut, and there is no appreciable convergence of the bending angles in the three groups towards the caudal end of the neuropore. For MHP, the gaps between each stay almost constant through the longitudinal axis. n values show number of embryos in each group. The data in the red-dashed boxes are separately bar-graphed in (G-H).

(G-H) For DLHP bending degree at Dil-labelled level (G), the value of the unincised control is significantly larger than those of both short and long cut embryos. For MHP bending angle at Dil-labelled level (H), the value of the unincised control is significantly larger than those of short cut and long cut embryos, and the value of short cut embryos is also larger than that of long cut embryos ($p < 0.001$ for both groups, 1 way ANOVA with Holm-Sidak multiple comparison procedures (significance level $p = 0.05$)). *: $p < 0.05$. Error bars represent standard errors. n: the number of embryos analysed.

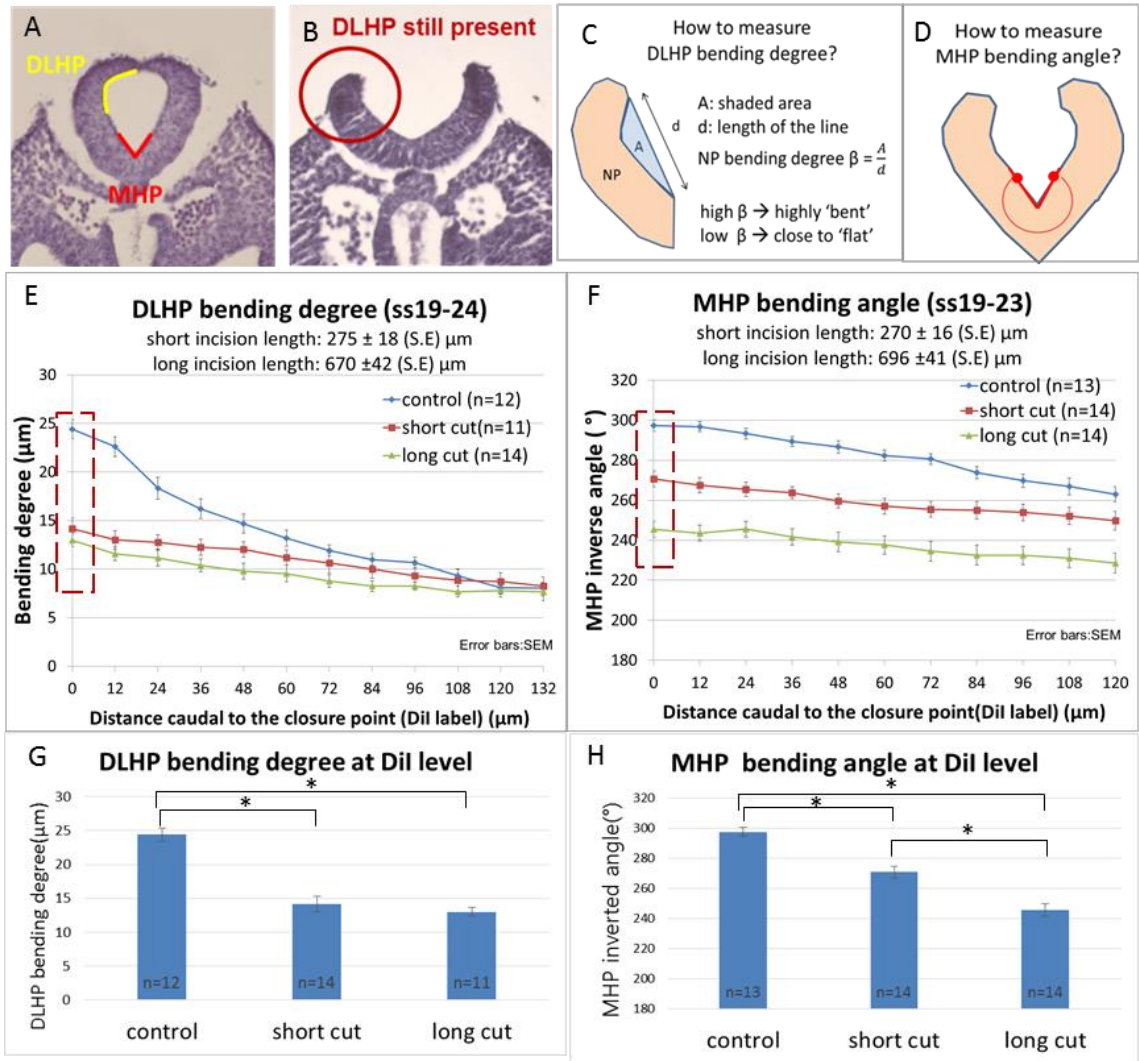


Figure 3.4. DLHP bending degree and MHP bending angle reduce after incision.

3.2.2. Cellular shape change after incision

Several lines of evidence suggest that the closing point of the PNP experiences maximum physical stress force, and that this diminishes with distance along the PNP. The incision experiment has confirmed that the largest effects on NP bending occur at the point of closure, and this result is also consistent with the paper folding/unfolding model. Moreover, the modelling study (see Chapter 6) also reveals how the magnitude of dorsal closing force (i.e. NP-pull in force) changes along the longitudinal axis. For neural tube closure to progress, the NP-pull in force must surpass the recovery force at the rostral end of the PNP, and hence the closure point experiences the greatest amount of stress.

The next goal was to determine whether the stress impinging on the closing point affects the NP at the cellular level, as well as at the tissue level in terms of NP bending. Dorso-ventral cell curvature and nuclear circularity were compared between incised and unincised embryos at the closing level and more caudally, at a more open level of the PNP. *Grhl3^{cre/+};ROSA^{YFP/+}* mice were used for this analysis, as they show a mosaic pattern of cytoplasmic YFP expression in the NP which facilitated analysis of individual cell shapes.

3.2.2.1. Cell curvature degree responds to external mechanical stress

Cell curvature degree was quantified by a similar method as DLHP bending degree. A straight line was drawn to connect the two extremities of a NP cell with another curved line dividing the area of the cell into roughly two halves (Figure 3.6 A). The area enclosed by the two lines was divided by the straight line length to generate a measure of cell curvature degree. Plus and minus signs were assigned to dorsally and ventrally curved cells, respectively.

In unincised control embryos, highly positive mean cell curvature values were observed in both dorsal and ventral NP halves at both closing and open PNP levels. The highest values were in the dorsal NP at the point of closure (Figure 3.5 A, 3.6 B). Hence, normal embryos exhibit dorsal curvature of NP cells throughout the entire PNP region.

Following neural tube incision, cell curvature decreased significantly in the dorsal NP half, particularly at the closing level, where DLHPs are present and where curvature was almost 50% less after incision (Figure 3.5 A, 3.6 B). Cell curvature also decreased significantly in the dorsal NP at the open level. In contrast, cell curvature did not change significantly after incision in the ventral NP half, either at closed or open PNP levels

(Figure 3.6 B). Hence, the curvature of individual NP cells responds to a reduction in external mechanical stress, with the most marked response in the dorsal NP close to the point of closure. The finding argues strongly that the dorsal NP at the site of closure is under maximal tension, compared with other NP regions.

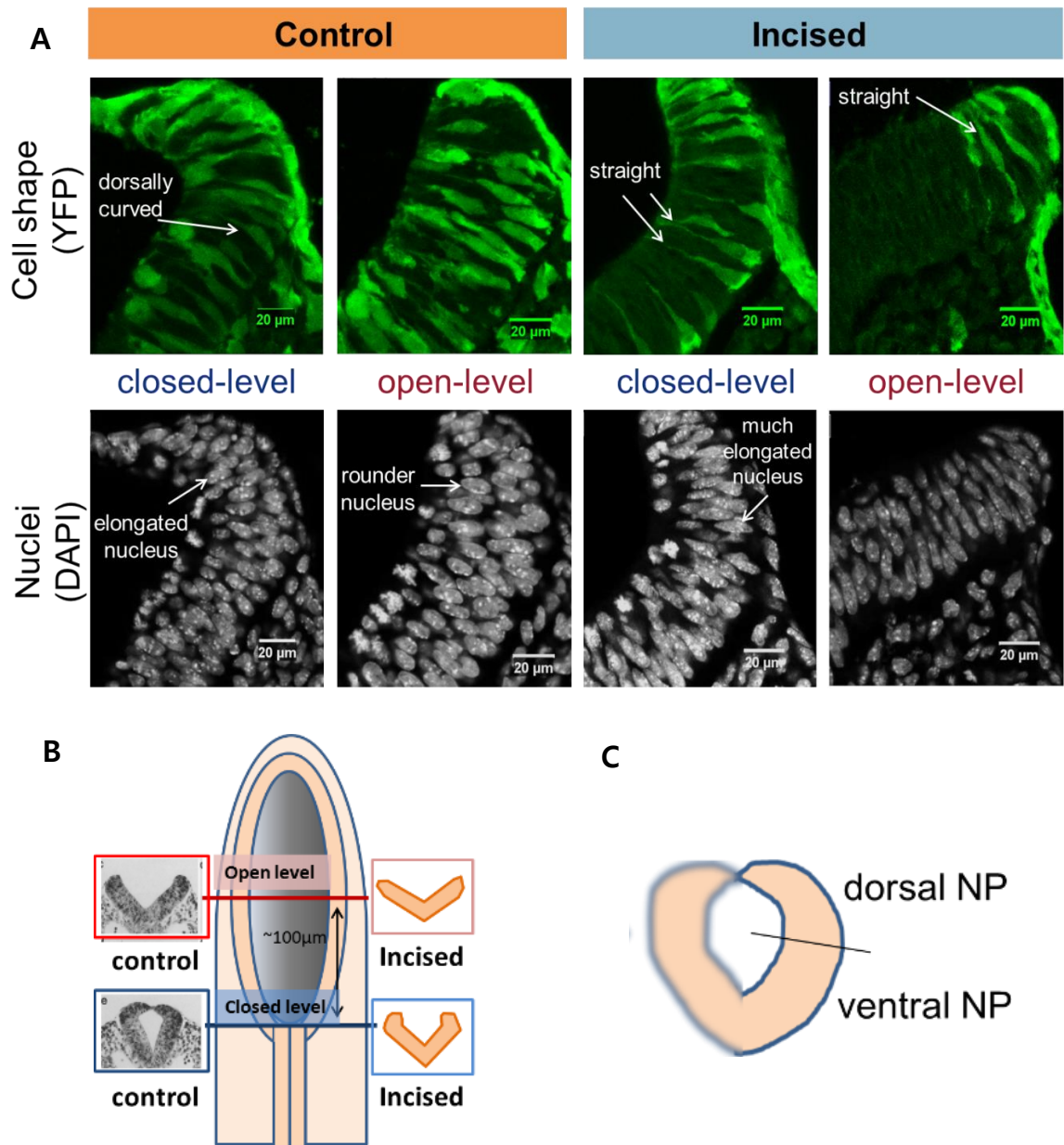


Figure 3.5. Cellular and nuclear shape changes after incision.

(A) Images of cell and nuclear shape before and after incision. Scale bars represent 20 μm.

(B) Schematic of the closing level and the open level of the PNP for control and incised embryos. The open level is approximately 100 μm caudal to the closing level.

(C) Division of the NP into dorsal and ventral halves for analysis.

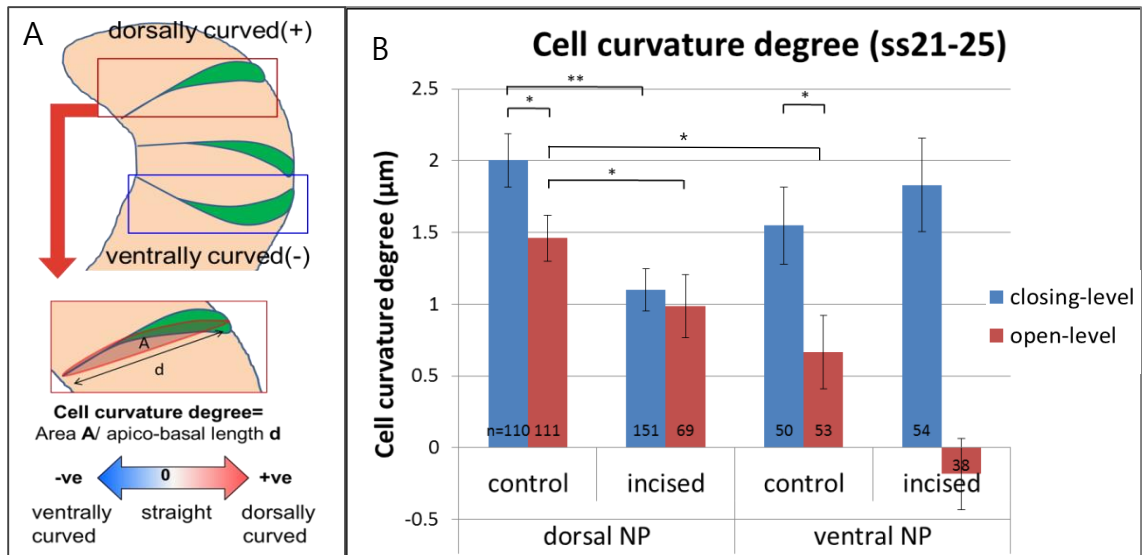


Figure 3.6. Cell shape becomes less curved after incision particularly in the dorsal NP.

(A) Schematic of how cell curvature degree is measured. Dorsally curved cells were assigned a +ve value, and ventrally curved cells were assigned a -ve value.

(B) Cell curvature degree change before and after incision for closing/open levels and dorsal/ventral NP. For unincised embryos, NP cells at the closing level were significantly more dorsally bent than cells at the open level (t-test for both dorsal and ventral halves). Particularly in the dorsal NP, cell shapes become more straight after incision at both closing and open levels (t-tests; *: $p < 0.05$, **: $p < 0.001$). n: the number of cells scored.

3.2.2.2. Nuclear elongation is associated with DLHP formation

Nuclear shape (circularity) was measured as a possible marker of cell compactness. It was reasoned that nuclei may become elongated particularly if a large number of cells are 'crowded' within a limited space. However, before drawing conclusions about cell packing based on nuclear shape, it first needed to be verified whether the volume of a nucleus remains constant while its shape changes. If nuclear volume were to change with cell packing, then nuclear shape might be an unreliable indicator. It proved impossible to measure the volume of individual nuclei using confocal z-stacks due to the ambiguity of nuclear boundaries in the 3D-reconstructed volume. On the other hand, if nuclear volume remains constant as shape change occurs, then nuclear lengthening should correlate closely with nuclear narrowing, as nuclei adopt lower circularity values.

To explore this prediction, mathematical modelling was used to predict how the Feret diameter (longest distance of an object) of an originally spherical object may vary with its circularity, whilst maintaining volume constant. Circularity was assessed from the cross section that passes through the central longitudinal axis of the object (Figure 3.7 C). From observations on nuclei in z-stacks, an elongated nucleus was found to most closely resemble a capsule-shaped object (Figure 3.7 D): a cylindrical body with a hemisphere at each end. As a result of this modelling, it was found that when the Feret diameter of the object increased (i.e. elongation of the capsule with reduced width), the object's circularity decreased, while the volume was kept constant (Figure 3.7 B). When the modelling result was compared with the actual nuclear data from z-stack analysis, it was found that the nuclear circularity also had an inversely proportional relationship with Feret diameter (Figure 3.7 A). This suggests that, at least for 20-23 somite stage (ss), nuclear volume remains relatively constant in the NP.

However, it was not straightforward to perform regression analysis on the actual data (nuclear circularity vs Feret diameter) as the polynomial degree could not be defined from the modelled equation (Figure 3.7 C). In the modelling, the equation of circularity of the capsule could not be algebraically expressed as Feret diameter, and hence the relationship between these two can only be solved in a numerical way by varying the c value from 0 to 1. Here, the c value represents how much elongated the capsule is; the closer the c value is to 0, the more elongated the shape is. Matlab was used to solve this, and to plot the result (Figure 3.7 B). In non-mathematical terms, it would be expected

that a nucleus of constant volume would remain spheroidal, at its lowest energy state, under normal stress-free conditions and would be unlikely to elongate, and adopt a higher energy state, unless forced to do so by tissue packing constraints. Therefore, this modelling result suggests that the volume of a nucleus remains more or less constant in the NP and that the observation of nuclear elongation is best explained as an effect of external pressure, probably caused by dense cell-packing conditions in the tissue.

In control (unincised) embryos, mean nuclear circularity in the dorsal NP was significantly less at the closing level of the PNP (where DLHPs are most prominent) than at the more caudal, open level (Figure 3.8 B). This suggests that cells may become increasingly close-packed within the NP while the DLHP forms during undisturbed development. Incised embryos were then studied in order to distinguish the contribution to such nuclear circularity changes from endogenous (within NP) and exogenous (e.g. from the recently closed neural tube) influences. Following incision, mean nuclear circularity reduced even further than in unincised controls, at both closing and open levels (Figure 3.8 B). The dorsal NP at the closing level showed the greatest reduction in nuclear circularity following incision, to a mean value that was smaller than any other dorso-ventral or rostro-caudal NP region. All other regions showed reduced nuclear circularity after incision, but there was no difference in circularity of the ventral NP between closing and open levels. These findings suggest that nuclei become increasingly elongated (lower circularity) specifically in the dorsal NP of the closing level, where DLHPs form, and that this is an endogenously-driven change that is partially opposed by the NP pull-in force from the closed neural tube. When the NP pull-in force is abolished by incision, and any 'tissue stretching' effect is removed, the tendency to nuclear elongation (and closer cell packing) is accentuated.

The finding of an even more elongated nuclear shape in the dorsal NP after incision appeared counterintuitive - it was originally expected that, upon removal of the exogenous NP pull-in force, nuclei would 'relax' and become more circular. To investigate why this did not occur, the length and cell (nuclear) number were measured within the surface ectoderm (SE) that contacts the dorsal-most NP (Figure 3.9 A,B). Where DLHPs were present, at the closing level, the SE was found to be significantly longer than at the open level. Moreover, after incision, the SE reduced in length becoming similar to the value for the open level before incision. In order to know whether the elongated SE pre-incision was due to an increased cell number, or a similar number of 'stretched' cells, the

SE length was divided by the number of nuclei within the tissue (Figure 3.9 B). At the closing level of the PNP, the value of SE length per nucleus (Figure 3.9 C) before incision was found to be significantly greater than for the closing level after incision, and also greater than the value at the open level before incision. This result strongly suggests that during DLHP formation, each cell in the SE becomes stretched, and that the NP pull-in force from the recently closed neural tube is the main source of this SE cell stretching. In conclusion, the process of DLHP formation involves NP cells decreasing their nuclear circularity, as cell packing increases. Simultaneously, the NF (including the SE layer) is stretched by the NP pull-in force and, upon incision, the NP volume within the DLHP region reduces, leading to further nuclear elongation as cells become even more closely packed.

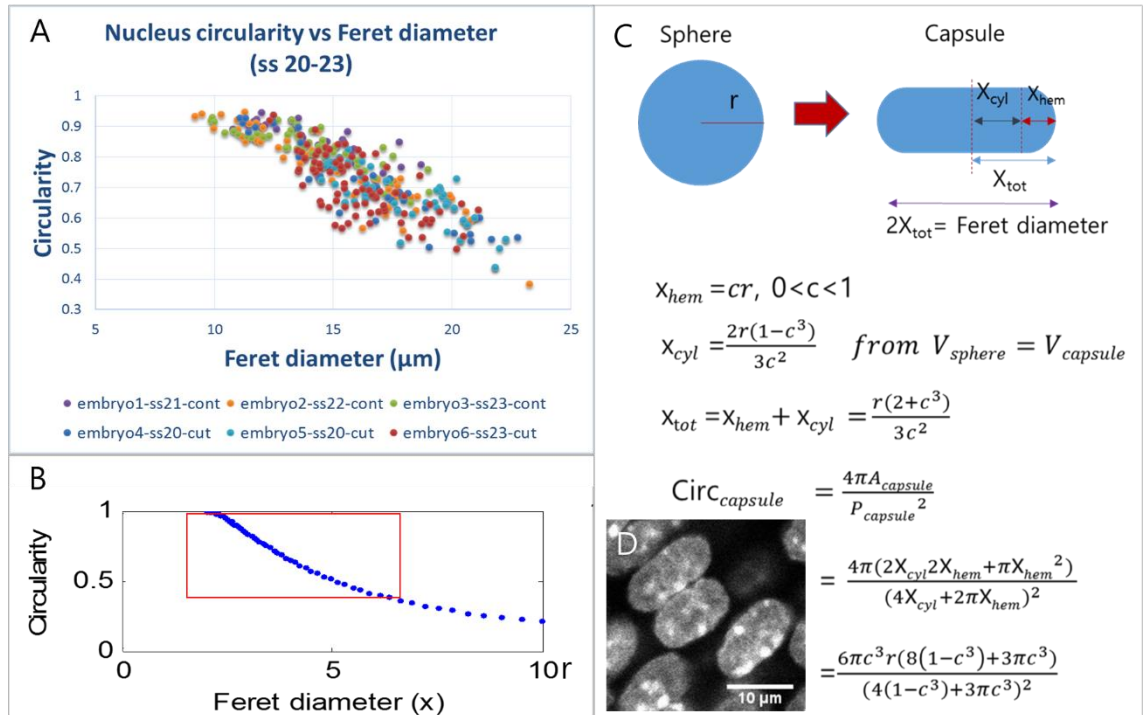


Figure 3.7 The relationship between circularity and the Feret diameter of a nucleus.

(A) Nuclear circularity plotted against nuclear Feret diameter from actual confocal z-stack data.

(B-C) Inversely proportional relationship between circularity and Feret diameter from modelled data (B) when a spherical object becomes elongated while maintaining a capsule shape (C) and with constant volume. The red rectangle in (B) corresponds to the circularity range of the experimental nuclear data. Since the equation of $\text{Circ}_{capsule}$ (circularity of the capsule) can not be algebraically expressed as x_{tot} , the relationship between $\text{Circ}_{capsule}$ and x_{tot} can only be solved in a numerical way by varying the value c from 0 to 1. Matlab was used for solving this, and the result is the graph (B).

(D) Magnified views of nuclei. An elongated nucleus adopts a capsule shape. Scale bar represents 10 μm .

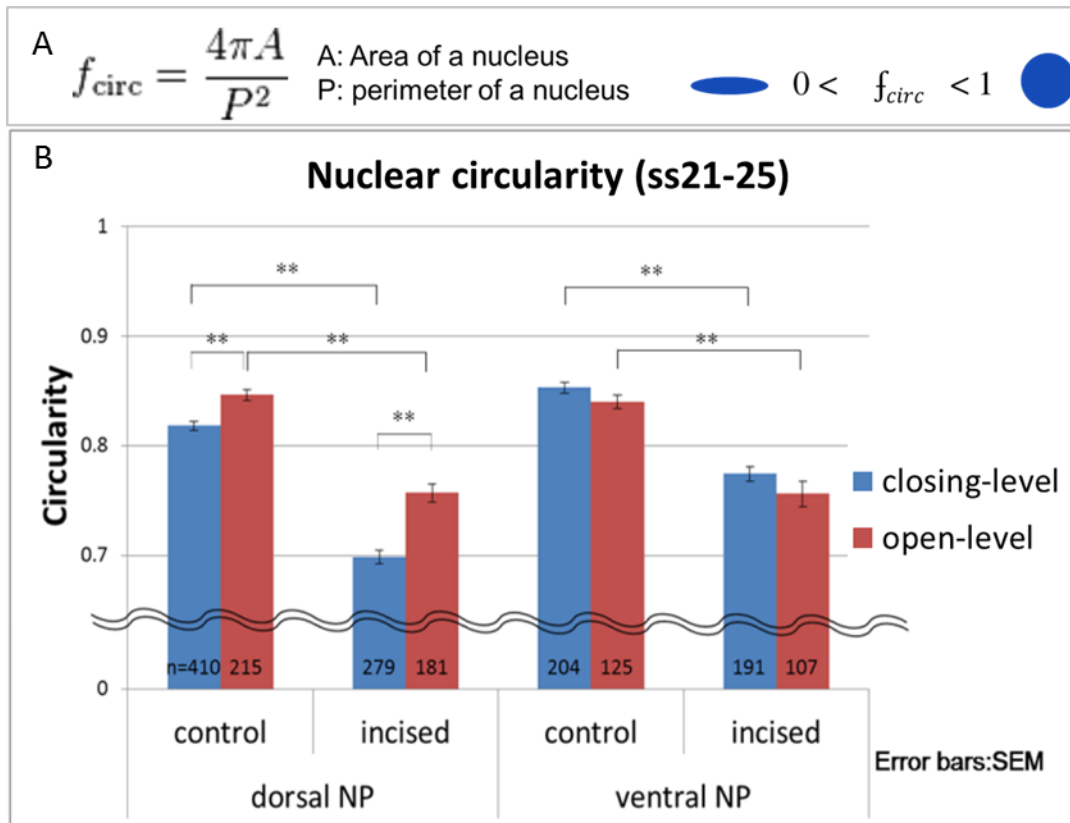


Figure 3.8 Nuclear circularity decreases after incision.

(A) The equation for circularity measurement. The closer the value is to 1, the more circular the object is.

(B) Nuclear circularity for closing/open level and dorsal/ventral NP. In general, nuclei were more elongated (less circular) in incised embryos than in unincised controls. Particularly in the dorsal NP, nuclei were more elongated at the closing level than at open level (t-test; **: $p < 0.001$). n: the number of nuclei scored.

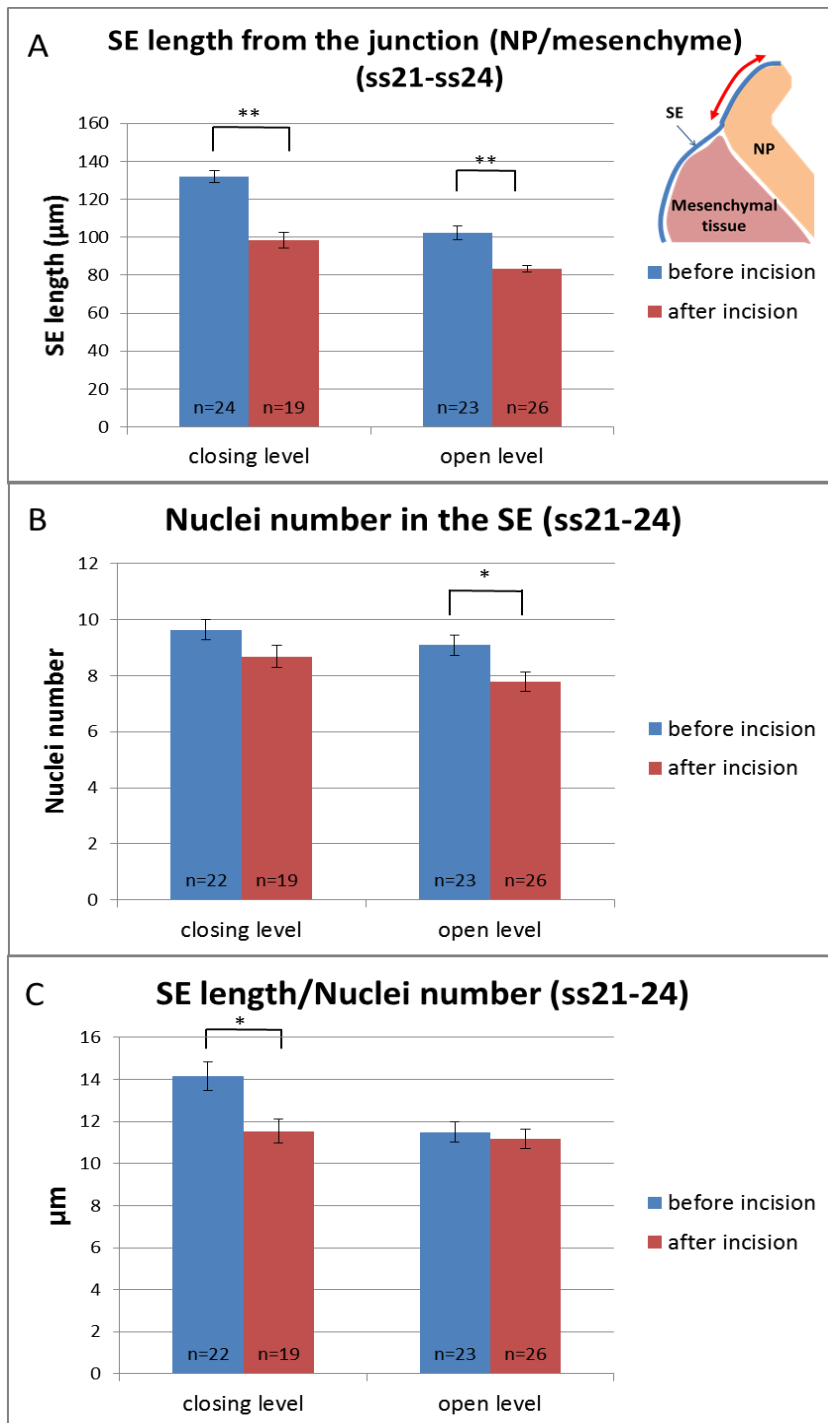


Figure 3.9 Surface ectoderm in contact with NP reduces in length after incision.

(A) SE length, from the junction with mesenchyme to the NF tip (red arrow in the diagram at top right), decreased after incision for both closing and open levels.

(B) Nuclear number in the SE region.

(C) SE length/nuclear number. Only the closing level showed a significant reduction after incision. n = number of NP sections analysed. t-tests: *: $p < 0.05$, **: $p < 0.001$.

n: the number of the medio-lateral half (either left or right) of the NP sections scored.

3.3. Discussion

3.3.1. Tissue morphology change after incision

In this thesis, mechanical properties of the NP were investigated through incision of the recently closed neural tube roof. Incision *in vivo* has been previously performed on different animal models and organs. For the early embryonic chick brain, thin slices of the brain tube were taken and their dorsal roofs were incised (Xu et al. 2010). Then, circumferential residual stress was estimated from the opening angle of the brain slice at different stages and regions of the brain. During heart development in chick embryos, the contractile role of the endodermal tissue layer in heart tube assembly was examined by making a linear incision at the medial point of the anterior intestinal portal (Varner and Taber 2012). Then the angles of triangle-shaped wounds were compared between control and blebbistatin (myosin II inhibitor)-treated embryos as a means of estimating contractility of the endodermal layer. While incisions in these two experiments were mainly intended to examine the elastic properties of the tissue itself, in my work incision was used to investigate how stress in the recently closed region of the spinal neural tube mechanically affects the structure and morphology of the adjacent open PNP region. In this chapter, the incision approach was taken with normally developing embryos. However, this strategy was also employed to gain insight into the mechanism of failed neural tube closure in *Zic2*^{ku/ku} embryos (see Chapter 4).

Methodology issues

The closing neural tube of E9.0-9.5 embryos is characterised by NP bending at the DLHPs and MHP. Previously, the DLHP bending angle was measured by drawing tangent lines on both dorsal and ventral sides of the NP and measuring the angle of intersection (Ybot-Gonzalez et al. 2002). However, from my observation, the NP regions dorsal and ventral to the DLHP were not always straight, and so it was difficult to define the precise points where tangent lines should be drawn. Similarly in Xu et al.'s (2010) work using chick embryo brain slices, the stiffness of the brain tube was estimated after incision by measuring the opening angle, which was defined as the angle between the two lines that connected the midline point to each neuroepithelial tip. However, large error bars (S.D: \pm minimum 20°) in their opening-angle results imply that this angle measurement method was subject to considerable inaccuracy. Therefore, I invented my own method for quantifying DLHP bending by measuring the area encompassed by an outline of the

apical surface of the NP and the line connecting the NF tip to the MHP. As the area was divided by the length of the NF-MHP connecting line, the final value still had the unit of length. However, during and after measurement, the bending degree values from all images were uniformly converted to micrometers, so that it was possible to compare the values between different sections and embryos.

For quantification of MHP bending, the method used for DLHP bending degree measurement was not suitable as it was less straightforward to define two clear reference points than for the DLHP bending degree measurement. My closest attempt was to set the point that lies 1/3 of the length along the apical surface of each NP from the MHP as a reference point and then to connect the points on the two hemi-NPs across the neural groove. The triangular area encompassed by the line and the apical surfaces of each hemi-NP was divided by the length of the line. However, I found that the reference points varied between sections as the NP length changed along the longitudinal axis, resulting in large variance in the area encompassed within. This method was therefore abandoned.

As an alternative, based on the finding that the NP region adjacent to MHP (i.e. non-bending region) was relatively straight, it was possible to measure the angle of the MHP by drawing two lines lying on the apical surface of the non-bending NP region, and measuring the angle between them.

There are some complications when comparing the bending degree in DLHP with that in MHP as the two values are different entities; DLHP bending degree has the unit of micrometer and MHP bending degree has the unit of angle (°). However, the both entities logically describe how much either DLHP or MHP is geometrically bent and at least the trend difference in each group can be compared.

Implications and interpretations of the incision experiments

An elastic NF re-opening was observed after incision of the recently closed neural tube roof. This result allows two conclusions to be drawn regarding the closing mouse PNP: first, that NF elevation towards the midline is not entirely the result of plastic changes within the NP itself and, second, that tension exists dorsally within the closed neural tube that helps bring the NFs into apposition.

It was previously proposed that an increase in dorsal tension in the curved spinal region is closely associated with failure of neural tube closure in the *curly tail* mouse (Brook et al. 1991). Therefore, in order to determine the effect of axial curvature on the

elastic re-opening after incision, the neural tube was incised in isolated caudal regions as well as in whole embryos. While relatively little difference in NF re-opening was observed between caudal regions and whole embryos, it should be noted that, in E9.5-E10 embryos (ss24 and above), not only the trunk but also the caudal region itself exhibits some dorso-ventral curvature. Therefore, it is not possible to completely exclude the effect of axial curvature when interpreting the incision results.

Considering DLHP bending degree, it was shown that the values in embryos with short and long incisions were quite similar and did not differ from each other as much as the MHP bending angle values, which were significantly more affected by long than short incisions at the closing level of the PNP (Figure 3.4 E,F). Based on the fact that the short incision lengths for the analysis of DLHP bending degree and MHP bending degree are nearly the same, this result suggests that DLHP bending reacts more sensitively to the incision than MHP bending, even if the incision is short. In order to understand the reasons for this, the NP pull-in force acting on the NF tip was calculated along the longitudinal axis by a modelling approach (see Chapter 6). It was found that the force is the largest around the closing point, and diminishes with distance along the PNP (Figure 6.1). The fact that the DLHP is physically closer to the focal point of NP pull-in force than the MHP can explain why the DLHP was possibly more affected even by the short incision than the MHP, as incision eliminates the NP pull-in force (provided the incision is long enough). In support of this idea, FEM modeling revealed that the dorsal closing part is going through larger amount of stress (Figure 6.2) and deformation (Figure 6.3) than the ventral part. Based on these modelling results, therefore, it can be inferred that the dorsal closing region would release more energy than the ventral region after incision, perhaps with a greater recoil. Similarly, the physical effects of incision will also be, in the longitudinal axis, inversely proportional to the distance from the incision point, and hence the incision effects will be attenuated towards the caudal end. This can explain why DLHP bending degrees of incised and control embryos converge towards the caudal end.

In contrast to the DLHP, MHP bending angles uniformly decreased for different incision lengths and did not converge towards the caudal end. Considering that the NP pull-in force is nearly zero near the caudal end, regardless of incision, this result suggests that the MHP re-opening is not particularly associated with the dorsally acting NP-pulling force. Rather, it behaves according to recovery force that constantly acts to 'unbend' the bent NP sheet. For example, in embryos with long incisions, the whole NP tissue towards

caudal end will be free from the stress that is created from the recently closed neural tube. Hence, the NP will be only under the influence of the recovery force, which results in the wide re-opening of the MHP. On the contrary, in control embryos, the whole NP tissue will be still under stress originated from the closing point and the stress interferes with the recovery force, which resulted in a smaller MHP re-opening than in incised embryos.

3.3.2. Cellular shape change after incision

3.3.2.1. Cell curvature degree responds to external mechanical stress

Cellular shape change analysis was made possible in this study by the finding that *Grhl3^{cre/+};ROSA^{YFP/+}* mice express a mosaic pattern of YFP in the NP. Other experiments in this thesis use an alternative approach to obtaining mosaic YFP expression: electroporation of a GFP-expressing plasmid vector (see Chapter 4). However, this is a technically difficult procedure, and so the genetic YFP-expressing cross was used for the initial, most extensive cell shape analysis in the present chapter. It should be noted, however, that there is currently no proof that NP cells in *Grhl3^{cre/+};ROSA^{YFP/+}* embryos express YFP in a random manner, although there is no obvious pattern to the YFP expression.

In view of the existence of interkinetic nuclear migration in the higher vertebrate NP (Sauer 1935), previous studies have largely categorised NP cell shapes into three different groups depending on the apico-basal position of the nucleus: spindle shape (nucleus in the middle), wedge shape (nucleus at the basal surface), and inverted-wedge shape (nucleus near the apical surface)(Smith and Schoenwolf 1987; Smith et al. 1994). However, from my analysis cell nuclei were found to be positioned anywhere along the apico-basal axis. Moreover, the cellular regions that did not contain the nucleus had extremely variable shapes: some were relatively straight, whereas others appeared variably curved. Due to the apparent randomness of the cell shapes, I invented my own way of analysing the dorso-ventral curvature of NP cells (i.e. as seen in transverse section), by determining the area enclosed by a straight line connecting the apico-basal end points of the cell and a curved line that divided the cell area in half. Dividing the area by the straight line length gave a good measure of the extent to which each cell is bent above or below the apico-basal cell axis. Despite the curvature degree value having a unit of

length, comparisons were possible using images with known resolution and scale.

Dorsal cell curvature in unincised embryos was most marked at the closing level, with lower values at the open PNP level. After incision, the cell curvature degree in the dorsal half NP showed a significant 45% reduction at the closing level of the PNP whereas it reduced by only 32% at the open level of the PNP. In contrast, such a drastic change after incision was not observed in the ventral half NP at the closing level. In the ventral half NP at the open level, there was also a significant decrease in the cell curvature degree after incision, along with a change in the direction of curvature (from dorsal-ward to ventral-ward). However, this result seems most likely due to a low sample size compared with the other groups.

The fact that the biggest change after incision was observed in the dorsal half NP at the closing level of the PNP suggests that mechanical stress is particularly concentrated on the DLHP region during its formation, and that this stress contributes importantly to cells adopting dorsally curved structures. In accordance with this idea, FEM modelling proved that the dorsolateral region is going through more stress than the ventromedial region during neural tube closure (Figure 6.2). The same modelling also showed that the DLHP and the ventral NP regions adopt dorsally-curved and ventrally-curved stress patterns, respectively, which suggests possible correlations between the stress profile and cell curvature patterns (Figure 6.2).

3.3.2.2. Nuclear elongation is an endogenous change associated with DLHP formation

At the closing level of the PNP of unincised embryos, nuclear circularity was smaller in the DLHP-present dorsal NP than in the ventral NP whereas at the open level nuclei circularity did not differ between the dorsal and ventral NP. This suggests that cells are more packed in the DLHP region than in the ventral non-bending region. This result is consistent with recent work from our lab based on nuclear counts (McShane et al. unpublished) that cell numbers and cell density are significantly larger in the NF region of elevated NP than that of the flat NP. Moreover, Dil labelling has shown that cells translocate dorsally in the NP during DLHP formation (McShane et al. unpublished). Therefore, it can be concluded that an increase in cell numbers in the dorsal NP during DLHP formation creates internal pressure within the region, which causes cells to become

more packed and nuclei more elongated.

As incision reduced NP bending, it was originally expected that nuclei in the DLHP region at the closing level would become more circular following incision, 'relaxing' and returning to the appearance of nuclei at the open level. However, the opposite result was obtained: nuclei responded to incision by becoming even more elongated, particularly in the dorsolateral region at the closing level. In order to explore this surprising result further, I examined the SE that contacts the dorsal NP, and which is known to be essential for DLHP formation (Ybot-Gonzalez et al. 2002). SE length (in the medio-lateral plane) divided by nuclear number was significantly greater at the closing level before incision than following incision. In unincised embryos, the closing level SE length/nuclear no. also exceeded that at the open level. These results strongly suggest, while the DLHP forms, individual SE cells become stretched, presumably as a response to the NP pull-in force. After incision this force is removed and the cells return to a more normal length, similar to the open PNP level. During the 'shrinkage' of the SE cells after incision, it can be conceived that the space within the dorsolateral NP also shrinks, as the NP is firmly attached by extracellular matrix to the SE (Lawson et al. 2001). This results in increased packing of NP cells, and elongation of their nuclei. Lastly, the shrinkage of the SE cells may also contribute to the reduction in DLHP bending degree post-incision.

The nuclear shape analysis was made on the stack images. As nuclei have 3D shapes, they appear in a consecutive series of planes. Through 3D volume reconstruction from several image processing tools, however, I found it nearly impossible to distinguish individual nuclei from each other as they were intensely spatially dense within the NP, and the boundary of each nucleus tended to overlap others. Nevertheless, by moving between 2D planes, it was more feasible to detect the boundary of each nucleus than by considering their entire 3D volumes. For the nuclear circularity analysis, therefore, the plane where the nucleus had its largest area was chosen. The validity of this method, based on measurement of a single plane for each nucleus, might be questioned. However, by modelling how nuclear circularity changes when a nucleus of constant volume becomes elongated, I found that my own data suggested constancy of nuclear volume in the NP. Moreover, in other cell systems, nuclei with constant volume have been shown to become compressed into different shapes by surrounding pressure (Knight et al. 2002). It seems reasonable, therefore, to expect that the shape of a nucleus in the plane that passes through the central longitudinal axis of the cell is likely to represent the

surrounding packing density. An elongated nucleus suggests a high nuclear population density, and a round nucleus suggests a low density. Lastly, a nucleus was modelled as a capsule-shaped object in my study even though it is conventionally regarded as an ellipsoid (Thibault et al. 2008). From my observation, however, elongated nuclei in the NP indeed mostly adopt capsule shape (Figure 3.7 D), and it was more straightforward to calculate their circularity values when they are treated as capsules than as ellipsoids; more parameters (semi-principal axis values for x, y, and z) and assumptions need to be taken into consideration in an ellipsoidal case.

4. Tissue and cellular morphologies in spinal neurulation defect developing *Zic2*^{Ku/Ku}

4.1. Introduction

Dorsolateral hinge points (DLHPs) are a characteristic feature of the PNP of E9.5 mouse embryos (Shum and Copp 1996). However, DLHPs are absent from *Kumba* mutant mice (Figure 4.1) which have a point mutation in the gene encoding the *Zic2* transcription factor (Ybot-Gonzalez et al. 2007a), resulting in spinal neurulation defects (Elms et al. 2003). During neurulation, *Zic2* is strongly expressed throughout the neuroepithelium of the PNP, but on completion of closure, transcripts become restricted to the roof plate and the region laterally adjacent to the NP (Gaston-Massuet 2004; Gaston-Massuet et al. 2005). DLHP formation and its related signalling pathways have been investigated previously. Both Sonic Hedgehog (Shh), secreted from the notochord (Ybot-Gonzalez et al. 2002), and BMP2 from the surface ectoderm, serve to inhibit DLHP formation, whereas BMP antagonism by proteins including Noggin, secreted from the dorsal NP, is required to induce DLHP formation (Ybot-Gonzalez et al. 2007a). In the same 2007 study, it was demonstrated that *Kumba* (*Zic2*^{Ku/Ku}) embryos have up-regulated BMP signalling and lack BMP antagonists dorsally, probably explaining their failure of DLHP formation. In addition, recent work from our lab involving microarray analysis has identified some molecular pathways associated with failure of DLHP formation in the *Kumba* model. At the stage when spinal neurulation defects first appear in *Zic2*^{Ku/Ku} embryos, Smad-dependent BMP signalling and the expression of *Cav1* (caveolae protein) were found to be up-regulated, while *Nr6a1* (germ cell nuclear factor) and *Grhl3* (spina bifida-related transcription factor) were down-regulated (Raza-Knight et al. unpublished PhD thesis). Despite these molecular insights into the mechanism of neurulation failure in *Kumba* embryos, the associated tissue and cellular morphology have not yet been thoroughly investigated, compared with wild-type.

The spinal neurulation defect is first apparent in *Kumba* mutant embryos at 13-14 somite stage (Raza-Knight et al. unpublished PhD thesis), when DLHPs first appear in normal embryos. My aim was to study this specific somite stage, in order to identify any morphological differences that could be related to failure of neural tube closure in *Zic2*^{Ku/Ku} embryos, and which might shed light on the mechanics of closure more generally. My approach was to measure basal NP width, the effect of neural tube incision on NF re-

opening, and cell curvature/nuclear circularity in $Zic2^{Ku/Ku}$ embryos compared with their wild-type littermates. From previous work in the lab, it had been noticed that the NP appeared smaller in the dorso-ventral dimension in $Zic2^{Ku/Ku}$ embryos than wild-type (see Figure 4.1). I hypothesised that basal NP width (i.e. the distance measured along the entire basal NP surface as viewed in the transverse plane) was likely to be smaller in $Zic2^{Ku/Ku}$ embryos than in wild-type. If confirmed, this would raise the possibility that the mutant would need more dorsal NP pull-in force to bend the NP through the same angle (the same amount of torque) as in wild-type. Hence, at the closing level, the mutant's NP would be expected to experience greater tension than wild-type, and this could be verified by observing the NF re-opening distance after incision, which should be greater than in wild-type. Moreover, cell curvature and nuclear circularity measurements were obtained to gain further information about local stress forces acting upon the NP of the *Kumba* mutant.

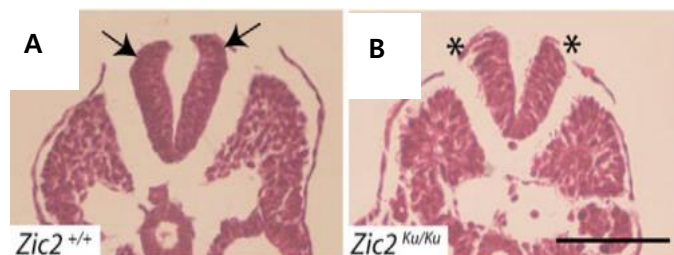


Figure 4.1 Morphology difference between $Zic2^{+/+}$ and $Zic2^{Ku/Ku}$ E9.5 embryos.

DLHPs are clearly present in the wild-type embryo (arrows in A), but are absent from the $Zic2^{Ku/Ku}$ embryo (asterisks in B). Figure adapted from (Ybot-Gonzalez et al. 2007a)

4.2. Results

4.2.1. Tissue morphology differences between *Zic2^{Ku/Ku}* and *Zic2^{+/+}*

In the *Kumba* mutant, PNP closure was found to be arrested at ss13, which resulted in the formation of an enlarged PNP at subsequent developmental stages compared with heterozygous and wild-type littermates (Raza-Knight et al. unpublished PhD thesis). In order to identify the possible mechanical causes of this closure failure in the mutant, structural/geometrical differences on transverse sections of the mutant and heterozygous/wild-type embryos were investigated at the closing level at ss13-16.

A series of consecutive six sections, spaced every 12 μm , was taken at the closing level of the PNP, and basal NP width was measured (yellow dashed lines in Fig 4.2 (A-C)). As the values of the six sections did not differ from each other, for each genotype (Figure 4.2 D), the mean basal width values were compared between genotypes. *Zic2^{Ku/Ku}* embryos proved to have a smaller mean basal NP width than the normally developing wild-type and heterozygous embryos (Figure 4.2 F). In contrast, there was no significant difference in basal NP width between heterozygous and wild-type embryos, although heterozygotes had a slightly lower mean value. A low frequency of spina bifida has been described in heterozygotes (Elms et al. 2003), perhaps explaining this finding.

Next, NP thickness of *Kumba* was analysed as the thickness could be another major component that affects bending of the NP. Anecdotal observations had previously suggested a thicker NP in *Zic2^{Ku/Ku}* embryos. However, it was difficult to take one specific site of the NP for this thickness comparison, as NP thickness varied dorso-ventrally in all genotypes. Therefore, I decided to measure mean NP thickness on the transverse section by dividing the area of the NP, which can be drawn and measured from ImageJ, by the basal NP width (NP area/basal width = mean NP thickness). Mean NP thickness values did not differ amongst a series of six sections from each genotype (Figure 4.2 E). Hence, means of the six section values were compared between different genotypes. This showed that mean NP thickness in *Zic2^{Ku/Ku}* embryos was significantly smaller than that of wild-type embryos, around the closing level, whereas there was no difference between heterozygotes and either of the other genotypes (Figure 4.2 G).

It was noticeable that the reduction in mean basal NP width in mutant embryos (~ 35% less than wild-type) was much greater than the reduction in mean NP thickness (~ 10% less than wild-type). It was concluded, therefore, that the basal NP width difference may be more influential than mean NP thickness difference in affecting neural

tube closure in $Zic2^{Ku/Ku}$ embryos. The effect of the geometric morphology differences on neural tube closure is discussed further in the FEM Modelling section (see Chapter 6).

Figure 4.2 *Kumba* embryo's morphology at the onset of spinal neurulation defect.

(A-C) Transverse sections of *Zic2*^{Ku} embryos at the stage of onset of the spinal neurulation defect. Sections are taken from a level 12 μm caudal to the closure point. Wild-type (ss15)(A) and heterozygous (ss14)(B) have longer basal NP widths than mutant (ss15)(C). Yellow dashed line represents basal NP width. Scale bar represents 50 μm .

(D-E) Basal NP width (D) and NP area/basal NP width (i.e. mean NP thickness)(E) from the first six sections caudal to the closure point. There is no significant difference between different rostro-caudal PNP levels for each genotype, for either measurement. For basal NP width, WT: $p = 0.974$, one-way ANOVA, Het: $p = 0.992$, Kruskal-Wallis one-way ANOVA on ranks, Mut: $p = 0.358$, one-way ANOVA. For NP thickness, WT: $p = 0.684$, one-way ANOVA, Het: $p = 0.429$, Kruskal-Wallis one-way ANOVA on Ranks, Mut: $p = 0.851$, one-way ANOVA. N: the number of embryos analysed.

(F-G) Mean basal NP width (F) and mean NP thickness (G) of the first six sections from the closure point. Mean basal NP width is significantly lower in mutant than in wild-type or heterozygous embryos ($p < 0.001$, one-way ANOVA with Holm-Sidak multiple comparison procedures, significance level $p = 0.05$). Mean NP thickness is also significantly lower in mutant than wild-type, although the heterozygote value does not differ from either of the other genotypes ($p = 0.020$, one-way ANOVA with Holm-Sidak multiple comparison procedures, significance level $p = 0.05$). *: $p < 0.05$. n: the number of embryos analysed.

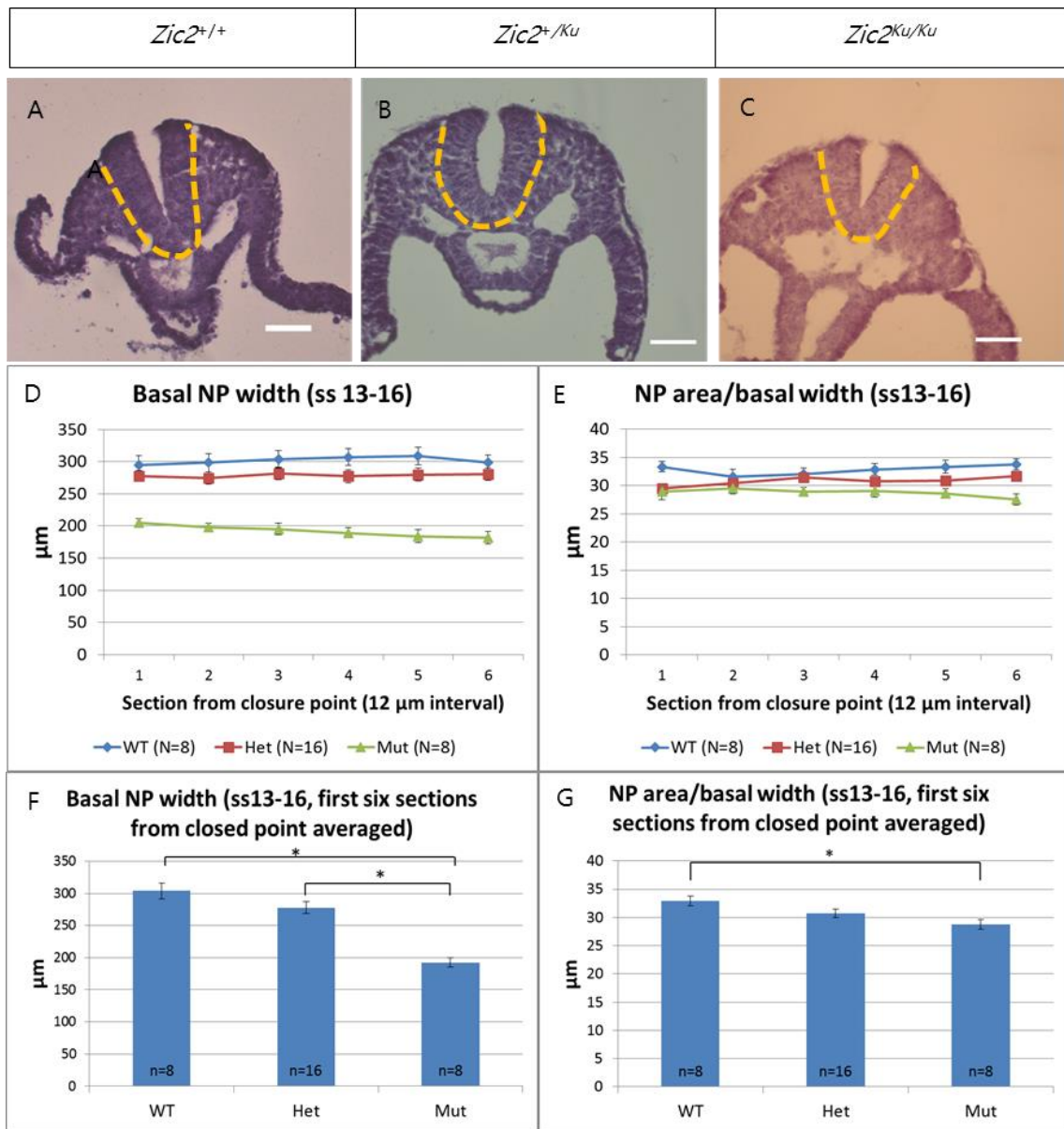


Figure 4.2 Morphology of *Kumba* embryos at the onset of spinal neurulation defect.

4.2.2. Tissue morphology change after neural tube incision in *Zic2*^{Ku/Ku} embryos

In Chapter 3, the mechanical effects of NT incision on the NF re-opening were studied in wild-type embryos. *Zic2*^{Ku/Ku} embryos start developing their spinal closure phenotype from around ss13, and a possible cause for this could be a stiffer NP in mutant than wild-type (see Chapter 5 for an experimental test of NP stiffness). This would require increased external force to achieve closure, leaving the mutant NP under greater tension than wild-type at closing level of the PNP. Therefore, an incision experiment using *Kumba* embryos was designed in order to test this hypothesis, by comparing the NF re-opening distance of mutant and wild-type embryos following NT incision at the same somite stage. The prediction was that, if there is more mechanical tension in the closing neural tube of *Kumba* mutant embryos, they will exhibit a greater extent of NF re-opening after incision.

In this experiment, embryos were divided into two groups according to somite stage: ss13-16 (E9.0), and ss17-23 (E9.5). NF re-opening after incision was recorded while the embryos were still alive (approximately 1 minute after incision), before transferring them to Bouin's solution. It was found that NF re-opening in the mutant was significantly greater than in heterozygous and wild-type littermates at both somite stages (Figure 4.3 A-E). Moreover, embryos at the more advanced stage (ss17-22) showed significantly greater NF re-opening than those of the earlier stage (ss13-16), irrespective of genotype. Incision length was kept as constant as possible and was not significantly different between the two somite stage groups, nor between genotypes (Figure 4.3 F). Hence, any possible effect of incision length variation on NF re-opening distance could be excluded.

These results suggest that the mutant's recently closed region is under greater tension than in normally developing embryos. Two possible causes were considered: first, that the NP of mutant embryos may be 'stiffer' (i.e. having higher Young's modulus values). Indeed, the greater NF re-opening in mutant embryos coincided with the result of AFM measurements (see Chapter 5), which revealed that both the dorsal and ventral NPs of *Zic2*^{Ku/Ku} embryos (ss16-17) have higher stiffness values than wild-type. This result is discussed further in Chapter 5.

The second possibility to be considered was that the mutant embryo has a more curved trunk that builds up tension on the neural tube roof. Previous work had demonstrated that convex curvature slows closure in mouse (Brook et al. 1991) and chick

(van Straaten et al. 1993) embryos. To investigate this possibility, curvature of the trunk was compared between somite stage groups and between genotypes (Figure 4.4 A-D). However, no significant differences in body axis curvature were detected in either comparison (Figure 4.4 E) suggesting that this is an unlikely explanation for the enhanced NF re-opening observed in *Zic2*^{Ku/Ku} or older somite stage embryos.

Figure 4.3 NF re-opening at previously closing level of *Kumba* embryos.

(A-B) NF re-opening of wild-type embryo (ss13) after incision. The length of red arrow between Dil marks before incision (A) and after incision (B) is nearly the same.

(C-D) NF re-opening of *Zic2*^{Ku/Ku} embryo (ss16) after incision. The length of the blue arrow between Dil marks is much longer after incision (D) than before incision (C).

(E) Graph of NF re-opening for ss13-16 and ss17-23 *Kumba* embryos. According to two-way ANOVA analysis ($p = 0.004$ for somite groups; $p = 0.001$ for genotypes), followed by Holm-Sidak multiple comparison procedure (significance level $p = 0.05$), NF re-opening in the ss17-23 group was significantly greater than in the ss13-16 group. Moreover, NF re-opening in *Zic2*^{Ku/Ku} (Mut) embryos was significantly greater than in wild-type or heterozygous littermates. The numbers of wild-type, heterozygous, and mutant embryos analysed were 5, 1, and 4, for ss13-16, and 2, 2, and 3, for ss17-23, respectively.

(F) Graph showing incision lengths in *Kumba* embryos. There were no significant differences in mean incision length between the two somite stage groups, nor between genotypes ($p = 0.112$ for somite stage groups; $p = 0.301$ for genotypes; two-way ANOVA analysis). This suggests that the differences observed in NF re-opening distance are unlikely to be related to incision length differences. Error bars represent standard errors. n: the number of embryos analysed.

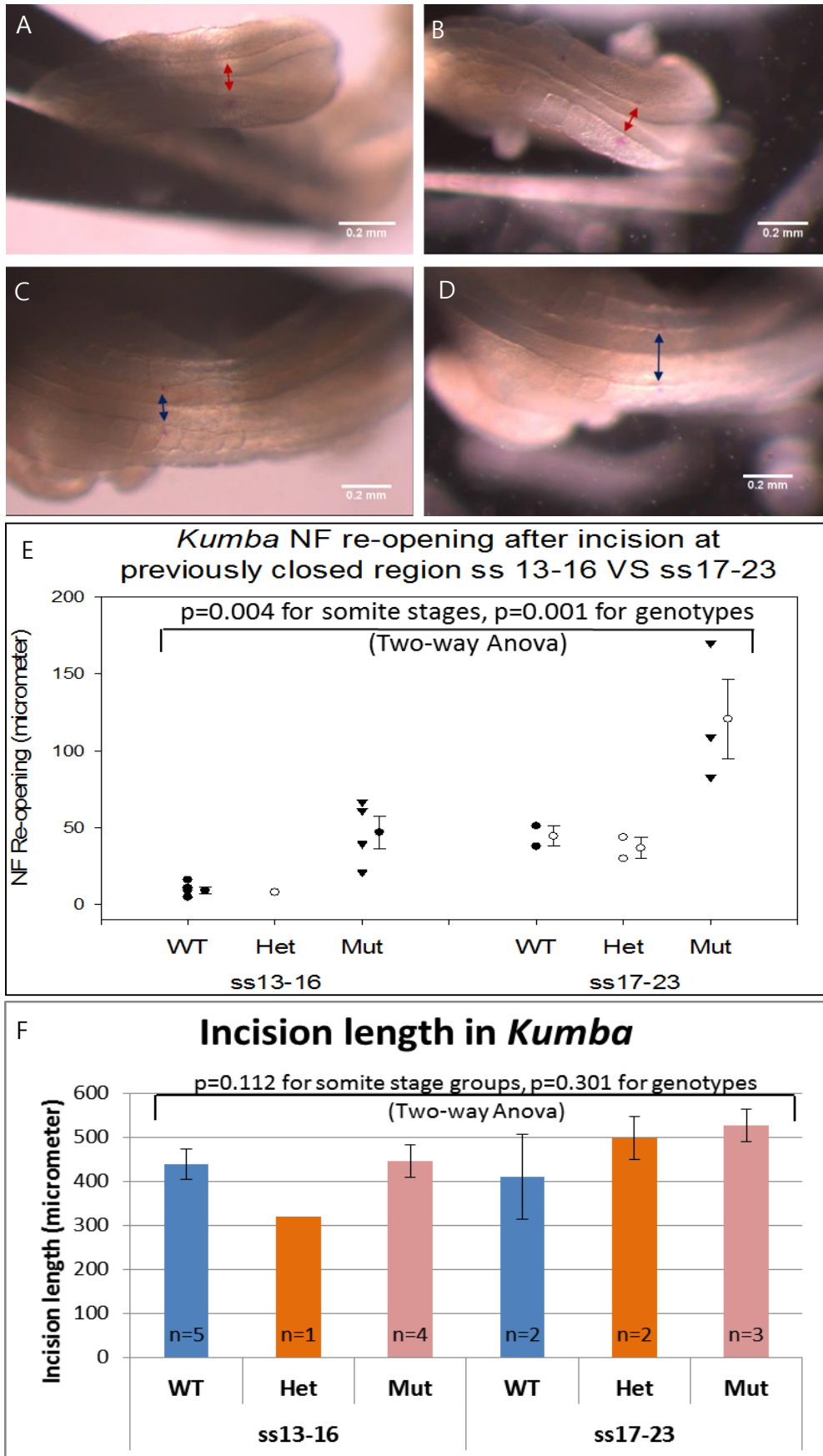


Figure 4.3 NF re-opening at previously closing level of *Kumba* embryos.

Figure 4.4 Curvature of the trunk of *Kumba* embryos.

(A-D) Wild-type ss14 (A) and ss19 (B), and *Zic2^{Ku/Ku}* ss16 (C) and ss22 (D) embryos illustrating the method of curvature measurement. A yellow curved line of 728 μm was drawn rostrally from the closure point (Dil-labelled), along the trunk curvature. Curvature was estimated by dividing the area enclosed within the yellow lines by the straight line length. Red arrows indicate Dil labels. Scale bar represents 0.2 mm.

(E) Curvature measurements of the trunk of ss13-16 and ss17-23 embryos of the three *Kumba* genotypes. No statistical differences were found between somite stage groups nor between genotypes ($p = 0.635$ for genotypes; $p = 0.104$ for somite stage groups; two-way ANOVA using somite stage ranges and genotypes as factors). The numbers of wild-type, heterozygous, and mutant embryos analysed were 5, 1, and 2, for ss13-16, and 2, 2, and 3, for ss17-23, respectively.

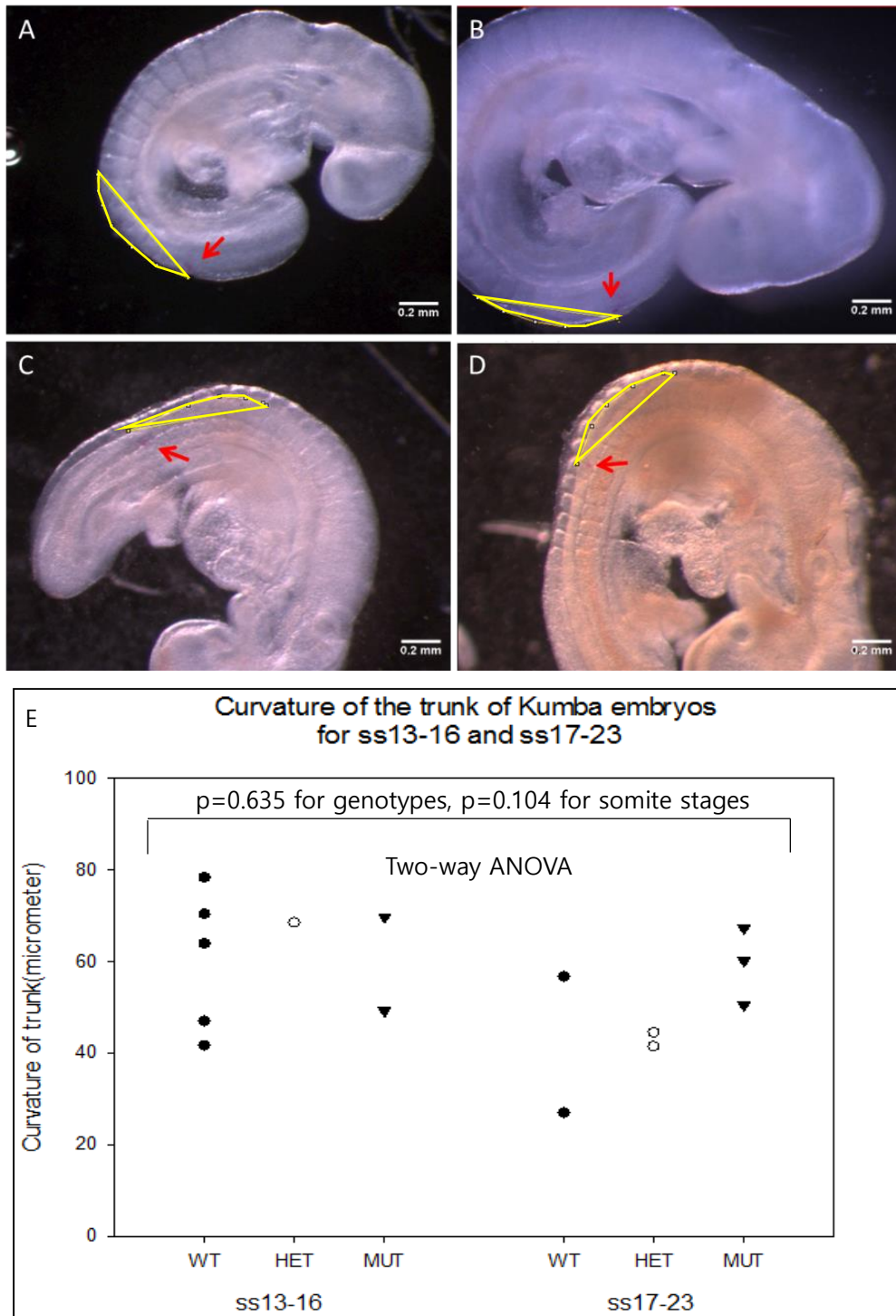


Figure 4.4 Curvature of the trunk of *Kumba* embryos.

In summary, following incision, mutant and older stage embryos (ss17-23) both exhibited greater NF re-opening than normally developing and younger stage embryos (ss13-16). In conjunction with the findings from AFM measurements of NP elasticity, the larger re-opening observed in *Zic2*^{Ku/Ku} embryos seems likely to be linked to the NP with large stiffness value in the mutant. A similar conclusion may also apply to the somite stage difference in re-opening (see Chapter 5). While an effect of trunk curvature should be considered, there was no difference in curvature detected between different somite stage groups nor between genotypes.

4.2.3. Cell shape differences between *Zic2*^{Ku/Ku} and wild-type embryos

4.2.3.1. Cell curvature differences

For the cell curvature analysis in Chapter 3, mice of genotype *Grhl3*^{cre/+};*ROSA*^{YFP/+} were used as these showed a mosaic pattern of YFP-expressing cells in the NP, which facilitated an individual cell shape analysis. However, for genotyping reasons, it proved to be difficult to generate this same genotype on the *Kumba* background. Instead, a cytoplasmic GFP plasmid vector was injected into the amniotic cavity of E8.5 *Kumba* embryos and electroporated, with targeting of the caudal region. Using a low concentration of plasmid (3000 ng/ μ l), a mosaic pattern of GFP expression was achieved by this method. After overnight culture, GFP expression was observed in 76% of electroporated embryos (103 out of 135 embryos that were cultured), within which nearly 50% (48 out of 103 GFP-positive embryos) showed strong expression particularly in the caudal region. Due to the growth variance caused by the culture environment and the low Mendelian ratio of appearance of mutant embryos (25%), embryos of a somewhat wide somite range (e.g. ss13-19) were collected for analysis.

For wild-type and heterozygous embryos, the first 3 sections from the closure point were taken for the analysis as DLHPs were most prominent in that region. For mutant embryos, however, PNP length greatly varied depending on somite stage, and the NP did not always express GFP uniformly throughout the PNP. In order to collect as many cells as possible among the limited sample of mutant embryos that was available, I decided to include a larger range of sections (200-600 μ m from the caudal end) for the analysis. The mean of this range (400 μ m) approximately matches the mean closing level for wild-type embryos (425 \pm 43 (SEM) μ m from the caudal end), but at this level, the

mutant NP was still open (see the diagram in Figure 4.6). Sections at the closing level of the mutant embryos were not considered due to the low number of samples.

The comparison of cell curvature between genotypes showed significantly lower mean values for *Zic2*^{Ku/Ku} embryos, indicating that cells in the mutant NP were less curved dorsoventrally than in either wild-type or heterozygous embryos. On the other hand, there was no significant difference in cell curvature between dorsal and ventral NP halves (Figure 4.5 A-D). As expected, the dorsolateral NP bending degree was significantly lower in the mutant than in the other genotypes. Wild-type and heterozygous embryos did not differ from each other (Figure 4.5 E). Hence, in *Kumba* embryos, as in non-mutants (Chapter 3), cell curvature degree is correlated with dorsolateral NP bending degree.

The proportions of spindle, wedge, and inverted-wedge shaped cells were measured in the NP using a conventional method of NP cell shape categorisation (Smith and Schoenwolf 1987). No significant differences were found in cell shape proportions between genotypes for either dorsal or ventral half NP (Figure 4.5 F,G).

Figure 4.5 *Kumba* NP cell curvature.

(A-C) GFP-expressing cells within the NP of wild-type *ss16* (A), heterozygous *ss19* (B), and mutant *ss16* (C) embryos. Many cells in the wild-type and heterozygous NPs show dorsal curvature (red arrows in A, B), whereas cells in mutant NP appear straight (yellow arrow in C) or even ventrally curved (white arrow in C). Scale bars represent 20 μm .

(D) Comparison of mean cell curvature degree between genotypes and dorso-ventral NP levels (2 way Anova using genotypes and dorsal/ventral NP halves as factors). Sections were analysed at closing level for wild-type and heterozygotes, and at open level for the mutant. There is no significant difference between dorso-ventral levels ($p = 0.590$) whereas genotypes differ significantly ($p = 0.003$), with lower mean curvature in mutant than in wild-type or heterozygous embryos (Holm-Sidak multiple comparison procedure; $p < 0.05$). n: number of cells scored; N: number of embryos analysed. Error bars represent standard errors.

(E) Mutant embryos (at open level) show a significantly lower dorsolateral NP bending degree than either wild-type or heterozygous embryos (at closing level), which do not differ from each other ($p < 0.001$, one-way ANOVA with Holm-Sidak multiple comparison procedures, $p < 0.05$). *: $p < 0.05$. n: number of NP sections scored; N: number of embryos analysed. Error bars represent standard errors.

(F-G) Proportions of spindle, wedge, and inverted-wedge shaped cells in dorsal (F) and ventral (G) halves of the NP. No significant differences were detected between genotypes for either dorsal NP ($p = 0.255$, power of test = 0.410, alpha = 0.050) or ventral NP ($p = 0.158$, power of test = 0.503, alpha = 0.050; Chi-square tests). The number of cells for the dorsal half (WT: 31, Het: 20, Mut: 41) and for the ventral half (WT: 37, Het: 18, Mut: 22).

(H-I) Images of a *ss20* heterozygous embryo that was electroporated/overnight-cultured in brightfield (H) and in GFP-fluorescent filter (I). Orange dashed lines represent the boundary of the PNP. Scale bars represent 0.2 mm.

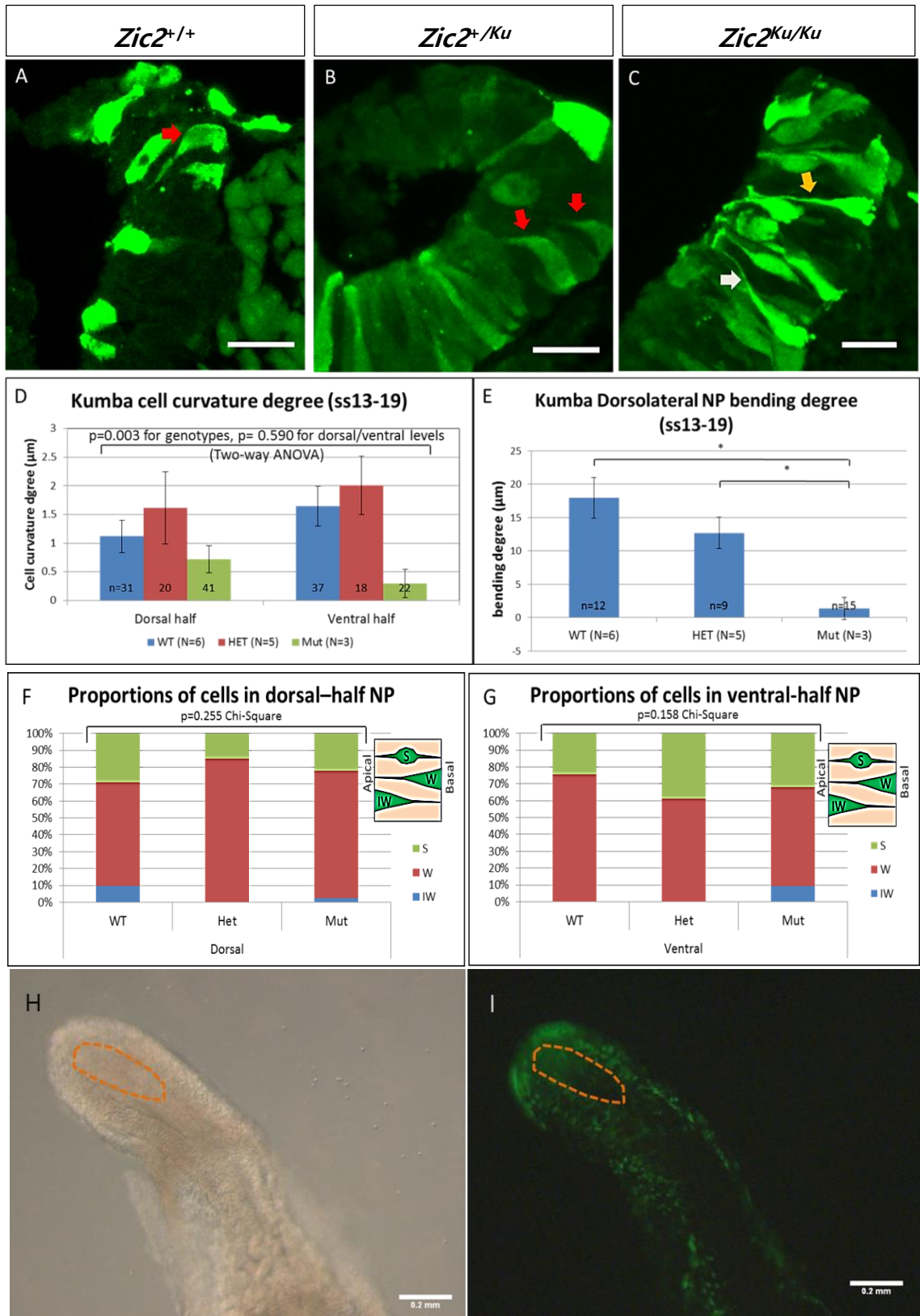


Figure 4.5 *Kumba* NP cell curvature.

4.2.3.2. Nuclear shape differences

PNP closure in the *Kumba* mutant embryo is arrested at around 13 somite stage (Raza-Knight et al. unpublished PhD thesis) while the rest of the embryo continues growing. This results in an elongated PNP, as illustrated by Figure 4.6 G, which shows PNP lengths of the three different *Kumba* genotypes at ss9-23. Particularly at ss18-23, mean PNP length in *Zic2^{Ku/Ku}* embryos (1520 ± 70 (SEM) μm) is more than double the values seen in wild-type (608 ± 28 μm) and heterozygous (629 ± 37 μm) littermates.

Chapter 3 described reduced nuclear circularity (more elongated/packed nuclei) in normally developing embryos within the dorsal NP at the closing level where DLHPs are present. Since DLHPs are absent from the mutant NP throughout the PNP (Ybot-Gonzalez et al. 2007a), I investigated whether nuclear circularity might show comparable differences between the NP of the mutant embryos and that of wild-type/heterozygous embryos where DLHPs occur normally.

While the *Kumba* embryos for cell curvature analysis had to be cultured after GFP-electroporation, for the nuclear shape analysis, fresh embryos were fixed straightaway after the dissection. For wild-type and heterozygous embryos, the first two 25 μm sections caudal to the closing point were taken for analysis (Figure 4.6 B,C). For mutant embryos, the equivalent rostro-caudal level to the closing level in wild-type and heterozygous embryos at ss18-23 was 575-625 μm from the caudal end; at this level, the mutant NP was widely open (Figure 4.6 D). Analysis was performed at this level, but also at the closing level in mutant embryos, even though this was considerably more rostral than the closing level in wild-type and heterozygous embryos (Figure 4.6 E).

Nuclei in the mutant NP were more circular than those in wild-type NP at the identical level (closing level for wild-type), and this difference was more prominent in the dorsal NP than in the ventral NP (Figure 4.6 A). Moreover, at the same level, nuclei were also more circular in heterozygous embryos than in wild-type, but less circular than in mutants. Considering that DLHP bending degree did not differ between wild-type and heterozygous embryos (Figure 4.6 F), it would seem that this nuclear circularity difference between wild-type and heterozygotes did not arise from a difference in NP morphology. Haploinsufficiency for *Zic2* function may have other bio-molecular effects on the neural plate, consistent with previous findings that *Zic2^{Ku}* heterozygotes exhibit a low penetrance of spinal defects at birth (Elms et al. 2003). It was also observed that,

particularly in the dorsal NP, nuclei at the closing level were more elongated than at the open level in *Zic2^{Ku/Ku}* embryos, but still rounder than those at the closing level of wild-type embryos. Considering that there is no DLHP formed at the closing level of mutant embryos (Figure 4.6 E), these results suggest that nuclei become more packed/elongated when the NP is closing and this effect becomes more prominent when the DLHP starts to form.

Figure 4.6. *Kumba* nuclear circularity and DLHP bending degree.

(A) Nuclear circularity in the dorsal/ventral NP of *Kumba* embryos. In both the dorsal and ventral NP halves, mutant mean nuclear circularity is significantly greater than wild-type and heterozygous values. Moreover, heterozygotes exhibit significantly greater nuclear circularity than wild-type ($p < 0.001$ for genotype comparison in both dorsal and ventral NP, Kruskal-Wallis one-way ANOVA on ranks with Dunn's Multiple Comparison Procedures, $p < 0.05$). n: the number of nuclei scored; N: number of embryos analysed. Error bars represent standard errors.

(B-E) DAPI-stained transverse sections of *Kumba* embryos (E9.5) at different PNP levels: (B) Wild-type (ss18) at the closing level; (C) Heterozygous (ss22) at the closing level; (D) Mutant (ss19) at the open level; (E) Mutant (ss19) at the closing level. The diagram in the centre explains how two measurement levels were used for mutant embryos: at the closing region which is considerably more rostral than in wild-type or heterozygous embryos (E; Mut-closing) and at the same axial level as measured in wild-type and heterozygous embryos, even though this is not closing in mutants (D; Mut-open). White arrowheads indicate the DLHPs in wild-type and heterozygous embryos, whereas these are absent from mutants at both closing and open levels. Scale bars represent 30 μ m.

(F) *Kumba* dorsolateral NP bending degree at the closing level for wild-type and heterozygous and at the open level for mutant (575-625 μ m from the caudal end, analogous to the closing level of wild-type and heterozygous). The value for mutant is significantly lower than wild-type and heterozygous values ($p < 0.001$, one-way ANOVA with Holm-Sidak multiple comparison procedures; $p < 0.05$). Minus value represents outward curvature. n: the number of NP sections scored; N: number of embryos analysed. *: $p < 0.05$. Error bars represent standard errors.

(G) PNP length plotted against somite stage for the *Kumba* mutant and wild-type/heterozygous littermates. In the graph, embryos younger than ss18 were fixed in Bouin's solution, whereas embryos more advanced than ss18 were fixed in PFA. Presumably due to the complication of the fixation methods, which might have resulted in different shrinkage rate in the two groups of embryos, PNP length of wild-type and heterozygotes is not showing a typical declining trend that can be seen in normally developing embryos. However, PNP length of the mutant is showing a clear increasing trend.

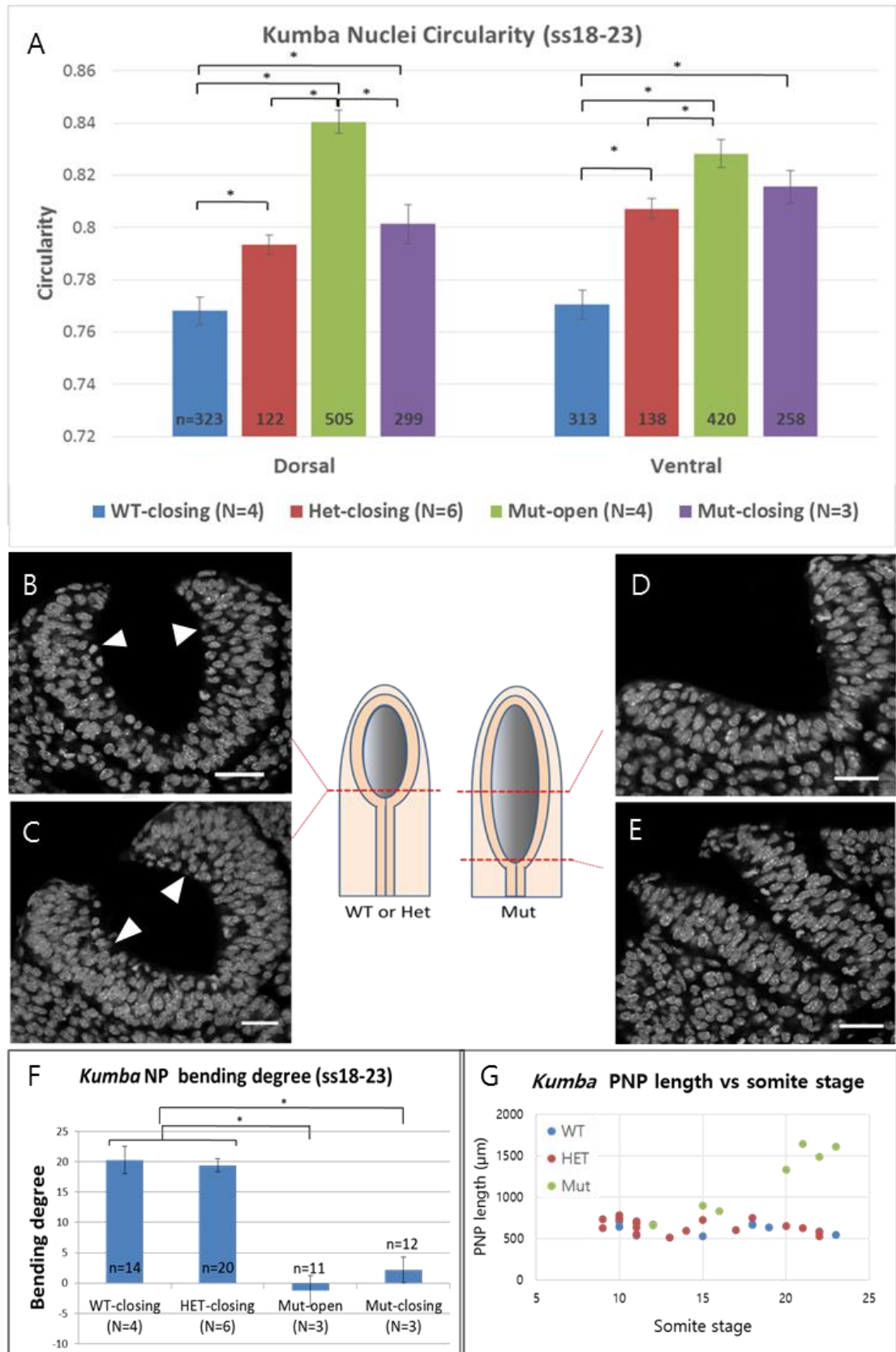


Figure 4.6 *Kumba* nuclear circularity and dorsolateral bending degree.

4.3. Discussion

4.3.1. Tissue morphology differences between *Zic2^{Ku/Ku}* and wild-type

It was previously found that DLHP formation is closely related to BMP signalling. BMP2 inhibits DLHP formation whilst its antagonism by noggin induces DLHP formation (Ybot-Gonzalez et al. 2007a). Further to this study, recent work from our lab showed that in the *Kumba* mutant (*Zic2^{Ku/Ku}*) PNP, at the onset of the spinal neurulation defect, Smad-dependent BMP signalling was up-regulated. Moreover, confirming previous microarray results, the expression of *Cav1* was found to be up-regulated, while *Nr6a1* and *Grhl3* were down-regulated, compared with wild-type (Raza-Knight et al. unpublished PhD thesis). It was reported that null mutation of *Nr6a1*, a BMP repressor (Lan et al. 2003), causes open neural tube, failure to turn, a posterior truncation, and a halt in somitogenesis after 13 somites (Chung et al. 2001). The function of *Grhl3* has been well characterised in the curly tail mouse, in which reduced expression of *Grhl3* in the spinal region results in a proliferation defect in the hindgut endoderm, followed by spina bifida (Gustavsson et al. 2007). The role of *Cav1* in neurulation is not well known due to the lack of overexpression studies of *Cav1*. Nevertheless, it was found that *Cav1* knockout mice develop vascular abnormalities, but without NTDs (Razani et al. 2001). However, the physical morphology differences between *Kumba* mutant, heterozygote and wild-type had not been investigated in detail, and so the aim of this thesis was to examine basal NP width, mean thickness of the NP, nuclear circularity and cell curvature in *Kumba* mutant embryos.

Both basal NP width and NP thickness were reduced in *Zic2^{Ku/Ku}* compared with heterozygous and wild-type embryos at the onset of spinal defects (ss13-16). While the NP width showed a marked reduction of around 35% in mutants, the NP thickness was reduced by only 10%. It has been suggested that the retarded growth in *Zic2^{Ku/Ku}* could be attributable to a decrease in Shh-regulated cell proliferation (Raza-Knight et al. unpublished PhD thesis). Both in the forebrain (Warr et al. 2008) and spinal region (Raza-Knight et al. unpublished PhD thesis) of *Zic2^{Ku/Ku}* embryos, Shh signaling was found to be down-regulated together with abnormal development of the notochord. Another study revealed that inhibition of Shh signaling causes a reduction in proliferation and survival of progenitor cells in the neuroepithelium (Cayuso et al. 2006). Therefore, it seems that reduced supply of progenitor cells might cause the immature NP development in *Zic2^{Ku/Ku}*. Nevertheless, cells within the mutant NP perhaps go through a relatively normal cell cycle,

by interkinetic nuclear migration, as there was no alteration in a proportion of wedge, spindle, and inverted-wedge shaped cells between the mutant NP and the wild-type NP.

The effect of the NP width on neural tube closure is further investigated in Chapter 5, where calculation of the dorsal closing force is performed using a Finite Element Method (FEM) simulation.

4.3.2. Tissue morphology change after incision on *Zic2^{Ku/Ku}* embryos

NF re-opening was measured, after incision of the most recently closed neural tube roof, in order to determine whether there may be mechanical differences between the NP of *Zic2^{Ku/Ku}* and wild-type, as the NFs are coming into apposition. NF re-opening in mutant embryos was found to be markedly greater than in wild-type or heterozygous embryos of a similar somite stage. Considering incision length was not statistically different between genotypes, and between the two somite stage groups that were studied (ss13-16 and ss17-23), this result strongly suggests that the mutant NP is under a greater amount of tension at the closing level, compared with normally developing embryos. In order to find the underlying reasons for this result, both NP stiffness and curvature of the embryonic trunk were investigated. No differences were observed in the degree of curvature of the trunk in mutants compared with the other genotypes. NP stiffness as measured using AFM was found to be enhanced in mutant embryos compared with wild-type (see Chapter 5). A stiffer NP (large elastic modulus value) is expected to be under greater stress when it is bent, and so will release more energy following incision, leading to greater NF re-opening. This idea is consistent with a previous study in anterior intestinal portal tissue of the chick heart tube, whose opening angle after incision was compared in the presence or absence of blebbistatin (a myosin-II inhibitor). Stiffness measurements were also made of each tissue (Varner and Taber 2012). Blebbistatin-treated tissue showed a significant reduction in opening angle, with lower stiffness values. This result strongly suggests that the opening degree of a tissue upon incision could be an indicator of the stiffness of the tissue.

Previous studies showed that PNP closure begins to show a delay in the *Kumba* mutant around 13 somite stage (Raza-Knight et al. unpublished PhD thesis). In my study, the difficulty of predicting exact stages of embryos in mouse litters led to embryos being collected largely in two somite stage groups: ss13-16 and ss17-23. However, even at the 13-16 somite stage, I found that mutant embryos had already begun to differ from wild-

type, in terms of a slightly longer PNP. Therefore, there is a possibility that the enhanced degree of NF re-opening in mutants might have been secondary to pre-existing enlargement of the PNP. In Chapter 6, FEM modelling of neural tube closure showed that, when a tube is being closed, the required dorsal closing force peaks at the closure-initiating site (large PNP) and gradually decreases towards the closure-completing site (small PNP). This result suggests that there is higher tension applied to the closing point when the PNP is larger, which leads to wider NF-reopening in mutants once incision is made.

NF re-opening after incision was found to be significantly greater in older (ss17-23) than in younger (ss13-16) stage embryos. This occurred irrespective of genotype, and amounted to an approximately 4-fold greater re-opening of wild-type NFs after incision at the later stage (see Figure 4.3 E). It was initially hypothesised that the presence of DLHPs was associated with the larger NF re-opening observed in older stage embryos: DLHPs were present in older embryos but could not be discerned at the younger stage. However, in the *Kumba* mutant there were no DLHPs at either somite stage, and yet the same trend of increased re-opening at ss17-23 was observed. Body axis curvature did not differ between the two somite stages, effectively ruling out this potential factor in NF re-opening. Other factors may be implicated in determining the extent of NF re-opening. For example, NP stiffness may increase and indeed AFM measurements revealed that NP stiffness was significantly larger in older embryos than in younger ones (see Chapter 5). This result is consistent with previous studies in chick (Xu et al. 2010) and frog (Zhou et al. 2009) embryos, which have shown that stiffness of tissue increases as embryos develop.

4.3.3. Cell shape differences between *Zic2*^{Ku/Ku} and wild-type

4.3.3.1. Cell curvature difference

A cytoplasmic GFP plasmid vector was administered into the NP by electroporation and, after overnight culture, cell shapes were compared between *Kumba* mutant and wild-type/heterozygous embryos. Cell curvature analysis revealed that the NP of mutant embryos which lacked DLHPs had relatively straight cells, compared with the NPs of wild-type and heterozygous embryos that had more dorsally curved cells, in association with prominent DLHPs. This finding is consistent with the earlier result (see

Chapter 3) from *Grhl3^{cre/+};ROSA^{YFP/+}* embryos, which demonstrated that cells were relatively straight in the open flat NP compared to the closing NP where DLHPs had formed.

This analysis suggests that cell curvature is associated with NP bending, but does not prove that the NP bending actually causes the cells to be dorsally curved. However, the earlier incision experiment on *Grhl3^{cre/+};ROSA^{YFP/+}* embryos revealed that dorsally curved cells at the closing level became more straight after incision, with the relaxation of the bent NP. This suggests that cell shape is elastic and that dorsal curvature is caused by the NP bending. Therefore, it can be concluded that DLHP formation exerts bending stress on the NP, and that NP cells change their curvature according to the bending stress they experience.

A similar cell behaviour was documented in a study by Amir et al. (2014), which showed that a bacterial cell could be bent by hydrodynamic flow, and then return to its initial straight state immediately after the removal of the bending force, hence demonstrating the elasticity of a very different cell type.

The proportions of the main three cell shapes (i.e. wedge-, spindle-, and inverted-wedge-shape) were compared between different genotypes for the dorsal and ventral halves of the NP. It has been shown that cells become wedge-shaped cells during bending of the neuroepithelium, particularly in the midline (Schoenwolf and Franks 1984; Smith and Schoenwolf 1987; Smith et al. 1994). During neurulation in chick embryos, it was shown that more than 70% of the cells in the median hinge point and 55% in the dorsolateral hinge point are wedge-shaped, whilst only 35% in the non-bending region are wedge-shaped (Schoenwolf and Franks 1984). Recent work from our lab (McShane et al. unpublished) compared apico-basal nuclear locations, as an indicator of NP cell shape, at different stages of spinal neurulation, and in different NP regions. When comparing flat NP (DLHP absent) with elevated NP (DLHP present) in the dorsolateral region of E9.5 embryos, the proportion of basal nuclei (i.e. wedge-shaped cells) was not found to be statistically different. This result is consistent with my finding that the proportion of wedge-shaped cells in the dorsal NP did not differ between mutant (DLHP absent) and normally developing (DLHP present) embryos. The evidence suggests, therefore, that DLHP formation is not marked by a local increase in wedge-shaped cells, and that the lack of DLHPs in *Kumba* mutant embryos is not related to a failure to generate wedge-shaped cells in the NP.

4.3.3.2. Nuclear shape difference

In Chapter 3, mathematical modelling revealed that nuclear circularity and Feret diameter have an inverse relationship when a nucleus is being elongated with conservation of its volume. After confirming that actual data followed the same trend as observed in the modelling, it was concluded that the nuclear volume of NP cells remains relatively constant while the cells are undergoing elongation. This implies that nuclear circularity values actually reflect the elongation state of nuclei. It was also shown that nuclei became more elongated when the space they occupy becomes decreased following NT incision, suggesting that nuclear elongation can be used as an indicator of local tissue pressure.

With these findings in mind, I compared nuclear circularity in *Kumba* embryos with the result that NP cells of mutant embryos were found to have more circular nuclei than those of wild-type and heterozygous embryos at the comparable axial level (i.e. closing level for wild-type and heterozygous, and 600 μm from the caudal end for mutants). A similar result was obtained when the mutant NP was studied at the closing level (i.e. considerably more rostral than in normally developing embryos). Considering that the NP bending degree of mutant embryos was markedly less than that of wild-type and heterozygotes, it can be concluded that nuclei become more elongated in NP that contains DLHPs than in NP that lacks DLHPs. This result is consistent with the finding that *Grhl3^{cre/+};ROSA^{YFP/+}* embryos exhibit greater nuclear elongation at the closing level where DLHP are present than at the open level where they are absent (see Chapter 3).

In recent work from our lab (McShane et al. unpublished), calculated mean cell diameter (NP width divided by nuclear number) in transverse sections was found to decrease significantly during elevation of the DLHP-containing NF, a finding that suggests cells become more closely packed in the dorsolateral NP during DLHP formation. This is consistent with my finding that nuclei become elongated in association with DLHP formation.

However, it is not clear how the cell-packing contributes to bending of the NP in the normally developing embryos. The observation that nuclei were more elongated in the NP of wild-type than mutant strongly suggests that there is an increased level of internal pressure in the wild-type NP. Therefore, it can be inferred that the pressure in the NP contributes to DLHP formation, perhaps by mechanical distortion of the NP structure. In support of this idea, a study of avian gut tube morphogenesis showed that

proliferation in the endoderm is more active in the folding region than the median region which is being flanked bilaterally by the folding part (Miller et al. 1999). In the same study, it was also found that there is no apoptosis involved during the endoderm folding. This suggests that newly populated cells can all contribute to building up the pressure within the germ layer, which might be a key mechanical cause of the folding. In conjunction with the 1999 study, recent work from our lab (Raza-Knight et al. unpublished PhD thesis) revealed that, when using Caspase 3 as a cell apoptosis marker, there was no difference detected in the apoptotic activity between wild-type and the *Kumba* mutant in the neuroepithelium for 18-20 somite stage. In the same study, however, proliferation rate was not compared for the same somite stage range, but for 14-15 somite stage; surprisingly, the mutant NP showed a significantly increased proliferation rate compared with wild-type, in the ventral region at this stage. Therefore, investigation of cell proliferation activity in the later stage of *Kumba* embryos would be an important future experiment.

5. *Kumba* NP stiffness measurement

5.1. Introduction

5.1.1. Atomic Force Microscopy working principles

Atomic force microscopy (AFM) is a high resolution type of scanning probe microscopy that can measure the stiffness (elasticity) or topography of a sample. A highly sensitive silicon cantilever, controlled by a piezo-electric ceramic, is brought into contact with a sample and the deflection of the cantilever is sensed by the change in the path of laser light that is reflected from the back of the cantilever towards a photodiode (Figure 5.1). When the cantilever is pressed onto a sample, the deflection is converted into the force applied to the sample, and the vertical position of the cantilever is recorded. As an output of the measurement, a force-distance curve (Figure 5.1 B) is obtained for each measurement point, and the Young's modulus (i.e. stiffness) of the sample can be calculated using Hertzian contact mechanics which takes into account the geometry of the tip-sample contact. In my work, the AFM probe contact surface was made spherical, by attaching a glass bead to the probe tip, in order to achieve a generalised indentation of the NP surface, rather than localised indentation of just one or a few NP cells.

5.1.2. Factors affecting stiffness

The cytoskeleton has been long known to be involved in setting the mechanical properties of tissue and cells. In a frog (*Xenopus*) embryo study, dorsal axial and paraxial tissues were surgically isolated (dorsal isolate) and treated with latrunculin B that depolymerises F-actin, and Y27632, a Rho-kinase inhibitor that results in a block of myosin II activation (Zhou et al. 2009). As a result of the drug treatments, the stiffness of the tissue, as measured using a 'nanoNewton force measurement device', was reduced at least by 50% for both treatments whereas an ECM component, fibrillar fibronectin, did not contribute to elasticity of the tissue. This suggests that actomyosin plays a major role in regulating elasticity of embryonic tissue. Similar stiffness reduction was observed, as measured by AFM, when retinal pigment epithelium was treated with either Y27632, Blebbistatin, or Cytochalasin D (Eiraku et al. 2011). Moreover, outer hair cells in the mouse cochlea also showed a significant decrease in stiffness, as measured by AFM, after latrunculin A treatment at early postnatal stages (P0 and P3) (Szarama et al. 2012). In the chick embryo, stiffness of the anterior intestinal portal, where the heart tube forms, was

significantly decreased after treatment with blebbistatin, a myosin-II inhibitor. The opening angle after incision of this region also showed a significant reduction following drug treatment, which suggests that contractility of the tissue is related to myosin-II activity (Varner and Taber 2012). In other studies, microtubule function has also been linked to tissue elasticity. Zhou et al. (2010) found that microtubule depolymerisation by nocodazole caused stiffening of the dorsal *Xenopus* isolate. However, decreasing microtubule density released Xlfc, a Rho-GEF, whose increased concentration led to an increase in RhoA activity (Chang et al. 2008). This in turn induced actomyosin contractility, which is probably the actual cause of the alteration in tissue stiffness (Zhou et al. 2010). Interestingly, pillar cells of the postnatal day 5 mouse cochlea showed a significant reduction in stiffness after nocodazole treatment (Szarama et al. 2012), suggesting that response to microtubule depolymerisation is dependent on the tissue context.

In this Chapter, the analysis of *Kumba* (*Zic2^{Ku/Ku}*) embryos, that develop extensive spinal neurulation defects, was extended to measurement of neural plate stiffness using AFM. Recent work from our lab has revealed excessive apical accumulation of actomyosin, in association with significant over-activation of RhoA, in the NP of *Zic2^{Ku/Ku}* embryos compared with wild-type littermates (Escuin et al. unpublished). In view of this work, and the previous findings on the role of actomyosin in determining the elasticity of embryonic tissues, it was hypothesised that the NP of *Kumba* mutant embryos might show an increase in stiffness compared to wild-type.

Figure 5.1. Schematic of AFM working principles and force-distance curve analysis.

(A) A laser beam is reflected onto the back of the cantilever. Cantilever deflection is sensed by a photodiode on the light path of the laser. The approach and contact of the cantilever tip with the sample can be precisely controlled by a piezo electric ceramic. For sample preparation, the ventral midline of the PNP was bisected and a single NF was immobilised on a tissue culture dish, with apical NP surface upwards. AFM measurements were performed at multiple locations on the NP, keeping track of the dorso-ventral and rostro-caudal positions of each measurement along the PNP.

(B) Captured image of force-distance curve analysis on JPK data processing software. The upper curve indicates an 'approaching' period where the probe approaches the sample and starts to indent. The lower curve indicates a 'retracting' period where the probe retracts from the sample. The x-axis of the graph is a tip-sample separation distance, minus-range of which represents indentation depth. The y-axis shows the deflection level of the cantilever, which represents the applied force, by Hooke's law. The dark blue arrow indicates the range where the Herztian fitting was performed. The red arrow indicates indentation depth. The orange box indicates 'Residual RMS', the value of which is used to determine the quality of the fitting. The red box shows Young's modulus, as an output of the Herztian fitting in the grey-shaded range (equivalent to the dark blue arrow range).

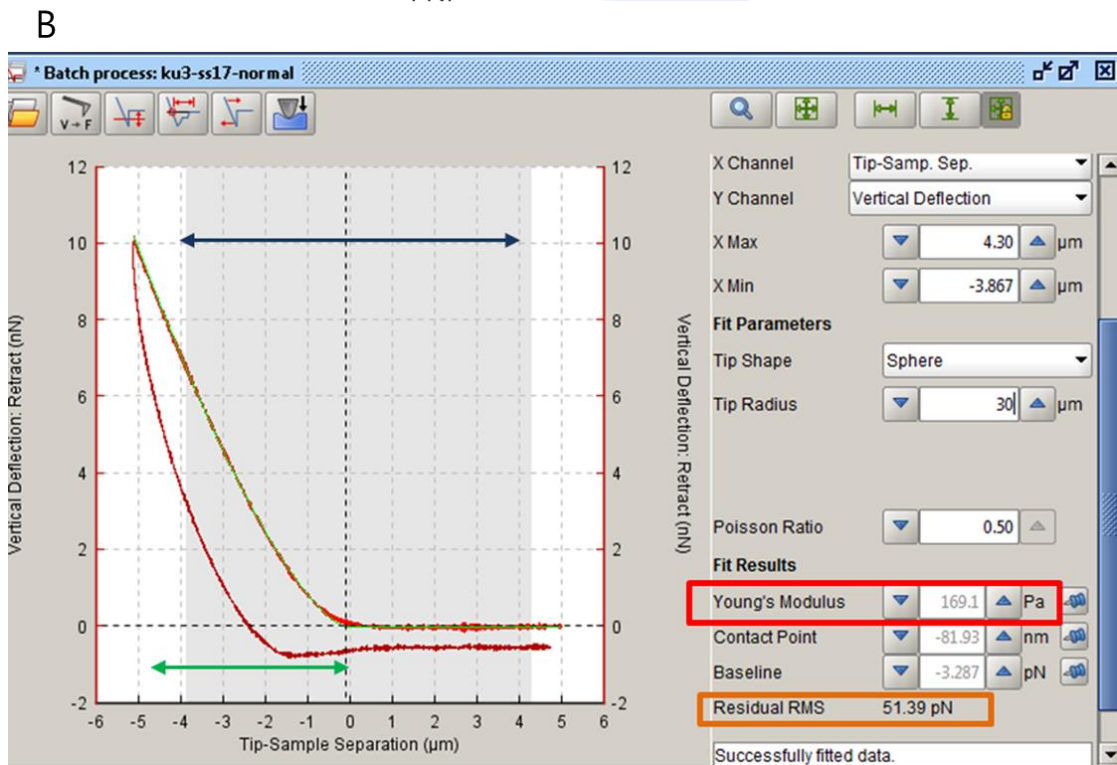
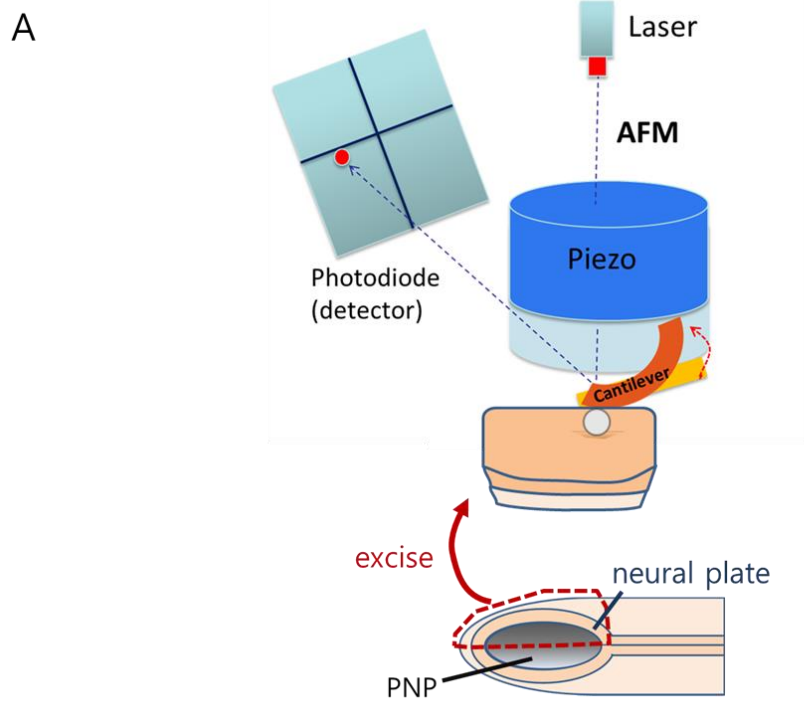


Figure 5.1. Schematic of AFM working principles and force-distance curve analysis.

5.2. Results

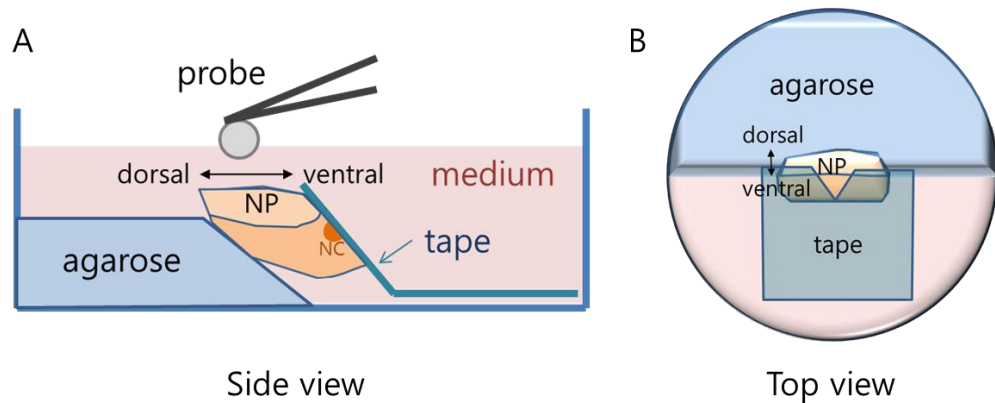
5.2.1. Sample immobilisation method and tissue viability

A sample should stay flat and firmly attached to a substrate or petri dish surface during AFM measurements, in order for reliable stiffness measurements to be possible. In initial studies, a bio-adhesive (Cell-Tak), which is an extract form of polyphenolic protein from mussel, was used to immobilise the neural plate explant on a petri dish. However, the tissue tended to detach once the medium was poured into the dish. To prevent this, longer incubation periods with Cell-Tak were used, to enable firmer adhesion. However, the explants became slightly dry and this aggravated the viability of the tissue (data not shown).

Therefore, it was necessary to find a way to mechanically confine the sample on the dish without using a biochemical-coating method. After incising the ventral midline of the neural tube, one of the two NP explants was gently laid on the slope of an agarose mould, with the apical side of the NP facing upwards (Figure 5.2 (1)). Then, transparent tape, half of which had been previously attached to the agarose-free area of the dish, was laid against the other side of the sample to immobilise it. The key principle of this method was to use the elastic properties of a tape to gently press the sample against the deformable agarose.

The viability of NP explants was investigated using a cell death marker propidium iodide (PI). PI is cell-impermeable and when the membrane is compromised, it can enter the cell and bind to nuclei acids, then fluorescing red. It was found that, up to 3 hours after the incision, the NP within each explant remained viable whereas other parts, mainly mesenchymal tissues, started going through apoptosis soon after the incision (Figure 5.3 D,H). After 3 hours, the NP regions of explants also appeared PI-positive, although this proved to be a reflected image from the opposite side (surface ectoderm) of the explant. When explants were removed from the mould and examined at various angles, fluorescence of PI was found to be largely absent from the NP (data not shown). In short, the NP region was viable for at least 3 hours following explantation and, considering that each NP explant took normally 40 minutes from the set-up procedure to the actual AFM measurement, this NP viability timeline allowed 4 NP explants to be probed by AFM from each litter of embryos. Interestingly, during these experiments it was noted that PI has possible adverse effects on NP elasticity. Therefore, PI was not added during the AFM measurements.

(1)



(2)

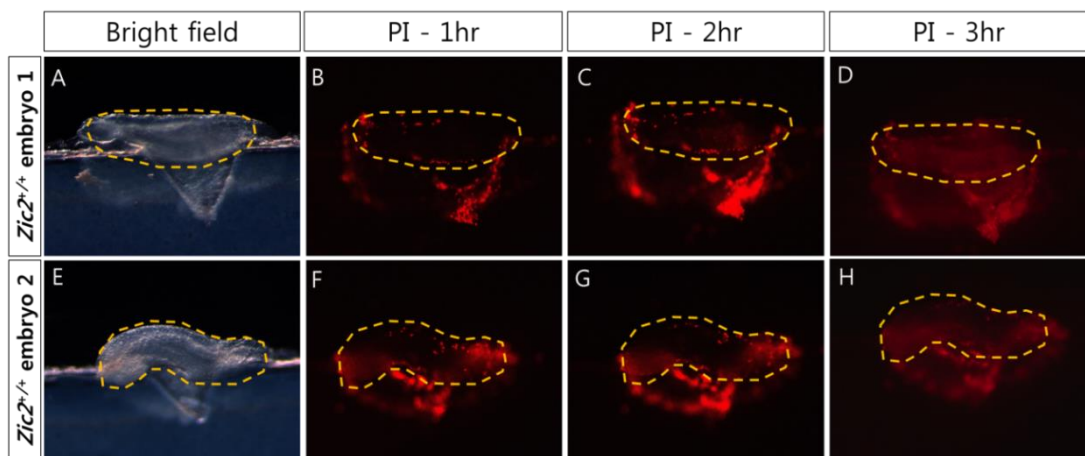


Figure 5.2. Schematic of NP immobilisation method and test of NP viability.

(1) (A-B). Immobilisation of the NP explant in side view (A), and top view (B). An NP explant was gently laid on the slope of an agarose mould with its apical surface facing upwards. Transparent tape was then gently placed against the edge of the explant in order to hold it in place. The dish was filled with culture medium, and the AFM probe was applied to the NP surface through the culture medium interface. NP and NC represents the neural plate and the notochord, respectively.

(2) (A-H). Assessing viability of the NP over time in two wild-type explants: embryo 1 (ss20) (A-D), and embryo 2 (ss20) (E-H). Yellow dashed line indicates the boundary of the NP. Bright field views are shown in (A,E). Propidium iodide (PI) staining is shown 1 hr (B,F), 2 hr (C,G) and 3 hr (D,H) after application of the stain. PI staining appears more prominent after 3 hr, although this staining was found to be in non-NP cells on the underside side of the explants, not in the NP itself (not shown)

5.2.2. AFM measurement

A glass bead was attached to the AFM cantilever to allow for a well-controlled tip-sample contact geometry, for a gradual pressure build-up, and to sample elasticity over areas comparable to the cellular apical area. Cellular apical area was not measured in this experiment, but mean cell width on the transverse plane was previously estimated to be around 5 μm (McShane et al. unpublished). And it was important that the probing interval, which was grid-controlled on the software, should be larger than the mean single cell size, in order to avoid probing the same cell twice. In our experiment, the probing interval was maintained at 12.5 μm , which is more than twice as large as the mean cell width. The diameter of the bead that was chosen for AFM measurement was around 60-70 μm , covering enough number of cells to sample averaged elasticity of them.

For analysis of AFM measurements, embryos were grouped into somite stages ss16-17 and ss18-23 to match as closely as possible the somite stages of embryos in the earlier incision experiments (ss13-16 and ss17-23). Due to time constraints, no embryos younger than ss16 could be collected for AFM measurement, and so ss16-17 was chosen as the younger group.

In preparing NP explants from the PNP of *Kumba* mutant embryos, it was not straightforward to take the explant from exactly corresponding locations among the different genotypes and somite stages, as the PNP varied considerably in length and was longer in mutant than heterozygous or wild-type embryos. For example, at ss16-17, the mutant already showed a slightly enlarged PNP compared with wild-type and heterozygotes (Figure 5.3 A). Moreover, at the more advanced stage (ss18-23), the PNP in mutant embryos was greatly elongated, relative to that of normally developing embryos in which the PNP was gradually shortening as closure progressed (see Table 4.1). It was impossible to make AFM measurements on the whole open NP of the mutant, due to time constraints of the measurement. Therefore, I decided to concentrate on NP measurements at a similar distance along the body axis (i.e. a similar distance from the caudal end). Hence, in the ss18-23 mutant where the PNP was much enlarged, the region near the closing point was not considered for analysis (Figure 5.3 A).

Figure 5.3 AFM of *Kumba* embryos: NP region excised and elasticity data.

(A) Schematic showing the excised NP regions for different genotypes in the ss16-17 and ss18-23 groups. For ss16-17, the PNP of the mutant embryos is only a little longer than that of wild-type or heterozygous embryos, and so comparable NP regions could be excised and measured. For ss18-23, however, the PNP of mutants is more than twice as long as that of wild-type or heterozygous embryos (see Table 4.1). Therefore, it was decided to measure a NP region in the mutant that was at an equivalent axial level to the region measured in normally developing embryos (red dashed boxes). The blue dashed box indicates the mutant PNP region that was not measured.

(B) NP stiffness (Pa) plotted against *Kumba* genotype and NP region for embryos at ss16-17. Each data point represents a single AFM measurement on the NP. Mean \pm SEM values for each set of data are shown. Mutant embryos had significantly greater stiffness than both wild-type and heterozygous. The stiffness of heterozygous embryos was also significantly larger than wild-type. In all genotypes, the stiffness of the ventral region was significantly larger than that of the dorsal region ($p < 0.001$ for both genotypes and dorso-ventral levels, two-way ANOVA, followed by Holm-Sidak multiple comparison procedures, significance level: $p = 0.05$). For dorsal, WT (N = 2, n = 43), Het (2, 29), Mut (2, 52). For ventral, WT (2, 32), Het (2, 34), Mut (2, 37). N: the number of embryos; n: the number of measured points.

(C) NP stiffness of *Kumba* embryos at ss18-23. Stiffness of genotypes and dorso-ventral levels could not be compared statistically due to their significant interactions ($p < 0.001$, two-way ANOVA). When genotypes were compared for dorsal or ventral regions separately, stiffness of the wild-type was significantly greater than the mutant in the dorsal region ($p = 0.035$, Kruskal-Wallis one-way ANOVA on ranks with Dunn's multiple comparison procedures, significance level: $p = 0.05$). In the ventral region, the three genotypes were all significantly different from each other in descending order, from heterozygous to wild-type ($p < 0.001$, Kruskal-Wallis one-way ANOVA on ranks with Dunn's multiple comparison procedures, significance level: $p=0.05$). However, significance marks are not presented here due to unreliability of the ss18-23 stiffness data (see explanation in the text). For dorsal, WT (N = 7, n = 139), HET (8, 125), Mut (5, 105). For ventral WT (7, 177), HET (8, 110), Mut (5, 85). N: the number of embryos, n: the number of measured points.

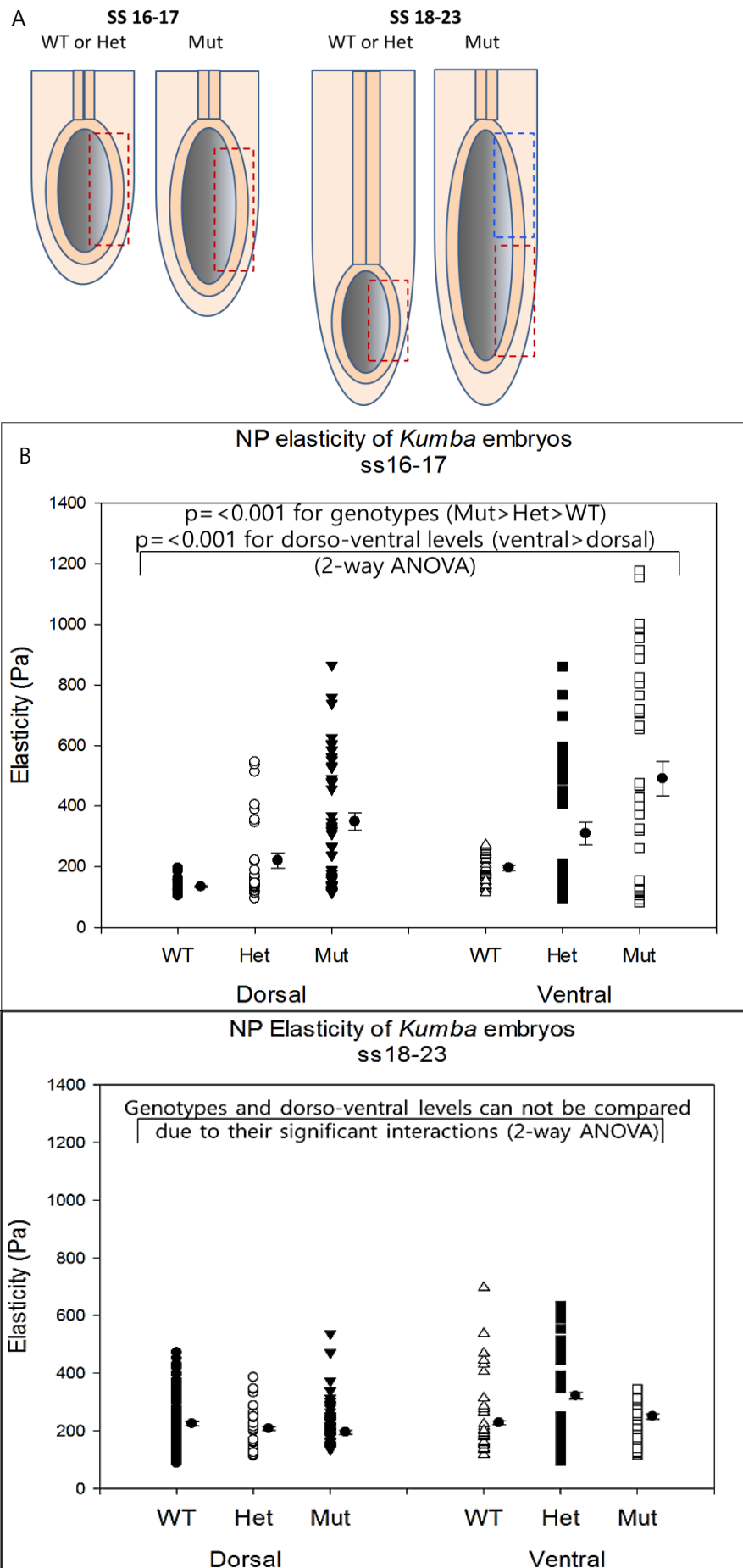


Figure 5.3 AFM of *Kumba* embryos: NP region excised and elasticity data.

AFM measurements revealed that, in the ss16-17 group, *Zic2*^{Ku/Ku} NPs showed a significant increase in stiffness compared with wild-type and heterozygous and, interestingly, *Zic2*^{Ku/+} showed an intermediate stiffness value between wild-type and mutant embryos (Figure 5.3 B). Moreover, stiffness of the ventral NP was significantly greater than of the dorsal NP.

In contrast, in the ss18-23 group, stiffness values between genotypes and dorso-ventral levels could not be properly compared statistically because the stiffness difference between genotypes behave differently for the dorsal and ventral parts (Figure 5.3 C). Therefore, stiffness values for the three genotypes were compared separately for dorsal and ventral NP regions. This showed that, in the dorsal region, the stiffness of the mutant embryos was significantly greater than for wild-type embryos. In the ventral region, the three genotypes were all significantly different from each other, in descending order from heterozygous to wild-type.

The inconsistency of the data trends between genotypes with regard to each NP level was probably because the stiffness values of ss18-23 embryos did not reflect the real differences between genotypes. One possible explanation for this can be deduced from the work in Chapter 4, where I observed greater NF re-opening in the mutant embryos after incision. This suggests that the closing point of the *Kumba* mutant PNP is under significantly greater tension than wild-type, probably reflecting different mechanical properties of the NP. Based on this finding, it can be hypothesised that the greatest difference in mechanical properties of the NP amongst genotypes would be observed near to the point of PNP closure. However, for ss18-23 *Kumba* embryos, the region near to the closing point was not examined by AFM because of the decision to measure stiffness in the PNP of mutant embryos at a similar axial level as in wild-type and heterozygous embryos. Therefore, it is likely that the main difference in NP stiffness among genotypes was not properly compared for the ss18-23 group.

Next, the elasticity data of ss16-17 and ss18-23 were compared for each dorsal/ventral level. However, two-way ANOVA using a comparison between somite stage groups and genotypes was difficult to interpret statistically, due to the significant interactions between these two variables. When values for all the genotypes were combined, it was found that the stiffness of ss18-23 was significantly greater than for ss16-17, for both dorsal and dorsal-ventral combined NPs (Figure 5.4). For the ventral region alone, there was no significant difference between somite stages.

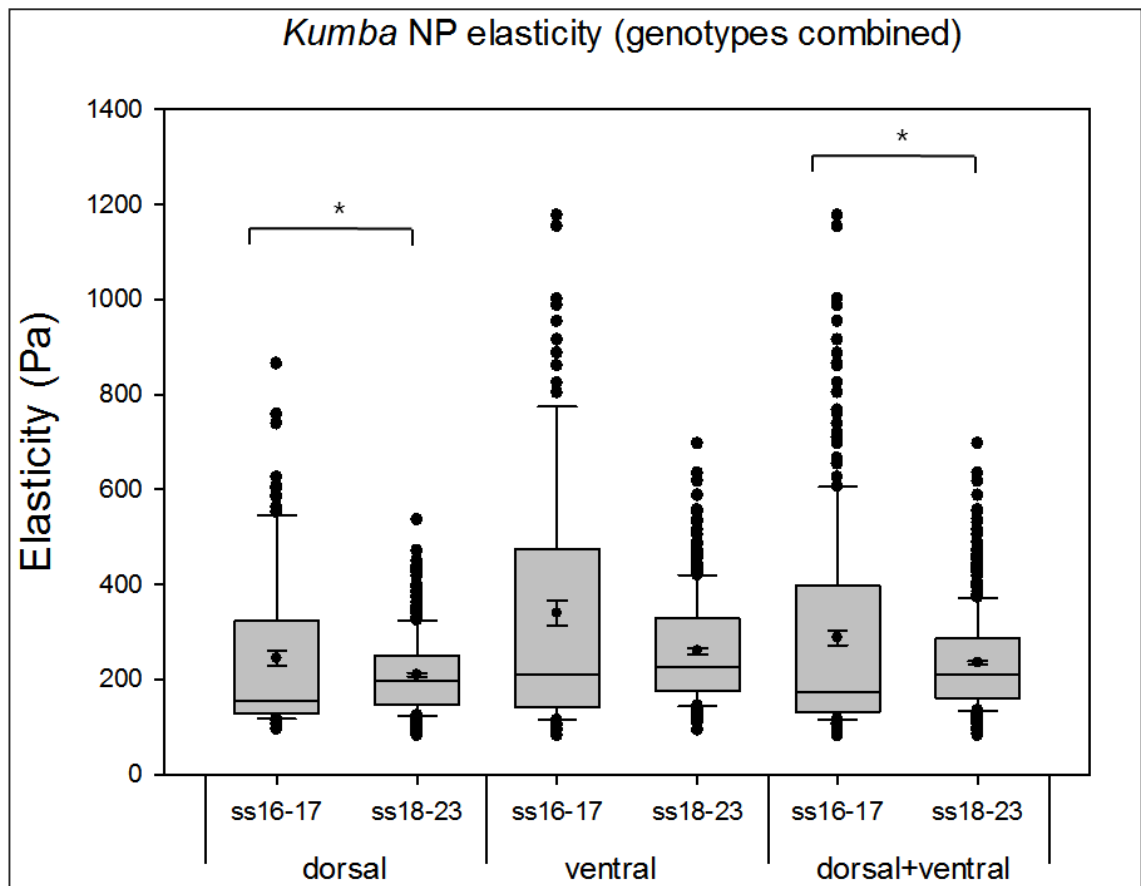


Figure 5.4 NP elasticity comparison between ss16-17 and ss18-23 *Kumba* NP.

Box and whisker plots in which the box shows the 1st and 3rd quartiles, around the median (line within box), and outliers are shown as individual points. The mean value and error bars (SEM) are also included within the box. For the dorsal NP, the ss18-23 values were significantly greater than for ss16-17 ($p = 0.040$). For the ventral NP, there was no significant difference between somite stages ($p = 0.755$). For dorsal and ventral combined, the ss18-23 value were significantly greater than for ss16-17 ($p = 0.05$). The number of measured points (n) were 124 for dorsal and ss16-17, 369 for dorsal and ss18-23, 103 for ventral and ss16-17, 372 for ventral and ss18-23. All tests were performed with Mann-Whitney Rank Sum Test. *: $p < 0.05$.

5.3. Discussion

5.3.1. Sample immobilising method and tissue viability

For AFM measurements, a firm adhesion of the sample to its substrate is essential. The tubular shape of the intact caudal region made it difficult to immobilise the structure as a whole and, moreover, the NP was largely inaccessible for AFM measurement after this procedure. Excision and immobilisation of single NFs was therefore necessary, to provide access to the NP surface. In one previous study, it was found that adsorption onto polyphenolic protein (Cell-Tak) coated surfaces was the most effective in sample immobilisation compared to other methods: glass-using physical confinement, physisorption to positively charged surfaces, and covalent binding to amine- or carboxyl-terminated surfaces (Louise Meyer et al. 2010). However, this study was limited to bacterial cells. Our experiments showed that the Cell-Tak method was inappropriate for mouse embryonic tissues perhaps because they have more dynamic 3D structure which may act as a hindrance to firm adhesion. In another study, the whole embryo was fixed in an agar mould and AFM-probed (Efremov et al. 2011), but this method was also inapplicable for our use as the apical side of the NP needed to face upwards in our experiment, and it was very hard to orientate the whole embryo in a solidifying agar mould to achieve this. Therefore, an excision method was chosen in order to handle the explant in a controlled manner, and to be able to best immobilise the explant physically for AFM measurement.

Using Propidium Iodide (PI) staining to reveal cells with compromised plasma membranes, it was confirmed that NP tissue stays viable for the duration of AFM measurements. However, during the actual AFM measurement, PI was not used due to possible adverse effects on tissue elasticity. Moreover, frequent fluorescent light exposure to check the PI staining may also have affected viability of the tissue.

NP excision might have caused the possible loss of pre-stress in the tissue (Zamir and Taber 2004). In our study, however, it was impossible to measure NP stiffness of the whole intact embryo (i.e. pre-stress), due to the technical difficulties of immobilising the embryo for AFM measurement. Therefore, pre-stress was not taken into account in the present experiment.

5.3.2. AFM measurements

For ss16-17 embryos, the NP of *Zic2^{Ku/Ku}* was found to be significantly stiffer than wild-type and heterozygous embryos. This result was also consistent with the NF re-opening results, in which significantly greater NF re-opening occurred following incision in mutants than in normally developing embryos (see Chapter 4.2.2). However, the stiffness of heterozygous embryos was still significantly larger than wild-type embryos, which suggests that the *Zic2^{Ku}* heterozygote has a partially penetrant phenotype, with some similarities to the homozygous mutant. This is consistent with my previous results that basal NP width and nuclear circularity values in heterozygotes were intermediate between the values of wild-type and mutant. Also, in previous work it was shown that *Zic2^{Ku}* heterozygotes occasionally exhibit spina bifida (Elms et al. 2003). It was also found that the ventral NP region showed greater stiffness than the dorsal NP region for ss16-17 embryos. One possible explanation for this is that the ventral margin of the NP was gently pressed by adhesive tape for immobilisation purpose, and that the physical confinement might have contributed to the increase in stiffness particularly in the adjacent ventral region.

Particularly for ss16-17 embryos, the mutant NP showed great variances in the stiffness values for both dorsal and ventral parts, compared with other genotypes. In order to explain this, for each genotype, the standard deviation between the mean values of each embryo (N=2 for each genotype) was compared. As a result, the standard deviation values between the mean of each embryo were measured 14.5, 155.6, and 245.9, for the dorsal parts of wild-type, heterozygous, and mutant, respectively, and 50.0, 294.5, and 388.7 for the ventral parts of wild-type, heterozygous, and mutant, respectively. These results strongly suggest that the large variance in stiffness data of the mutant NP is not due to inherently varying stiffness values of the mutant NP itself, but most likely due to distantly clustered dataset of the two embryo samples. The observed larger mean of the mutant NP than others could be interpreted with the same explanation. Therefore, more NP samples are required for completion of this analysis.

For ss18-23 embryos, it is more difficult to draw definite conclusions about the elasticity of the NP in the different *Kumba* genotypes. Interactions in the two-way ANOVA prevented a valid comparison of the difference between genotypes, across both dorso-ventral levels. One-way ANOVA separately for each dorso-ventral level demonstrated that, unlike with ss16-17, there were considerable inconsistencies of elasticity values for

the genotypes at ss18-23. In the dorsal region, the elasticity of wild-type and mutant embryos were largest and smallest, respectively, whereas in the ventral region, the stiffness of heterozygous and wild-type embryos were largest and smallest, respectively. This inconsistency of findings may have originated from the mismatch between the region of the NP collected from normally developing embryos (wild-type and heterozygous) and that from mutant embryos. The PNP of the *Zic2^{Ku}* mutant became much longer at E9.5 compared to E9.0, while the PNP of wild-type and heterozygous embryos became shorter at E9.5 compared to E9.0. Since it was not possible to measure NP elasticity for all positions along the mutant PNP, it was decided to match the anteroposterior axis level of the NP sample among the different genotypes. Hence, the NP of mutant embryos was measured only in a region at considerable distance from the closing point (Figure 5.3 A), unlike the normally developing control embryos which were measured near to the closing point. In retrospect, this decision probably resulted in the loss of important mechanical information, as incision experiments in *Kumba* embryos (which were performed after the *Kumba* AFM measurements) revealed that the NF re-opening was the largest in the mutant, perhaps indicating increased stiffness at the closing point.

AFM results showed that stiffness of the NP mostly ranged between 100 Pa and 400 Pa, in the normally developing embryos for both somite stage groups. In a mouse ES cell-driven optic-cup morphogenesis study, stiffness of the neural retina and retinal pigment epithelium were measured approximately at 150 and 400 Pa, respectively, as measured by AFM (Eiraku et al. 2011). Even though those two studies were based on different tissues of mice, it is notable that the two living tissues have approximately the same values, demonstrating the validity of our AFM measurement.

When the NP stiffness values of ss16-17 and ss18-23 embryos were compared, for the dorsal and ventral levels combined, the stiffness at ss18-23 was found to be significantly larger than at ss16-17 (a 1.2-fold increase in median value). Similar results were found in other animal models. For example, the dorsal axial and paraxial tissues of the frog embryo showed a 4-fold increase in stiffness (from 20 Pa to 80 Pa) from gastrula stage to early neural tube stage. This dramatic increase in stiffness was thought to be associated with dorsal elongation, and the presence of presomitic mesoderm which had a particularly stiff tissue structure (Zhou et al. 2009). Moreover, in chick embryos, when the stiffness of different regions of the brain tube was measured, there was a general

trend of increasing stiffness for most regions as the brain developed (Xu et al. 2010). In mouse embryos, the NP stiffness difference between different stages of neural tube closure needs to be further investigated in association with the major stiffness-determining factors such as actomyosin. One previous study showed apically-localised F-actin (by phalloidin staining) throughout the neuroepithelium at all three different stages of spinal neural tube closure, with no visually discernible difference in phalloidin staining pattern between the 12 and 26 somite stages (Ybot-Gonzalez and Copp 1999). However, this study did not quantitatively assess the actomyosin activity in the developing NP, and this might alter with development, leading to the increasing stiffness observed in my experiments.

6. Modelling of neural tube closure using the Finite Element Method (FEM)

6.1. Introduction

6.1.1. The uses of FEM in understanding neural tube closure

In previous chapters, incision experiments were performed to determine whether there is tension within the closing NFs that originates from the closing point of the PNP (see Chapter 3). Incision of the most recently closed region of NT led to NF re-opening that was most marked near the closure point, but also observed throughout the PNP. This result suggests that the tension (i.e. NP pull-in force) plays a role in pulling the NFs inward during neural tube closure. Since this type of force is not easily measured directly, an alternative approach was taken: Finite Element Method (FEM) modelling.

FEM is a method used to computationally solve the force equilibrium equations of a solid body (e.g. tissue) (Reddy 1993). Here, the solid body is dealt with as a continuum and is divided into subdomains of geometrically simple shapes, or discrete (finite) elements. Displacement (deformation) of the solid body, in response to external forces, is then calculated over the elements, through which strain and stress fields within each element can be estimated. To be more specific, a function for the relationship between displacement and external force is first mathematically described for each element, using shape function, which varies depending on the element shape (e.g. a triangle or rectangle), and constitutive relationship (elastic modulus if linear elastic material is assumed). The function for each element is expressed in the form of matrix through linear algebra equations. Then, the matrices of all the elements are integrated and the equations are solved to predict the behaviour of the global system.

FEM has been used in the analysis of many different morphogenetic processes including neurulation. In the past, neurulation modelling was mostly focused on 2D (Odell et al. 1981) or simplified-3D bending models of the neuroepithelium (Jacobson et al. 1986). Relatively recently, neurulation in the whole amphibian embryo was simulated using real 3D geometry data and physically measured mechanical properties. Moreover, the effects of Shroom-dependent neural ridge formation and lamellipodium-driven convergent extension were studied by changing related mechanical parameters (Chen and Brodland 2008).

For our modelling, the 3D geometry of the NP was first drawn in the software. Then,

by applying certain displacement conditions, the closure of the structure from one end to the other end (i.e. zipping neural tube closure) was simulated using FEM. The forces acting at certain locations within the structure were investigated during the process of closure. Additionally, and of particular relevance to the experimental chapters of this thesis, I used FEM analysis to examine whether the bending degree of the NP was affected by the closure process.

I also applied the FEM method to the analysis of closure in the *Kumba* mouse (see Chapter 5). The stiffness of the NP in mutant embryos was found to be greater than in wild-type and the heterozygous embryos. In order to determine how the stiffness of the NP could affect neural tube closure, the dorsal closing force was calculated and compared between genotypes using FEM. This modelling was intended to test the hypothesis that a larger NP pull-in force would be required to achieve closure in embryos, such as *Zic2^{Ku/Ku}*, whose NP has increased elasticity (i.e. stiffer NP).

Moreover, at the onset of the spinal neurulation defect, *Kumba* mutant embryos showed a reduced basal NP width and mean NP thickness, compared with wild-type (see Chapter 4). Hence, I applied the FEM approach to determine how the closing force would be affected when the geometries and structures of *Zic2^{Ku/Ku}* and the wild-type were differentiated, based on the morphological differences experimentally measured.

6.2. Results

6.2.1. Distribution of dorsal closing force along the longitudinal axis and stress profiles during neural tube closure

During neural tube closure, the NP is firmly attached by extracellular matrix to the SE and paraxial mesoderm (Lawson et al. 2001). In the modelling, however, the geometry and dynamics of only the NP were studied excluding other tissue layers; it is simpler to simulate the motion of a monolayer. Moreover, possible mechanical roles of paraxial mesoderm and SE in DLHP formation were found to be dispensable, in that the majority of each tissue could be removed without preventing DLHP formation or the continuation of spinal closure in cultured embryos (Ybot-Gonzalez et al. 2002).

In the geometry part of the modelling, NP structure was drawn as closely as possible to the actual NP shape reflecting its width and the angle of MHP and DLHP (Figure 6.1 B) for E9.5 embryos. Then, by applying displacement conditions to the dorsal edge of the NF along the longitudinal axis (Figure 2.2), the open NP was set to come into apposition from one end to the other end (Figure 6.1 C-E). The NF dorsal edge line was equally divided by 10, and at each time point of the closure, the closing forces (i.e. the force component towards the symmetry plane) exerted at each sub-line were calculated as the average over each segment.

As a result, it was shown that the closing force peaks at the most recently closed segment. For example, at $t = 1.1s$, when the tube is closed halfway through, the peak of the force at this time appears at the 5th segment (sky blue graph in Figure 6.1 A), which corresponds to the most recently closed segment (Figure 6.1. D). In addition, the closing force diminishes with distance in both directions at each time point (Figure 6.1 A). Interestingly, the rate of diminution is greater towards the caudal (unclosed) end than towards the rostral (already closed) end. In the graph (Figure 6.1 A), however, the force profiles at the first two segments (i.e. 1st and 2nd segments) were not considered valid as, in the simulation, the NP starts to close from the open end at this level, and the closing force at the first two segments are likely to be different from the actual case of neural tube closure in which the NP is continuing to close from the rostrally closed region. For the same reason, the force profiles at the last two segments (i.e. 9th and 10th segments) were considered invalid.

The von-Mises stress (maximum stress) in the NP was also calculated during the time of neural tube closure (Figure 6.2). Immediately after the NP starts to approach each

other ($t=0.01$ sec), on the opposite side of the closing end, dorsally curved stress patterns were persistently observed until $t=1.4$ sec particularly in the DLHP region, with the NF region being under larger amount of stress than the non-bending region (more ventral to the DLHP region). From $t=1.0$ sec, the ventral-most region of the NP gradually starts to become stressed, resulting in ventrally curved stress patterns. Furthermore, these results suggest that the region-specific stress patterns might have a connection with cell curvature patterns (see Chapter 3.2.2); NP cells showed a tendency to be more dorsally curved in the dorsal half NP than in the ventral half NP, both at closing and open levels of the NP for E9.5 embryos. If this is the case, cells determine their curvature according to the stress distribution in the NP.

In conclusion, this modelling result coincides with the prediction in the neural tube case that the tension which originates from the closing point is present in the NF along the longitudinal axis and diminishes with distance particularly towards the caudal (unclosed) end. Moreover, the stress distribution in the transverse section of the closing neural tube demonstrated a possible correlation with cell curvature patterns in the NP.

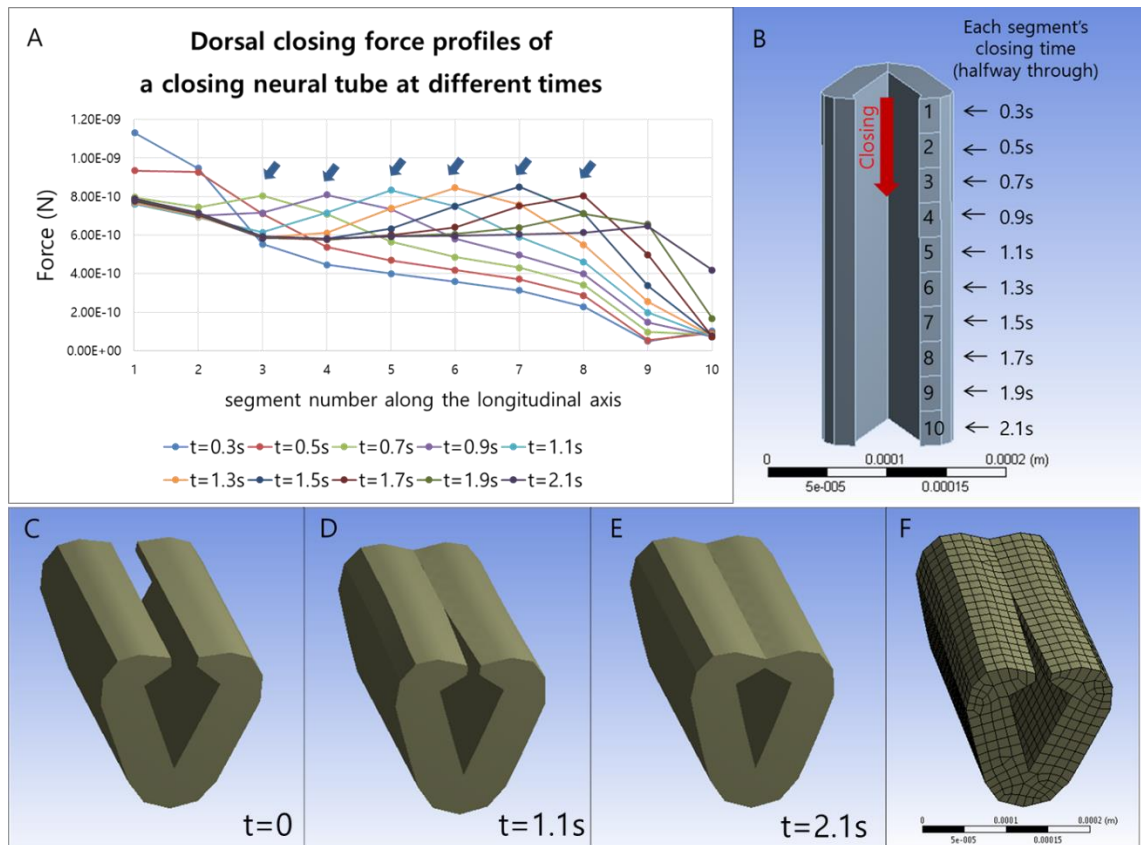


Figure 6.1 Temporal and spatial profiles of dorsal closing force.

(A) Dorsal closing force profiles at different times along the longitudinal axis. The force profiles at 1st, 2nd, 9th and 10th segments should be disregarded as the boundary conditions of these segments are different from those in the middle part of the axis, which are the continuously closing parts. Blue arrows indicate the peak forces at the most recently closed segments at different times. Forces show a gradually declining trend away from the recently closed segment, with a steeper decline along the open region and a less steep decline along the already closed neural tube.

(B) Schematic of the closing neural tube. The longitudinal side of the NF is divided into 10 segments and force at each segment was studied at different times through the closure simulation.

(C-E) Closing process of the neural tube during simulation. Initially open state ($t=0$ sec) (C), half closed state ($t=1.1$ sec) (D), and fully closed state ($t=2.1$ sec) (E).

(F) Example image of the mesh-formed (i.e. element-divided) neural tube.

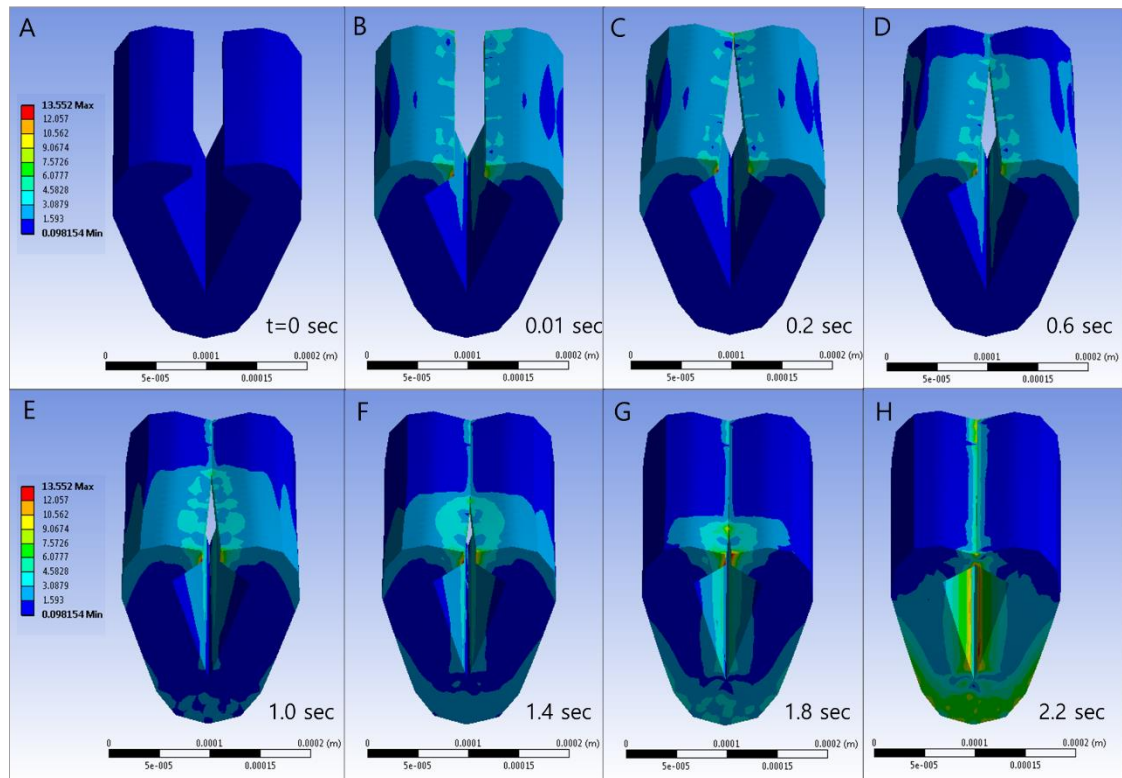


Figure 6.2 Stress profiles during neural tube closure.

(A-H) Stress profiles of the closing neural tube at different times. Initially open/stress-free state ($t=0$ sec) (A), closure-initiated state ($t=0.01$ sec) (B), $t=0.2$ sec (C), $t=0.6$ sec (D), $t=1.0$ sec (E), $t=1.4$ sec (F), $t=1.8$ sec (G), and closure-completed state ($t=2.2$ sec) (H). The color map depicted in (A) and (E) represents the maximum stress level (von-Mises) of the NP structure; red indicates the highest, and blue indicates the lowest (zero) stress level. Throughout the first two-thirds of the zippering process, dorsally curved stress patterns appear in the DLHP regions, opposite to the closure-initiated side, with the NF region being under larger amount of stress than the non-bending region (ventral to the DLHP region). From $t=1.0$ sec, approximately midway through the zippering process, the ventral region of the open NP gradually becomes stressed and the stress propagates dorsally towards the end of closure.

6.2.2. DLHP bending degree change during FEM-simulated closure

For the displacement conditions of the closure, only the symmetrical x co-ordinate points (medio-lateral axis) of the dorsal NF edge were manipulated, while the displacement of the y co-ordinate points (dorso-ventral axis) of the dorsal NF edge was 'ignored' as part of the programme functions. For example, the two symmetrical points of the NF edge, (-27, 65) and (27, 65) were set to join at (0, y₂), but y₂ value did not need to be specified in the displacement conditions applied, using the 'ignored' function in the software (Figure 2.2 B and 6.3 A,B). This way, the simulated-closure was designed to occur naturally, perhaps in a mechanically favourable manner. If the y₂ value is specified, the NF tips have to be joint at the y₂ point regardless of energy/force preference of the system during the motion, which might cause mechanical distortion of the NP structure.

X-Y plane images of the neural tube were captured on the FEM before and after simulated-closure, at the same magnification level. Then, DLHP bending degree on the images was compared, using the same measurement method as for section-based DLHP bending degree. As a striking result, DLHP bending degree increased from 2.34 μm to 3.83 μm after closure, which is approximately a 1.6-fold increase (Figure 6.3 A,B). This result strongly suggests that the closure process itself contributes to dorsolateral bending of the NP. Moreover, this result is consistent in a converse manner with the incision experiment results (see Chapter 3.2.1), where the NFs sprang apart, losing nearly 50% of the DLHP bending degree after incision at the closing level (Dil-marked level).

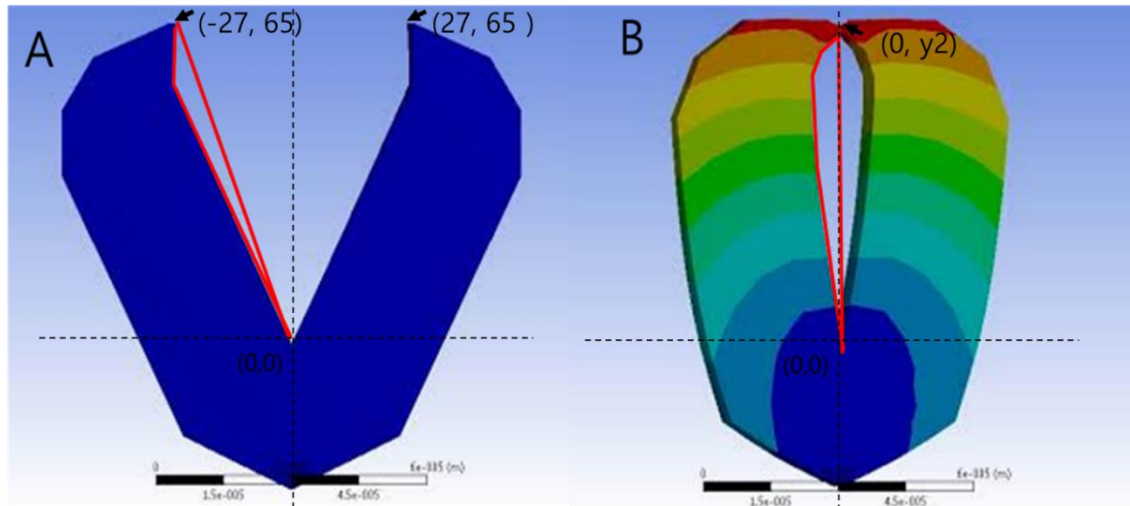


Figure 6.3 DLHP bending degree change in FEM after simulated closure.

(A) NP before simulated closure. The calculated value for DLHP bending degree is $2.34 \mu\text{m}$.

(B) After simulated closure. The calculated value for DLHP bending degree is $3.83 \mu\text{m}$. DLHP bending degree is measured by dividing the area bounded by the red lines by the length of the straight line that connects NF tip and the MHP. Measurements for the two images were performed at the same scale. The color map depicted in (B) represents the map of the deformation level of the elements in the NP structure after closure; red indicates the largest, and blue indicates the least (zero) deformation. Black arrows indicate the NF tips, whose coordinates are preset, before initiating simulation, as (-27, 65), (27, 65), and (0, y2) for the NPs on the left side in (A), on the right side in (A), and in (B), respectively. The y2 value was not specified but left as a blank (Figure 2.2B), so that the bending occurred in a mechanically favourable manner. After the simulation, y2 value turned out to be 64.

6.2.3. *Kumba* morphology and its effect on dorsal closing force

Basal NP width and NP thickness of *Kumba* embryos were found to be smaller than that of wild-type embryos at the onset of the spinal neurulation defect (see Chapter 4). In order to investigate the effect of basal NP width on dorsal closing force, in the geometry part of the modelling, basal NP width was drawn with length 199.7 for mutant and 267.3 μm for wild-type, while keeping NP thickness constant at 30 μm (Figure 6.4 A,B). Similarly, in order to test the effect of NP thickness on dorsal closing force, NP thickness was varied between 30 μm for wild-type and 25 μm for mutant, using the NP shape in Chapter 6.2.2 as a geometry template (Figure 6.5 A,B). These values were based on the results in Chapter 4.2.1 (Figure 4.2). However, the both variables (i.e. basal NP width and NP thickness) inputted into the modelling were slightly different from the experimentally measured data, and this was because there was a limitation revealed, while keeping other measures (e.g. initial NF tip-to-tip distance (54 μm), NF tip shape, stiffness of the NP (100 Pa), and NP thickness or basal NP width) constant in the geometry design. The closing forces at the 5th, 6th, 7th and 8th segments obtained from the simulation at time points 1.1, 1.3, 1.5 and 1.7 sec, which are equivalent to the time of each segment's closure, were compared to determine the effect of basal NP width and thickness variation on the force required for neural tube closure. The duration of the simulated-closure was set just 2.2 sec for time efficiency, which is considerably shorter than real neural tube closure time (2 hours for every somite pair formation). However, when the total duration of the modelling was prolonged 100 times (i.e. 220 sec), the dorsal closing force profiles showed an identical pattern with exactly the same values, suggesting that variation in the duration of the simulation does not affect the force profiles (data not shown).

The results show that *Kumba* mutant embryos with a smaller basal NP width require greater force for closure than the wild-type embryos (Figure 6.4 C), which can perhaps partly explain why the NFs of mutant embryos stop closing. Moreover, when NP thickness was reduced, there was a decrease in the required closing force (Figure 6.5 C), which suggests that thickening of the NP can play an inhibitory role in neural tube closure.

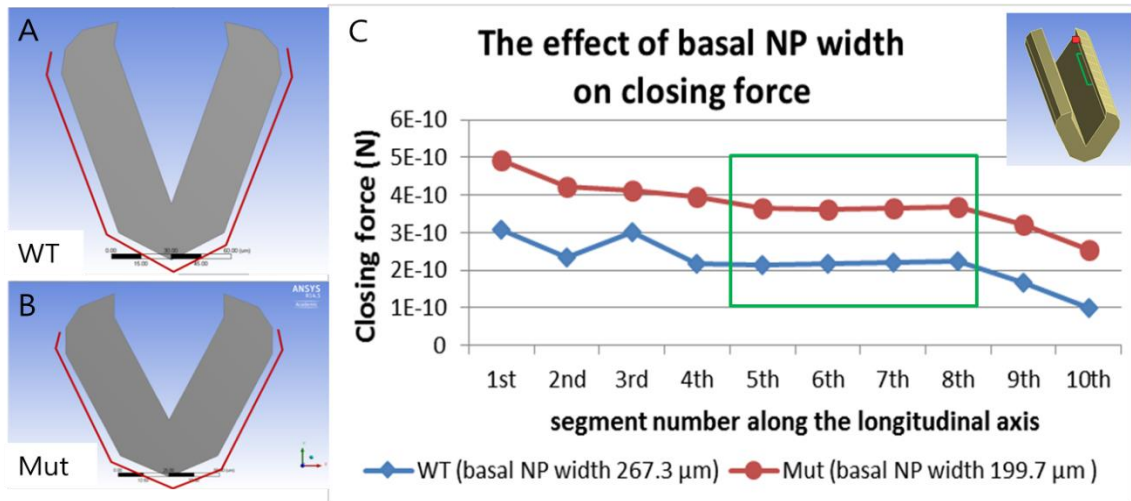


Figure 6.4 Effects of variation in basal NP width on the required dorsal closing force.

(A-B) Geometry inputs to simulate the NP of the *Kumba* mutant, with shorter basal NP width (B), compared with wild-type (A). Red lines indicate basal NP width.

(C) Closing force for each segment along the simulated neural tube of wild-type and mutant. The required force to achieve closure is larger in mutant, with a smaller basal NP width, than wild-type, with a normal basal NP width. The green box indicates a valid data zone, which corresponds to the closing force of the 5th to 8th segments (see a diagram at the top right).

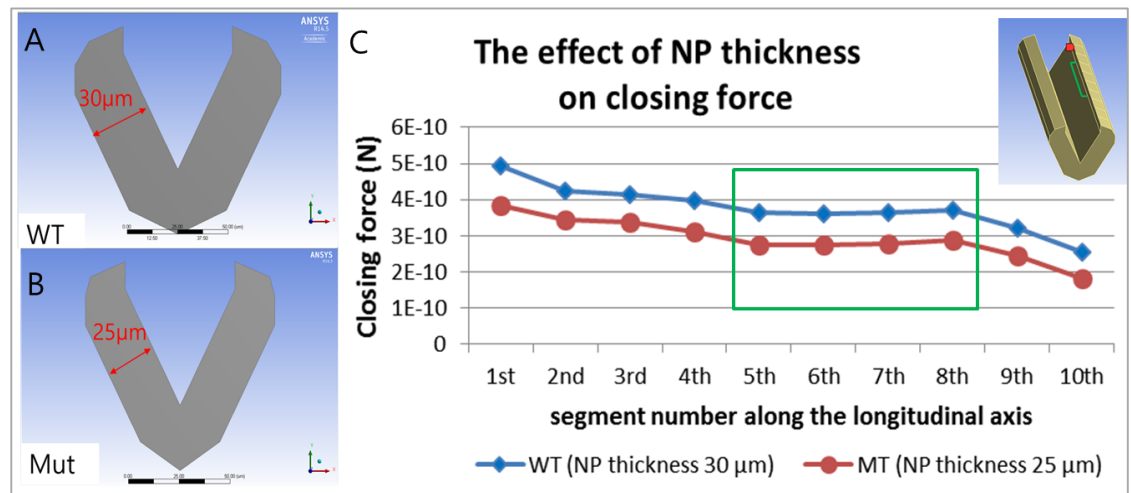


Figure 6.5 Effects of variation in NP thickness on the required dorsal closing force.

(A-B) Geometry inputs to simulate the NP of thickness 30 μm (WT) (A), and 25 μm (Mut) (B).

(C) Closing force for each segment along the simulated neural tube with the NP of thickness 30 μm and 25 μm. When NP thickness decreases from 30 to 25 μm, the force required for tube closure also decreases. The green box indicates a valid data zone as mentioned above.

6.2.4. Relationship between elasticity and dorsal closing force

Kumba mutant embryos showed a significant increase in NP elasticity compared with both wild-type and heterozygous embryos at the 16-17 somite stage (see Chapter 5). FEM was used to determine the relationship between elasticity of the NP and dorsal closing force.

The mean values of NP elasticity measured in Chapter 5 ranged from approximately 100 to 400 Pa. In the FEM simulation, elasticity (Young's modulus) of the material in the model was varied, to include values of 100, 200 and 300 Pa, while keeping all the other conditions constant; the shape of the NP from Chapter 6.2.2 was used as a geometry template. The elasticity of the material was adjusted in the modelling settings. It was confirmed that the dorsal closing force required for closure showed a linear increase with elasticity value, in the middle region of the tube - a valid data zone (Figure 6.6 B). The same effect was observed when simulated with a different geometry of the NP (data not shown). It seems likely that an increase in NP elasticity causes an escalation of the elastic recovery force of the bending NP. Then, at least an equal dorsal closing force is needed to balance the recovery force, in order for closure to progress. Therefore, this result suggests that a NP with a high elastic modulus requires a larger closing force to achieve closure than a NP with lower elasticity, consistent with the failure of closure to progress in *Kumba* mutant embryos at the 16-17 somite stage.

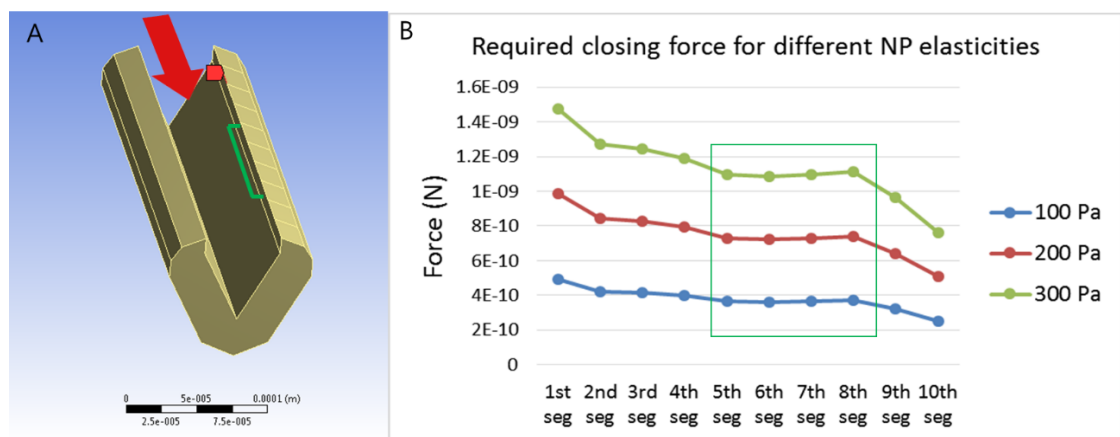


Figure 6.6 Closing forces for NPs with different elasticity values.

(A) Geometry input for the simulation. The green bracket shows the 5th to 8th segments, which were considered to provide valid FEM data for this comparison.

(B) Required closing force for NPs with elasticity values of 100, 200, and 300 Pa. The closing force required during closure has a linearly proportional relationship with the elasticity of the NP. Green box indicates the valid data zone.

6.3. Discussion

With the advance of computing technology, FEM has been increasingly used in biological research to better understand the mechanisms behind organisms' morphological changes and the physical variables (e.g. forces, velocities) involved. For example, in a study of heart tube formation of chick embryos, in order to determine which tissue layer, either endoderm or mesoderm, at the anterior intestinal portal played a major contractile role, each layer was given a different contractility value in the modelling (Varner and Taber 2012). Then, after simulated incision, the deformed contour of the structure in each case was compared with the contour change in the real animal model. Similarly, in order to determine whether circumferential residual stress in the chick brain tube affects indentation stiffness, the brain tube was modelled as a cylinder and the computed stiffness of the cylindrical tissue was compared before and after a simulated cut (Xu et al. 2010). Lastly, in the zebrafish tailbud, local rotational velocity was simulated using 3D-FEM to predict the cell flow in this region (Lawton et al. 2013). Detailed aspects of amphibian neurulation were also simulated in full 3D in Chen and Brodland's (2008) work by inputting various mechanical parameters from physical measurements. Then the effect of mechanical parameters (e.g. stress) on formation of the normal phenotype was investigated. In my case, FEM was mainly used to determine the patterns of dorsal closing force during neural tube closure, and to make comparisons between *Kumba* mutant and wild-type based on differences in morphology and elasticity of the NP that had been measured in the embryo itself.

From the modelling of the closing tube, it was found that the closing force peaks at the closure point and diminishes with distance towards both ends. However, it was striking that the rate of decline in closing force was greater towards the unclosed end, equivalent to more caudal levels of the PNP, than towards the already closed end, equivalent to the more rostral, closed neural tube. This is consistent with the marked attenuation along the PNP of the effects of incision (e.g. re-opening of the NFs) that was observed in Chapter 3. The lesser degree of attenuation of the closing force in the already closed neural tube region suggests that force is to some extent 'stored' (potential energy) within the closed neural tube structure. This seems to be dissipated gradually, as development proceeds (e.g. with continued cell proliferation and onset of neuronal differentiation) within the increasingly mature post-closure neural tube.

The dorsolateral bending degree of the NP was compared before and after

closure in the FEM simulation, using the same method as the measurement of DLHP bending degree in embryo sections. Strikingly, the NP after simulated closure showed a 1.6-fold increase in bending degree compared to the NP before closure. This result is consistent, in a converse manner, with the finding in Chapter 3 of a significant reduction in DLHP bending degree after NT incision. Collectively, these results suggest that the dorsal closing force plays an important role in DLHP formation. Furthermore, it was found that a larger closing force is required to achieve closure in a neural tube with smaller NP width, therefore modelling the effect of the NP width difference between *Kumba* mutants and wild-type. The modelling result also identified a relationship between NP thickness and force required for closure. The thicker the NP, the more mechanically unfavourable was tube closure.

Most strikingly, FEM provided evidence to support the idea that the elasticity difference between the NPs of *Kumba* mutant and wild-type embryos may play a major role in determining the failure of closure to progress in mutants. NP elasticity in the FEM simulation was increased from 100 to 300 Pa, equivalent to the approximate NP elasticity values of the dorsal NP region in wild-type and the *Kumba* mutant embryos at ss16-17, respectively (see Chapter 5). This caused the closing force required for closure to increase linearly, strong evidence for an important role of a more elastic (stiffer) NP hampering closure in the *Kumba* mutant.

It is interesting to compare the magnitude of the effects on dorsal closing force of varying the NP elasticity, basal NP width or NP thickness in the FEM simulation (Table 6.1). Provided that dorsal closing force has a linearly proportional relationship with NP elasticity, increasing elasticity from 134 (measured wild-type data) to 349 Pa (measured mutant data), for the dorsal NP of ss16-17, resulted in a 2.6-fold linear increase in closing force. When basal NP width was reduced by approximately 25%, as observed in *Kumba* mutant embryos compared with wild-type, the dorsal closing force showed a 1.7-fold increase. In contrast, 17% decrease in NP thickness, as observed in *Kumba* mutant compared with wild-type, caused reduction in the required dorsal closing force by 24%. Therefore, it can be concluded that increased NP stiffness is likely to be the main mechanical cause of failure of neural tube closure in *Kumba* mutant embryos. In addition, the effects of basal NP width, NP thickness, and NP elasticity on dorsal closing force could be all combined together as they were compared in a mutually exclusive manner. Hence, multiplying each fold change of the closing force for the three different variables (the last

column in Table 6.1) resulted in a 3.28-fold total increase in the dorsal closing force for mutant compared with wild-type. Similar results were observed when the dorsal closing force was calculated after all the NP variables were all combined for each genotype; the required dorsal closing force for mutant was 3.31 times as large as that of wild-type (the last row in Table 6.1)

NP variables	WT			Mut			Mut/WT (fold change)		
	Msrd	Input	F (pN)	Msrd	Input	F (pN)	Msrd	Input	F
Basal width (μm) (with fixed input values of 30 μm NP thickness, 100 Pa Elasticity)	304	266.7	220	192	199.7	366	0.63	0.75	1.66
Thickness (μm) (with fixed input values of 199.7 μm basal width, 100 Pa Elasticity)	33.0	30	366	28.8	25	280	0.87	0.83	0.76
Elasticity (Pa) (with fixed input values of 199.7 μm basal width, 30 μm NP thickness)	134	134	490	349	349	1280	2.60	2.60	2.60
Total (variables combined)		combined	294.8		combined	977.2			3.31

Table 6.1 Comparison of basal NP width, NP thickness, and NP elasticity between measured values, simulation-input, and dorsal closing forces for wild-type and mutant.

'Msrd' represents experimentally measured mean values. 'Input' represents the value inputted for simulation. 'F' represents the required dorsal closing force (mean value of the valid data zone) after simulation with 'Input' values. The column 'F' in 'Mut/WT' represents the rate of increase/decrease (fold change) in the required dorsal closing force.

When neural tube closure was simulated, it was assumed that the NP is in a static state in terms of its growth. In reality, however, the NP is constantly growing through cell proliferation, and altering its shape, for example by extension in the longitudinal axis, through convergent extension and cell rearrangements (Ybot-Gonzalez et al. 2007b). Therefore, a more accurate, life-like simulation would be to include such NP growth and shape change during the simulated closure progression. Based on Miller et al.'s (1999) finding that cell proliferation drives folding of avian gut endoderm, it can be expected that such proliferation, in balance with apoptosis, affects internal stress of the tissue, which might lead to elasticity change. Similarly, the balance between proliferation and

apoptosis will also determine the growth rate of basal NP width and NP thickness. The lack of any allowance for growth in the present study is a limitation, and may have caused inaccuracies in the calculated dorsal closing force profiles.

A further limitation of the FEM simulation was its focus solely on the dynamics of the NP, with no consideration given to possible mechanical roles of the paraxial mesoderm or surface ectoderm, which are attached to the NP in the embryo. The paraxial mesoderm does not appear to be essential for NP bending as ablation experiments to remove it from the adjacent neural folds do not prevent NT closure from continuing, in either mouse or chick (Alvarez and Schoenwolf 1992; Ybot-Gonzalez et al. 2002).

A possible mechanical role of the surface ectoderm in neural tube closure is more controversial. In the chick embryo, it was suggested that elevation of the neural folds might result from expansion of the surface ectoderm, which could 'push' the neural folds towards the midline (Hackett et al. 1997), although expansion of surface ectoderm is actually minimal at spinal levels (Moury and Schoenwolf 1995). In an amphibian study, a mechanical role of the surface ectoderm in neural tube closure was also proposed, based on the successful neural fold elevation after eliminating apical constriction of NP cells by colchicine treatment that inhibits microtubules (Brun and Garson 1983). On the other hand, work in the mouse (Ybot-Gonzalez et al. 2002), chick (Hackett et al. 1997) and urodele amphibians (Jacobson and Moury 1995), all demonstrate that only a very narrow fragment of surface ectoderm needs to be attached to the neural plate to allow DLHP formation and neural tube closure. Such fragments of ectoderm have no lateral anchoring points against which to develop a push force, making unlikely a mechanical role of surface ectoderm in generating DLHPs. This suggests that the surface ectoderm may have a bio-molecular signalling function in DLHP formation, rather than a purely mechanical role.

In conclusion, the FEM simulation described in this chapter, despite some limitations in the scope of its modelling, has nevertheless provided a meaningful approach to understanding neural tube closure. In particular, it has provided insight into the force relationship between various features of the closing NP (elasticity, basal width, thickness), and the force required to achieve closure. The parallels between findings from the FEM simulations and the results of biological experiments in the thesis are striking, and can form the basis for future analysis of neurulation mechanisms in mammalian embryos.

7. General discussion

7.1. Summary of the findings

Neural tube closure is a multifactorial event in which various bio-molecular pathways drive bending of the neuroepithelium in a mechanically coordinated manner. While the link between bio-molecular signals and both midline and dorsolateral bending has been subjected to experimental analysis (Patten and Placzek 2002; Ybot-Gonzalez et al. 2002; Ybot-Gonzalez et al. 2007a), the mechanical basis of these bending events is largely unknown. In this thesis, the physical origins of dorsolateral NP bending were investigated by mechanical manipulation (i.e. incision) of the NT, which provided insight into the force relationships within and around the closing NT.

After incision of the most recently closed NT roof, the NFs were observed to spring apart immediately, with a significant reduction in the bending degree of both DLHPs and MHP post-incision. This 'unbending' response was largest at the closing PNP level and smallest at the more caudally open PNP level. This result suggests that NP bending is largely elastic, and that there exists force derived from the recently closed NT (i.e. the NP pull-in force), which acts to bring the NFs into apposition in the open region of the PNP.

NP cells were also observed to respond mechanically to the incision: cells in the dorsal NP region showed the greatest reduction in their dorso-ventral curvature after incision, becoming straighter, an effect that was most marked at the closing level where DLHPs are present, and less marked at the open/caudal level where DLHPs are absent. In unincised embryos, nuclei were more elongated in the dorsal NP of the closing level than at the open level, suggesting that cells become increasingly compact in the dorsal NP as DLHPs form. After incision, nuclei became even more elongated, with the most marked effect in the dorsal NP of the closing level. The NF-associated surface ectoderm was found to reduce its medio-lateral length following incision, suggesting that it had become stretched during DLHP formation, and that elastic recoil occurred upon incision. Hence, the NP pull-in force stretches the dorsal NF whose NP cells are already crowded (with elongated nuclei). Upon incision, the NF returns to its unstretched conformation, with further NP cells crowding and even greater nuclear elongation.

The incision effects were also tested on *Kumba* mutant embryos developing spina bifida. The elastic re-opening of the NFs was significantly larger in the mutant than

in the wild-type, suggesting that there exists more tension at the closing PNP level of the mutant. In order to identify a possible cause for this, NP elasticity was measured by AFM at the onset of the spinal neurulation defect, and the elasticity of the mutant NP was found to be larger than that of the wild-type. FEM simulation of closure further revealed that increased NP stiffness causes an escalation of the dorsal closing force required for NT closure. This suggests that increased NP stiffness leads to the dominance of the elastic recovery force of the NP (acting outward) over the NP pull-in force (Figure 7.1 D), which is presumed to be the main mechanical cause of spinal neurulation failure in the mutant embryos. In the cell shape analysis, cells were straighter and nuclei were more circular in the mutant NP than in wild-type or heterozygous embryos. These results confirm that cells vary their curvature depending on tissue bending, and that cell-packing in the dorsal NP is closely associated with DLHP formation.

7.2. Origin of the NP pull-in force

My experiments suggest that NP pull-in force originates in the recently closed NT region, and this force is approximately balanced by an equal and opposite elastic recovery force, in a static mode of NT closure. Most importantly, for NT closure to progress, the NP pull-in force must surpass the recovery force at the rostral end of the PNP. An important question for further research relates to the 'motor' that drives continuing closure, and that perhaps generates extra NP pull-in force in addition to the pre-existing NP pull-in force created from the closed NT region. It has been conventionally suggested that medial movement of the SE contributes to NP bending and NT closure (Alvarez and Schoenwolf 1992), but the study by Ybot-Gonzalez et al. (2002) study suggests that a physical role of the SE in NP bending is negligible since DLHP still forms when most of the SE is removed. A prediction would be, therefore, that if the NT is incised and then embryos continue to develop in culture, any further DLHP formation and PNP closure may be inhibited. Experiments of this sort are now beginning in our lab.

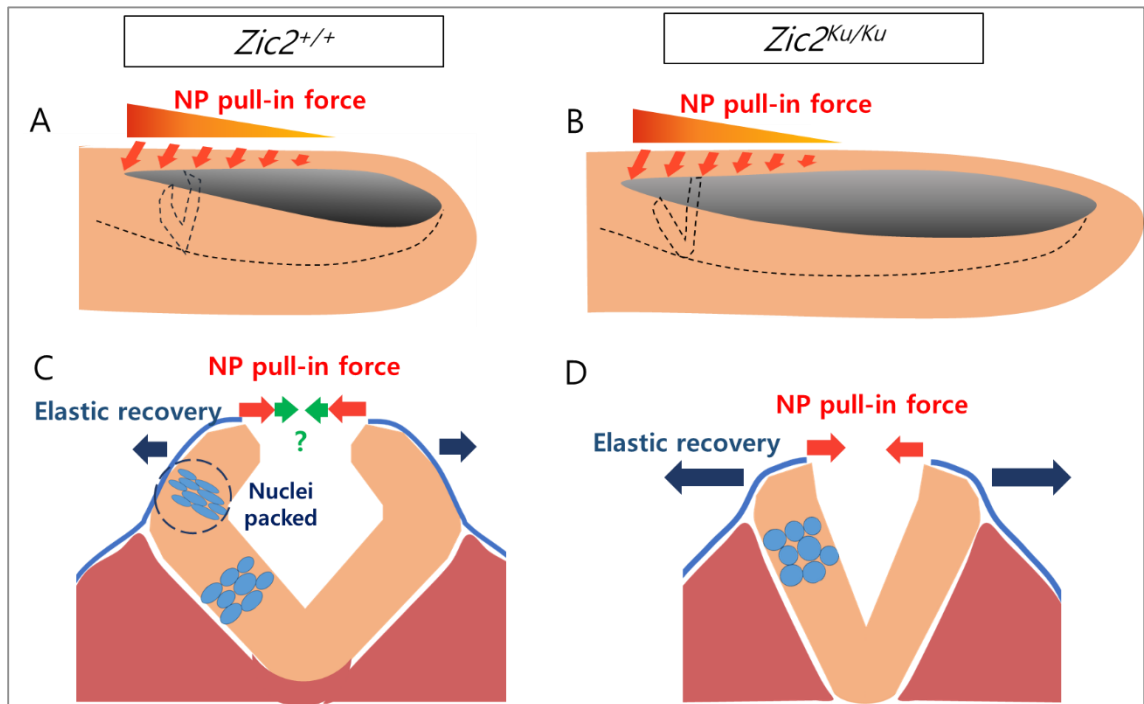


Figure 7.1 Summary diagram of force relationships in *Zic2*^{+/+} and *Zic2*^{Ku/Ku} embryos.

(A-B) Embryo views of *Zic2*^{+/+} (A) and spina bifida (enlarged PNP) developing *Zic2*^{Ku/Ku} (B). For both, closure point driven NP pull-in force peaks at the PNP closing point, and diminishes with distance towards the caudal end.

(C-D) Transverse views of *Zic2*^{+/+} (C) and spina bifida developing *Zic2*^{Ku/Ku} (D) at the closing level of the PNP (dashed-lined shapes in (A,B)). In *Zic2*^{+/+} (C), NP pull-in force is balanced by elastic recovery force, in a static state of NT closure, but an additional force (green arrows), which might act as a motor for continuing closure of the NT, is required for progression of NT closure. Increased cell (nuclear) packing particularly in the dorsal NP of *Zic2*^{+/+}, compared with *Zic2*^{Ku/Ku}, is thought to be involved in DLHP formation. On the other hand, in *Zic2*^{Ku/Ku} (D), elastic recovery force is greater than NP pull-in force due to increased Young's modulus (stiffness) of the NP, which implies that *Zic2*^{Ku/Ku} requires larger dorsal closing force than *Zic2*^{+/+}. Therefore, the closing process is arrested in *Zic2*^{Ku/Ku}.

7.3. Motors for continuing closure of the neural tube

In line with my finding, a recent study by Hashimoto et al. (2015) showed direct evidence that dorsal fusion process (“zippering”) itself provides a motive force for neural tube closure. In their 2015 study, once chordate embryos are cut into anterior and posterior halves just before the initiation of zippering, which occurs in a unidirectional manner (i.e. posterior-to-anterior), the posterior cut half goes through full zippering whereas the anterior cut half remains completely open. More importantly, the same study revealed that neural/epidermal junctions just ahead of the closing point become sequentially shortened, with concomitant myosin activation/enrichment in this region, which is driven by an upregulated Rho/ROCK signaling pathway. It was also confirmed through a laser-ablation experiment that junctional tension is most condensed on the myosin-enriched region just ahead of the advancing zipper; recoiling velocities are the fastest in this region. These results directly address the possibility that ROCK-dependent myosin contraction in the neural/epidermal junctions could be the fundamental force for continuing NT closure in vertebrate as well. However, while *Ciona intestinalis* neural tube closure was completely halted by treatment with blebbistatin, H1152 (specific inhibitor of ROCK), and y27632, posterior neurulation in mice embryos was not affected by blebbistatin treatment, but by y27632 treatment (Escuin et al. unpublished). These contrary results strongly suggest that there might be other zippering mechanisms involved in mouse neurulation than myosin-driven contraction.

Extrusion of the dorsal midline cells in the rostrally closed regions may act as a driving motor for continuing closure of the neural tube. Cell extrusion is a homeostatic process that pushes out excess cells from tissues, to avoid overcrowding. During formation of the dorsal thorax in *Drosophila*, the two lateral dorsal wing disc epithelial sheets progress towards each other, and fuse in the dorsal midline. It was found that basal delamination of cells then occurs in the dorsal midline, by cells sensing the local crowding in this region (Marinari et al. 2012). Similar cell extrusion was also reported in Madin-Darby canine kidney (MDCK) cells, except that cells were extruded apically from an epithelial sheet that was caused experimentally to become overcrowded (Eisenhoffer et al. 2012). The dorsal NFs contain crowded cells, as demonstrated in my study, and so fusion of these folds could lead to transient cell crowding in the NT roof. Moreover, apoptotic cell death is plentiful in the region immediately overlying the recently closed NT (Yamaguchi et al. 2011). Although this cell death is not essential for closure (Massa et

al. 2009), it seems likely to represent cells recently extruded from the NT. Cell extrusion was not investigated in the present study, but if this extrusion really happens at the dorsal midline of the neural tube, it can be conceived that non-extruded cells will extend themselves towards each other to fill up the space where the extruded cells previously reside. And the 'patch-up' force might also act on the adjacent dorsal tissue of the caudally open PNP region, facilitating the apposition of the NFs. Therefore, it will be important to verify the functional importance of cell extrusion in the dorsal NT midline as a future experiment.

Contraction of a circumferential actin 'cable' in the apical region of the NP could be another motor for continuing closure, and perhaps for NP pull-in force enhancement. Dorsal closure in *Drosophila* and wound healing in several animal groups progresses by formation and contraction of an actin cable (Martin and Lewis 1992) located in the apices of cells bordering the epithelial edge. In a similar way, closure of the NT could allow rapid assembly of a circumferential actin cable, which then, by contracting, could provide NP pull-in force. PNP closure continues in the presence of the actin disassembling drug Cytochalasin D (Ybot-Gonzalez and Copp 1999), but at the concentrations used, this drug might not be able to disassemble a relatively massive actin cable. Investigation of the role of this mechanism in NT closure would be an important future experiment.

7.4. Mechanical mechanisms of DLHP formation

The present study demonstrated that the NP pull-in force partly contributes to dorsolateral NP bending, from both the morphology and the FEM analyses. However, these analysis results do not fully prove that the NP pull-in force is the motive force for DLHP formation. Then, the nucleus circularity study revealed that nuclei are more packed in wild-type NP than in *Kumba* NP (DLHP absent), suggesting possible roles of cell-packing in DLHP formation. In accordance with this result, recent unpublished work in our lab also confirmed that cells in the NP are translocating in a ventral-to-dorsal direction during neural tube closure, forming a biphasic structure that comprises of a denser dorsolateral component and a less dense ventromedial component. Collectively, these results suggest that there is an inhomogeneity in cell density along the dorso-ventral axis of the NP, which becomes most prominent in the phase-transition site (i.e. the dorsolateral region). From mechanical perspectives, this kind of inconsistency in a

material could be considered as a mechanical discontinuity, where stress can be concentrated upon the exertion of external force, and therefore this will be the site where mechanical distortion would happen. For this reason, 'buckling' happens in the dorsolateral region of the NP, forming the DLHP during neural tube closure.

7.5. Molecular basis of the increased stiffness in *Kumba* mutant embryos

Recent work from our lab (Escuin et al. unpublished) shows that actomyosin is apically accumulated in the NP of *Kumba* mutant embryos compared to the wild-type. Moreover, Blebbistatin (a myosin-II inhibitor) is able to both normalise the distribution of actomyosin, and also partially rescue the spinal neurulation defect. If the increase in NP stiffness of the mutant embryos is related to the apical accumulation of actomyosin, perhaps NP stiffness of the mutant embryos could be brought back to the level of wild-type after Blebbistatin treatment in culture. This experiment would be perfectly feasible to do, and was considered for this thesis, but could not be carried out due to shortage of time.

Intermediate filaments could be another candidate for a stiffness regulator. During reactive gliosis in the rodent retina, it was found that stiffening of glial cells is closely related to density of intermediate filaments (Lu et al. 2011). However, the roles of microtubules in stiffness regulation are controversial. In a *Xenopus* dorsal isolate, treatment with nocodazole (microtubule depolymeriser) causes an increase in stiffness via an upregulated RhoA pathway (Zhou et al. 2010). In contrast, the same drug treatment on pillar cells of the mouse cochlea result in a considerable decrease in stiffness (Szarama et al. 2012), suggesting that response to microtubule depolymerisation is dependent on the tissue context. As a future experiment, therefore, it would be important to compare intermediate filament and microtubule expressions between the wild-type and *Kumba* mutant NPs.

7.6. Application of NT closing mechanisms to other morphogeneses

Similar morphogenesis as vertebrate neurulation can be seen in other organisms. During ventral enclosure of *C.elegans*, the anterior pair of leading cells among ventral

cells start extending towards the ventral midline by their actin-rich filopodia protrusions (Williams-Masson et al. 1997). Once the contact of the leading cells is made, posterior ventral cells also spread towards the ventral midline, forming an actin-ring in their free edges (Williams-Masson et al. 1997). Then, the bilateral contact of ventral cells completes ventral enclosure.

Similarly, during dorsal closure of *Drosophila*, the epithelial opening is known to be sealed by contraction of supracellular actin cables, and by apical constriction of amnioserosal cells, which generates pulling forces (Kiehart et al. 2000).

While the previous two closure processes are mainly driven by contraction of a circumferential actin ring/cable (i.e. a “purse-string” mechanism), secondary palate development in vertebrates involves a zippering process, closely resembling neural tube closure. At the time of palatal shelf elevation, the pair of the palatal shelves reorientate from vertical to horizontal positions. Then, the paired shelves grow and fuse at the midline, beginning from the middle region in the antero-posterior axis. When the fusion happens and propagates towards the both ends, it appears in the frontal sections of the developing palate that the palatal shelves adopt a flat-tube-like shape in the nasal chamber (Bush and Jiang 2012). Since the palatal shelves are also initially flat before their outgrowths and elevation, it can be expected that, during the zippering process, a similar type of force as NP pull-in force will be exerted on the closing side of the palatal shelves. In order to test this hypothesis, however, elastic properties of the tissue (e.g. a recoil after incision) should be examined first.

7.7. Limitations of the studies

Several limitations of the experimental approaches in this thesis have been discussed in the relevant chapters, and are not repeated here. Mechanisms of neural tube closure were explained in the present study, using perception of force balance between the NP pull-in force and an elastic recovery force of the NP. However, since the NP pull-in force can be defined only when a pre-closed point exists in the antero-posterior axis, closure 1, in which the flat NP comes into its first contact, cannot be explained by this theory. Therefore, another mechanical model is required to understand closure 1, in addition to convergent extension based models (Ybot-Gonzalez et al. 2007b).

The AFM method was very valuable in identifying the NP elasticity abnormality

in *Kumba* mutant embryos, but it would be more useful if it could be applied to whole embryos, and particularly in a repeated manner on single embryos. For example, in the *Kumba* experiments with Blebbistatin mentioned above, the ideal approach would be to measure elasticity by AFM in the same embryo before and after the addition of Blebbistatin to the culture medium. Further development of the AFM technique would be needed to achieve such repeated measurements.

In the modelling studies, FEM was used to simulate closure of an open NT in 3D. However, post-incision NP behavior (springing-apart of the NFs) was not modelled in this thesis due to the complications of applying an incision condition in 3D. However, in FEM-based studies of anterior intestinal portal epithelia in chick heart tube (Varner and Taber 2012) and early embryonic chick brain (Xu et al. 2010), to investigate the mechanical outcome of incision, tissues were modelled in 2D so that an incision condition could be implemented in a simple form. In my modelling, the closed NT could be simplified as a 2D model, by considering only its transverse section appearance. Then, it would be intriguing to compare the degree of springing-apart after incision between the NP with high elastic modulus and the one with low elastic modulus.

7.8. Conclusion

Neural tube closure comprises both elastic and plastic bending of the NP. This suggests a new way of thinking about neurulation, which has long been considered a problem of the gradual elevation of NFs through plastic changes occurring endogenously within the NP, or through forces originating from tissues lateral to the NFs (e.g. surface ectoderm). Apposition of the NFs is an elastic process exogenously driven by the NP pull-in force that originates from the most recently closed point. DLHP formation, however, is a partially plastic process, closely associated with cell packing within the dorsal NP as an endogenous event. In the *Kumba* mutant embryos, a stiffer NP and the absence of cell-packing in the dorsal NP region are perhaps the main mechanical causes of spinal neurulation failure; the NP with higher elastic modulus requires a larger amount of NP pull-in force for NT closure, and the lack of cell-packing in the dorsal region accompanies absence of DLHP formation.

8. Bibliography

- Alvarez, I. S. and Schoenwolf, G. C. (1992). Expansion of surface epithelium provides the major extrinsic force for bending of the neural plate. *J Exp Zool* **261** (3):340-8.
- Amir, A., Babaeipour, F., McIntosh, D. B., Nelson, D. R., and Jun, S. (2014). Bending forces plastically deform growing bacterial cell walls. *Proc Natl Acad Sci U S A* **111** (16):5778-83.
- Aruga, J., Nagai, T., Tokuyama, T., Hayashizaki, Y., Okazaki, Y., Chapman, V. M., and Mikoshiba, K. (1996). The mouse zic gene family. Homologues of the Drosophila pair-rule gene odd-paired. *J Biol Chem* **271** (2):1043-7.
- Aruga, J., Yokota, N., Hashimoto, M., Furuichi, T., Fukuda, M., and Mikoshiba, K. (1994). A novel zinc finger protein, zic, is involved in neurogenesis, especially in the cell lineage of cerebellar granule cells. *J Neurochem* **63** (5):1880-90.
- Barrett, K., Leptin, M., and Settleman, J. (1997). The Rho GTPase and a putative RhoGEF mediate a signaling pathway for the cell shape changes in Drosophila gastrulation. *Cell* **91** (7):905-15.
- Bellaiche, Y., Gho, M., Kaltschmidt, J. A., Brand, A. H., and Schweisguth, F. (2001). Frizzled regulates localization of cell-fate determinants and mitotic spindle rotation during asymmetric cell division. *Nature cell biology* **3** (1):50-7.
- Boresi, Arthur P. and Schmidt, Richard J. (2003). *Advanced mechanics of materials*. 6th ed. New York: John Wiley & Sons.
- Botto, L. D., Moore, C. A., Khoury, M. J., and Erickson, J. D. (1999). Neural-tube defects. *N Engl J Med* **341** (20):1509-19.
- Bower, C., D'Antoine, H., and Stanley, F. J. (2009). Neural tube defects in Australia: trends in encephaloceles and other neural tube defects before and after promotion of folic acid supplementation and voluntary food fortification. *Birth Defects Res A Clin Mol Teratol* **85** (4):269-73.
- Bronner, M. E. and LeDouarin, N. M. (2012). Development and evolution of the neural crest: an overview. *Dev Biol* **366** (1):2-9.
- Brook, F. A., Shum, A. S., Van Straaten, H. W., and Copp, A. J. (1991). Curvature of the caudal region is responsible for failure of neural tube closure in the curly tail (ct) mouse embryo. *Development* **113** (2):671-8.
- Brun, R. B. and Garson, J. A. (1983). Neurulation in the Mexican salamander (*Ambystoma mexicanum*): a drug study and cell shape analysis of the epidermis and the neural plate. *Journal of embryology and experimental morphology* **74**:275-95.
- Bush, J. O. and Jiang, R. (2012). Palatogenesis: morphogenetic and molecular mechanisms of secondary palate development. *Development* **139** (2):231-43.
- Camerer, E., Barker, A., Duong, D. N., Ganesan, R., Kataoka, H., Cornelissen, I., Darragh, M. R., et al. (2010). Local protease signaling contributes to neural tube closure in the mouse embryo. *Dev Cell* **18** (1):25-38.
- Cayuso, J., Ulloa, F., Cox, B., Briscoe, J., and Marti, E. (2006). The Sonic hedgehog pathway independently controls the patterning, proliferation and survival of neuroepithelial

- cells by regulating Gli activity. *Development* **133** (3):517-28.
- Chang, Y. C., Nalbant, P., Birkenfeld, J., Chang, Z. F., and Bokoch, G. M. (2008). GEF-H1 couples nocodazole-induced microtubule disassembly to cell contractility via RhoA. *Mol Biol Cell* **19** (5):2147-53.
- Chen, X. and Brodland, G. W. (2008). Multi-scale finite element modeling allows the mechanics of amphibian neurulation to be elucidated. *Phys Biol* **5** (1):015003.
- Chen, Z. F. and Behringer, R. R. (1995). twist is required in head mesenchyme for cranial neural tube morphogenesis. *Genes Dev* **9** (6):686-99.
- Chung, A. C., Katz, D., Pereira, F. A., Jackson, K. J., DeMayo, F. J., Cooney, A. J., and O'Malley, B. W. (2001). Loss of orphan receptor germ cell nuclear factor function results in ectopic development of the tail bud and a novel posterior truncation. *Mol Cell Biol* **21** (2):663-77.
- Copp, A. J. (2005). Neurulation in the cranial region--normal and abnormal. *J Anat* **207** (5):623-35.
- Copp, A. J., Checiu, I., and Henson, J. N. (1994). Developmental basis of severe neural tube defects in the loop-tail (Lp) mutant mouse: use of microsatellite DNA markers to identify embryonic genotype. *Dev Biol* **165** (1):20-9.
- Copp, A. J. and Greene, N. D. (2013). Neural tube defects--disorders of neurulation and related embryonic processes. *Wiley Interdiscip Rev Dev Biol* **2** (2):213-27.
- Copp, A. J., Greene, N. D., and Murdoch, J. N. (2003). The genetic basis of mammalian neurulation. *Nature reviews. Genetics* **4** (10):784-93.
- Copp, A.J. and Greene, N.D.E. (2010). Genetics and development of neural tube defects. *The Journal of pathology* **220** (2):217-30.
- Costa, M., Sweeton, D., and Wieschaus, E. 1993. Gastrulation in Drosophila: Cellular Mechanisms of Morphogenetic Movements. In *The development of drosophila melanogaster*, edited by Alfonso Martinez Arias Michael bate, 425-65. New York: Cold Spring Harbor Laboratory Press.
- Curtin, J. A., Quint, E., Tshipouri, V., Arkell, R. M., Cattanch, B., Copp, A. J., Henderson, D. J., et al. (2003). Mutation of Celsr1 disrupts planar polarity of inner ear hair cells and causes severe neural tube defects in the mouse. *Current biology : CB* **13** (13):1129-33.
- Davidson, L. A., Koehl, M. A., Keller, R., and Oster, G. F. (1995). How do sea urchins invaginate? Using biomechanics to distinguish between mechanisms of primary invagination. *Development* **121** (7):2005-18.
- Dawes-Hoang, R. E., Parmar, K. M., Christiansen, A. E., Phelps, C. B., Brand, A. H., and Wieschaus, E. F. (2005). folded gastrulation, cell shape change and the control of myosin localization. *Development* **132** (18):4165-78.
- Del Bene, F. (2011). Interkinetic nuclear migration: cell cycle on the move. *The EMBO journal* **30** (9):1676-7.
- Efremov, Y. M., Pukhlyakova, E. A., Bagrov, D. V., and Shaitan, K. V. (2011). Atomic force microscopy of living and fixed Xenopus laevis embryos. *Micron* **42** (8):840-52.
- Eiraku, M., Takata, N., Ishibashi, H., Kawada, M., Sakakura, E., Okuda, S., Sekiguchi, K., Adachi, T., and Sasai, Y. (2011). Self-organizing optic-cup morphogenesis in three-dimensional

- culture. *Nature* **472** (7341):51-6.
- Eisenhoffer, G. T., Loftus, P. D., Yoshigi, M., Otsuna, H., Chien, C. B., Morcos, P. A., and Rosenblatt, J. (2012). Crowding induces live cell extrusion to maintain homeostatic cell numbers in epithelia. *Nature* **484** (7395):546-9.
- Elms, P., Siggers, P., Napper, D., Greenfield, A., and Arkell, R. (2003). Zic2 is required for neural crest formation and hindbrain patterning during mouse development. *Dev Biol* **264** (2):391-406.
- Ettensohn, C.A. (1984). Primary Invagination of the Vegetal Plate During Sea Urchin Gastrulation. *American Zoologist* **24** (3):571-88.
- Fox, D. T. and Peifer, M. (2007). Abelson kinase (Abl) and RhoGEF2 regulate actin organization during cell constriction in Drosophila. *Development* **134** (3):567-78.
- Gaston-Massuet, C., Henderson, D. J., Greene, N. D., and Copp, A. J. (2005). Zic4, a zinc-finger transcription factor, is expressed in the developing mouse nervous system. *Dev Dyn* **233** (3):1110-5.
- Gaston-Massuet, Calres (2004). Role of Zic genes during neurulation. *UCL*.
- Golden, J. A. and Chernoff, G. F. (1993). Intermittent pattern of neural tube closure in two strains of mice. *Teratology* **47** (1):73-80.
- Grinberg, I., Northrup, H., Ardinger, H., Prasad, C., Dobyns, W. B., and Millen, K. J. (2004). Heterozygous deletion of the linked genes ZIC1 and ZIC4 is involved in Dandy-Walker malformation. *Nat Genet* **36** (10):1053-5.
- Gubb, D. and Garcia-Bellido, A. (1982). A genetic analysis of the determination of cuticular polarity during development in Drosophila melanogaster. *Journal of embryology and experimental morphology* **68**:37-57.
- Guo, N., Hawkins, C., and Nathans, J. (2004). Frizzled6 controls hair patterning in mice. *Proc Natl Acad Sci U S A* **101** (25):9277-81.
- Gustavsson, P., Greene, N. D., Lad, D., Pauws, E., de Castro, S. C., Stanier, P., and Copp, A. J. (2007). Increased expression of Grainyhead-like-3 rescues spina bifida in a folate-resistant mouse model. *Hum Mol Genet* **16** (21):2640-6.
- Hackett, D. A., Smith, J. L., and Schoenwolf, G. C. (1997). Epidermal ectoderm is required for full elevation and for convergence during bending of the avian neural plate. *Dev Dyn* **210** (4):397-406.
- Haigo, S. L., Hildebrand, J. D., Harland, R. M., and Wallingford, J. B. (2003). Shroom induces apical constriction and is required for hinge-point formation during neural tube closure. *Current biology : CB* **13** (24):2125-37.
- Harden, N. (2002). Signaling pathways directing the movement and fusion of epithelial sheets: lessons from dorsal closure in Drosophila. *Differentiation* **70** (4-5):181-203.
- Harris, A. R. and Charras, G. T. (2011). Experimental validation of atomic force microscopy-based cell elasticity measurements. *Nanotechnology* **22** (34):345102.
- Harris, M. J. and Juriloff, D. M. (2007). Mouse mutants with neural tube closure defects and their role in understanding human neural tube defects. *Birth Defects Res A Clin Mol Teratol* **79** (3):187-210.
- Harris, M. J. and Juriloff, D. M. (2010). An update to the list of mouse mutants with neural tube

- closure defects and advances toward a complete genetic perspective of neural tube closure. *Birth Defects Res A Clin Mol Teratol* **88** (8):653-69.
- Hashimoto, H., Robin, F. B., Sherrard, K. M., and Munro, E. M. (2015). Sequential contraction and exchange of apical junctions drives zippering and neural tube closure in a simple chordate. *Dev Cell* **32** (2):241-55.
- Hildebrand, J. D. (2005). Shroom regulates epithelial cell shape via the apical positioning of an actomyosin network. *Journal of cell science* **118** (Pt 22):5191-203.
- Hildebrand, J. D. and Soriano, P. (1999). Shroom, a PDZ domain-containing actin-binding protein, is required for neural tube morphogenesis in mice. *Cell* **99** (5):485-97.
- Homem, C. C. and Peifer, M. (2008). Diaphanous regulates myosin and adherens junctions to control cell contractility and protrusive behavior during morphogenesis. *Development* **135** (6):1005-18.
- Houtmeyers, R., Souopgui, J., Tejpar, S., and Arkell, R. (2013). The ZIC gene family encodes multi-functional proteins essential for patterning and morphogenesis. *Cell Mol Life Sci* **70** (20):3791-811.
- Jacobson, A. G. and Moury, J. D. (1995). Tissue boundaries and cell behavior during neurulation. *Dev Biol* **171** (1):98-110.
- Jacobson, A. G., Oster, G. F., Odell, G. M., and Cheng, L. Y. (1986). Neurulation and the cortical tractor model for epithelial folding. *Journal of embryology and experimental morphology* **96**:19-49.
- Juriloff, D. M. and Harris, M. J. (2012). A consideration of the evidence that genetic defects in planar cell polarity contribute to the etiology of human neural tube defects. *Birth Defects Res A Clin Mol Teratol* **94** (10):824-40.
- Kee, N., Wilson, N., De Vries, M., Bradford, D., Key, B., and Cooper, H. M. (2008). Neogenin and RGMa control neural tube closure and neuroepithelial morphology by regulating cell polarity. *The Journal of neuroscience : the official journal of the Society for Neuroscience* **28** (48):12643-53.
- Keller, R., Shook, D., and Skoglund, P. (2008). The forces that shape embryos: physical aspects of convergent extension by cell intercalation. *Phys Biol* **5** (1):015007.
- Kibar, Z., Vogán, K. J., Groulx, N., Justice, M. J., Underhill, D. A., and Gros, P. (2001). Ltap, a mammalian homolog of Drosophila Strabismus/Van Gogh, is altered in the mouse neural tube mutant Loop-tail. *Nat Genet* **28** (3):251-5.
- Kiehart, D. P., Galbraith, C. G., Edwards, K. A., Rickoll, W. L., and Montague, R. A. (2000). Multiple forces contribute to cell sheet morphogenesis for dorsal closure in Drosophila. *J Cell Biol* **149** (2):471-90.
- Knight, M. M., van de Breevaart Bravenboer, J., Lee, D. A., van Osch, G. J., Weinans, H., and Bader, D. L. (2002). Cell and nucleus deformation in compressed chondrocyte-alginate constructs: temporal changes and calculation of cell modulus. *Biochim Biophys Acta* **1570** (1):1-8.
- Kolsch, V., Seher, T., Fernandez-Ballester, G. J., Serrano, L., and Leptin, M. (2007). Control of Drosophila gastrulation by apical localization of adherens junctions and RhoGEF2. *Science* **315** (5810):384-6.

- Kosodo, Y., Suetsugu, T., Suda, M., Mimori-Kiyosue, Y., Toida, K., Baba, S. A., Kimura, A., and Matsuzaki, F. (2011). Regulation of interkinetic nuclear migration by cell cycle-coupled active and passive mechanisms in the developing brain. *The EMBO journal* **30** (9):1690-704.
- Lan, Z. J., Gu, P., Xu, X., Jackson, K. J., DeMayo, F. J., O'Malley, B. W., and Cooney, A. J. (2003). GDNF-dependent repression of BMP-15 and GDF-9 mediates gamete regulation of female fertility. *The EMBO journal* **22** (16):4070-81.
- Lane, M. C., Koehl, M. A., Wilt, F., and Keller, R. (1993). A role for regulated secretion of apical extracellular matrix during epithelial invagination in the sea urchin. *Development* **117** (3):1049-60.
- Lawson, A., Anderson, H., and Schoenwolf, G. C. (2001). Cellular mechanisms of neural fold formation and morphogenesis in the chick embryo. *Anat Rec* **262** (2):153-68.
- Lawton, A. K., Nandi, A., Stulberg, M. J., Dray, N., Sneddon, M. W., Pontius, W., Emonet, T., and Holley, S. A. (2013). Regulated tissue fluidity steers zebrafish body elongation. *Development* **140** (3):573-82.
- Lee, J. Y., Marston, D. J., Walston, T., Hardin, J., Halberstadt, A., and Goldstein, B. (2006). Wnt/Frizzled signaling controls C. elegans gastrulation by activating actomyosin contractility. *Current biology : CB* **16** (20):1986-97.
- Lemire, R. J. (1969). Variations in development of the caudal neural tube in human embryos (Horizons XIV-XXI). *Teratology* **2** (4):361-9.
- Leptin, M. and Grunewald, B. (1990). Cell shape changes during gastrulation in Drosophila. *Development* **110** (1):73-84.
- Li, Z., Ren, A., Zhang, L., Ye, R., Li, S., Zheng, J., Hong, S., Wang, T., and Li, Z. (2006). Extremely high prevalence of neural tube defects in a 4-county area in Shanxi Province, China. *Birth Defects Res A Clin Mol Teratol* **76** (4):237-40.
- Louise Meyer, R., Zhou, X., Tang, L., Arpanaei, A., Kingshott, P., and Besenbacher, F. (2010). Immobilisation of living bacteria for AFM imaging under physiological conditions. *Ultramicroscopy* **110** (11):1349-57.
- Lu, X., Borchers, A. G., Jolicoeur, C., Rayburn, H., Baker, J. C., and Tessier-Lavigne, M. (2004). PTK7/CCK-4 is a novel regulator of planar cell polarity in vertebrates. *Nature* **430** (6995):93-8.
- Lu, Y. B., Iandiev, I., Hollborn, M., Korber, N., Ulbricht, E., Hirrlinger, P. G., Pannicke, T., et al. (2011). Reactive glial cells: increased stiffness correlates with increased intermediate filament expression. *Faseb j* **25** (2):624-31.
- Marinari, E., Mehonic, A., Curran, S., Gale, J., Duke, T., and Baum, B. (2012). Live-cell delamination counterbalances epithelial growth to limit tissue overcrowding. *Nature* **484** (7395):542-5.
- Marti, E., Takada, R., Bumcrot, D. A., Sasaki, H., and McMahon, A. P. (1995). Distribution of Sonic hedgehog peptides in the developing chick and mouse embryo. *Development* **121** (8):2537-47.
- Martin, P. and Lewis, J. (1992). Actin cables and epidermal movement in embryonic wound healing. *Nature* **360** (6400):179-83.

- Massa, V., Savery, D., Ybot-Gonzalez, P., Ferraro, E., Rongvaux, A., Cecconi, F., Flavell, R., Greene, N. D., and Copp, A. J. (2009). Apoptosis is not required for mammalian neural tube closure. *Proc Natl Acad Sci U S A* **106** (20):8233-8.
- Messier, P. E. and Auclair, C. (1973). Inhibition of nuclear migration in the absence of microtubules in the chick embryo. *Journal of embryology and experimental morphology* **30** (3):661-71.
- Miller, S. A., Adornato, M., Briglin, A., Cavanaugh, M., Christian, T., Jewett, K., Michaelson, C., et al. (1999). Domains of differential cell proliferation suggest hinged folding in avian gut endoderm. *Dev Dyn* **216** (4-5):398-410.
- Mitchell, L. E. (2005). Epidemiology of neural tube defects. *American journal of medical genetics. Part C, Seminars in medical genetics* **135C** (1):88-94.
- Montcouquiol, M., Rachel, R. A., Lanford, P. J., Copeland, N. G., Jenkins, N. A., and Kelley, M. W. (2003). Identification of Vangl2 and Scrb1 as planar polarity genes in mammals. *Nature* **423** (6936):173-7.
- Morris-Wiman, J. and Brinkley, L. L. (1990). Changes in mesenchymal cell and hyaluronate distribution correlate with in vivo elevation of the mouse mesencephalic neural folds. *Anat Rec* **226** (3):383-95.
- Morris, G. M. and Solursh, M. (1978). Regional differences in mesenchymal cell morphology and glycosaminoglycans in early neural-fold stage rat embryos. *Journal of embryology and experimental morphology* **46**:37-52.
- Moury, J. D. and Schoenwolf, G. C. (1995). Cooperative model of epithelial shaping and bending during avian neurulation: autonomous movements of the neural plate, autonomous movements of the epidermis, and interactions in the neural plate/epidermis transition zone. *Dev Dyn* **204** (3):323-37.
- Murdoch, J. N., Damrau, C., Paudyal, A., Bogani, D., Wells, S., Greene, N. D., Stanier, P., and Copp, A. J. (2014). Genetic interactions between planar cell polarity genes cause diverse neural tube defects in mice. *Dis Model Mech* **7** (10):1153-63.
- Murdoch, J. N., Doudney, K., Paternotte, C., Copp, A. J., and Stanier, P. (2001a). Severe neural tube defects in the loop-tail mouse result from mutation of Lpp1, a novel gene involved in floor plate specification. *Hum Mol Genet* **10** (22):2593-601.
- Murdoch, J. N., Henderson, D. J., Doudney, K., Gaston-Massuet, C., Phillips, H. M., Paternotte, C., Arkell, R., Stanier, P., and Copp, A. J. (2003). Disruption of scribble (Scrb1) causes severe neural tube defects in the circletail mouse. *Hum Mol Genet* **12** (2):87-98.
- Murdoch, J. N., Rachel, R. A., Shah, S., Beermann, F., Stanier, P., Mason, C. A., and Copp, A. J. (2001b). Circletail, a new mouse mutant with severe neural tube defects: chromosomal localization and interaction with the loop-tail mutation. *Genomics* **78** (1-2):55-63.
- Nagai, T., Aruga, J., Minowa, O., Sugimoto, T., Ohno, Y., Noda, T., and Mikoshiba, K. (2000). Zic2 regulates the kinetics of neurulation. *Proc Natl Acad Sci U S A* **97** (4):1618-23.
- Nagai, T., Aruga, J., Takada, S., Gunther, T., Sporle, R., Schughart, K., and Mikoshiba, K. (1997). The expression of the mouse Zic1, Zic2, and Zic3 gene suggests an essential role for Zic genes in body pattern formation. *Dev Biol* **182** (2):299-313.
- Nance, J. and Priess, J. R. (2002). Cell polarity and gastrulation in *C. elegans*. *Development* **129**

(2):387-97.

- Nikolaidou, K. K. and Barrett, K. (2004). A Rho GTPase signaling pathway is used reiteratively in epithelial folding and potentially selects the outcome of Rho activation. *Current biology : CB* **14** (20):1822-6.
- Nolan, P. M., Peters, J., Strivens, M., Rogers, D., Hagan, J., Spurr, N., Gray, I. C., et al. (2000). A systematic, genome-wide, phenotype-driven mutagenesis programme for gene function studies in the mouse. *Nat Genet* **25** (4):440-3.
- O'Rahilly, R. and Muller, F. (2002). The two sites of fusion of the neural folds and the two neuropores in the human embryo. *Teratology* **65** (4):162-70.
- Odell, G. M., Oster, G., Alberch, P., and Burnside, B. (1981). The mechanical basis of morphogenesis. I. Epithelial folding and invagination. *Dev Biol* **85** (2):446-62.
- Park, T. J., Haigo, S. L., and Wallingford, J. B. (2006). Ciliogenesis defects in embryos lacking inturned or fuzzy function are associated with failure of planar cell polarity and Hedgehog signaling. *Nat Genet* **38** (3):303-11.
- Patten, I. and Placzek, M. (2002). Opponent activities of Shh and BMP signaling during floor plate induction in vivo. *Current biology : CB* **12** (1):47-52.
- Pruyne, D., Evangelista, M., Yang, C., Bi, E., Zigmond, S., Bretscher, A., and Boone, C. (2002). Role of formins in actin assembly: nucleation and barbed-end association. *Science* **297** (5581):612-5.
- Razani, B., Engelman, J. A., Wang, X. B., Schubert, W., Zhang, X. L., Marks, C. B., Macaluso, F., et al. (2001). Caveolin-1 null mice are viable but show evidence of hyperproliferative and vascular abnormalities. *J Biol Chem* **276** (41):38121-38.
- Reddy, J. N. (1993). *An introduction to the finite element method*. 2nd ed, McGraw-Hill series in mechanical engineering. New York: McGraw-Hill.
- Ridley, A. J. (2001). Rho GTPases and cell migration. *Journal of cell science* **114** (Pt 15):2713-22.
- Roelink, H., Porter, J. A., Chiang, C., Tanabe, Y., Chang, D. T., Beachy, P. A., and Jessell, T. M. (1995). Floor plate and motor neuron induction by different concentrations of the amino-terminal cleavage product of sonic hedgehog autoproteolysis. *Cell* **81** (3):445-55.
- Rogers, S. L., Wiedemann, U., Hacker, U., Turck, C., and Vale, R. D. (2004). Drosophila RhoGEF2 associates with microtubule plus ends in an EB1-dependent manner. *Current biology : CB* **14** (20):1827-33.
- Roh-Johnson, M. and Goldstein, B. (2009). In vivo roles for Arp2/3 in cortical actin organization during *C. elegans* gastrulation. *Journal of cell science* **122** (Pt 21):3983-93.
- Rolo, A., Skoglund, P., and Keller, R. (2009). Morphogenetic movements driving neural tube closure in *Xenopus* require myosin IIB. *Dev Biol* **327** (2):327-38.
- Rugendorff, Astrid, Younossi-Hartenstein, Amelia, and Hartenstein, Volker (1994). Embryonic origin and differentiation of the *Drosophila* heart. *Roux's archives of developmental biology* **203** (5):266-80.
- Sagot, I., Rodal, A. A., Moseley, J., Goode, B. L., and Pellman, D. (2002). An actin nucleation mechanism mediated by Bni1 and profilin. *Nature cell biology* **4** (8):626-31.

- Sauer, F. C. (1935). Mitosis in the neural tube. *The Journal of Comparative Neurology* **62** (2):377-405.
- Sausedo, R. A., Smith, J. L., and Schoenwolf, G. C. (1997). Role of nonrandomly oriented cell division in shaping and bending of the neural plate. *The Journal of Comparative Neurology* **381** (4):473-88.
- Sawyer, J. M., Harrell, J. R., Shemer, G., Sullivan-Brown, J., Roh-Johnson, M., and Goldstein, B. (2010). Apical constriction: a cell shape change that can drive morphogenesis. *Dev Biol* **341** (1):5-19.
- Schoenwolf, G. C. (1984). Histological and ultrastructural studies of secondary neurulation in mouse embryos. *Am J Anat* **169** (4):361-76.
- Schoenwolf, G. C. (1988). Microsurgical analyses of avian neurulation: separation of medial and lateral tissues. *The Journal of Comparative Neurology* **276** (4):498-507.
- Schoenwolf, G. C. and Alvarez, I. S. (1991). Specification of neuroepithelium and surface epithelium in avian transplantation chimeras. *Development* **112** (3):713-22.
- Schoenwolf, G. C., Folsom, D., and Moe, A. (1988). A reexamination of the role of microfilaments in neurulation in the chick embryo. *Anat Rec* **220** (1):87-102.
- Schoenwolf, G. C. and Franks, M. V. (1984). Quantitative analyses of changes in cell shapes during bending of the avian neural plate. *Dev Biol* **105** (2):257-72.
- Schoenwolf, G. C. and Sheard, P. (1990). Fate mapping the avian epiblast with focal injections of a fluorescent-histochemical marker: ectodermal derivatives. *J Exp Zool* **255** (3):323-39.
- Schoenwolf, G. C. and Smith, J. L. (2000). Mechanisms of neurulation. *Methods Mol Biol* **136**:125-34.
- Severson, A. F., Baillie, D. L., and Bowerman, B. (2002). A Formin Homology protein and a profilin are required for cytokinesis and Arp2/3-independent assembly of cortical microfilaments in *C. elegans*. *Current biology : CB* **12** (24):2066-75.
- Shum, A. S. and Copp, A. J. (1996). Regional differences in morphogenesis of the neuroepithelium suggest multiple mechanisms of spinal neurulation in the mouse. *Anat Embryol (Berl)* **194** (1):65-73.
- Smith, J. L. and Schoenwolf, G. C. (1987). Cell cycle and neuroepithelial cell shape during bending of the chick neural plate. *Anat Rec* **218** (2):196-206.
- Smith, J. L. and Schoenwolf, G. C. (1988). Role of cell-cycle in regulating neuroepithelial cell shape during bending of the chick neural plate. *Cell and tissue research* **252** (3):491-500.
- Smith, J. L. and Schoenwolf, G. C. (1989). Notochordal induction of cell wedging in the chick neural plate and its role in neural tube formation. *J Exp Zool* **250** (1):49-62.
- Smith, J. L. and Schoenwolf, G. C. (1991). Further evidence of extrinsic forces in bending of the neural plate. *J Comp Neurol* **307** (2):225-36.
- Smith, J. L., Schoenwolf, G. C., and Quan, J. (1994). Quantitative analyses of neuroepithelial cell shapes during bending of the mouse neural plate. *J Comp Neurol* **342** (1):144-51.
- Solursh, M. and Morriss, G. M. (1977). Glycosaminoglycan synthesis in rat embryos during the formation of the primary mesenchyme and neural folds. *Dev Biol* **57** (1):75-86.

- Somlyo, A. P. and Somlyo, A. V. (2003). Ca²⁺ sensitivity of smooth muscle and nonmuscle myosin II: modulated by G proteins, kinases, and myosin phosphatase. *Physiol Rev* **83** (4):1325-58.
- Srinivas, S., Watanabe, T., Lin, C. S., William, C. M., Tanabe, Y., Jessell, T. M., and Costantini, F. (2001). Cre reporter strains produced by targeted insertion of EYFP and ECFP into the ROSA26 locus. *BMC Dev Biol* **1**:4.
- Stein, K. F. and Rudin, I. A. (1953). DEVELOPMENT OF MICE HOMOZYGOUS FOR THE GENE FOR LOOPTAIL. *Journal of Heredity* **44** (2):59-69.
- Suzuki, M., Hara, Y., Takagi, C., Yamamoto, T. S., and Ueno, N. (2010). MID1 and MID2 are required for *Xenopus* neural tube closure through the regulation of microtubule organization. *Development* **137** (14):2329-39.
- Sweeton, D., Parks, S., Costa, M., and Wieschaus, E. (1991). Gastrulation in *Drosophila*: the formation of the ventral furrow and posterior midgut invaginations. *Development* **112** (3):775-89.
- Szarama, K. B., Gavara, N., Petralia, R. S., Kelley, M. W., and Chadwick, R. S. (2012). Cytoskeletal changes in actin and microtubules underlie the developing surface mechanical properties of sensory and supporting cells in the mouse cochlea. *Development* **139** (12):2187-97.
- Thibault, Guillaume, Devic, Caroline, Horn, Jean-François, Fertil, Bernard, Sequeira, Jean, and Mari, Jean-Luc (2008). Classification of cell nuclei using shape and texture indexes.
- Umeshima, H., Hirano, T., and Kengaku, M. (2007). Microtubule-based nuclear movement occurs independently of centrosome positioning in migrating neurons. *Proc Natl Acad Sci U S A* **104** (41):16182-7.
- van Straaten, H. W., Hekking, J. W., Consten, C., and Copp, A. J. (1993). Intrinsic and extrinsic factors in the mechanism of neurulation: effect of curvature of the body axis on closure of the posterior neuropore. *Development* **117** (3):1163-72.
- Varner, V. D. and Taber, L. A. (2012). Not just inductive: a crucial mechanical role for the endoderm during heart tube assembly. *Development* **139** (9):1680-90.
- Vinson, C. R. and Adler, P. N. (1987). Directional non-cell autonomy and the transmission of polarity information by the frizzled gene of *Drosophila*. *Nature* **329** (6139):549-51.
- Wang, J., Hamblet, N. S., Mark, S., Dickinson, M. E., Brinkman, B. C., Segil, N., Fraser, S. E., Chen, P., Wallingford, J. B., and Wynshaw-Boris, A. (2006a). Dishevelled genes mediate a conserved mammalian PCP pathway to regulate convergent extension during neurulation. *Development* **133** (9):1767-78.
- Wang, Y., Guo, N., and Nathans, J. (2006b). The role of Frizzled3 and Frizzled6 in neural tube closure and in the planar polarity of inner-ear sensory hair cells. *The Journal of neuroscience : the official journal of the Society for Neuroscience* **26** (8):2147-56.
- Warr, N., Powles-Glover, N., Chappell, A., Robson, J., Norris, D., and Arkell, R. M. (2008). Zic2-associated holoprosencephaly is caused by a transient defect in the organizer region during gastrulation. *Hum Mol Genet* **17** (19):2986-96.
- Wiebe, C. and Brodland, G. W. (2005). Tensile properties of embryonic epithelia measured using a novel instrument. *J Biomech* **38** (10):2087-94.

- Williams-Masson, E. M., Malik, A. N., and Hardin, J. (1997). An actin-mediated two-step mechanism is required for ventral enclosure of the *C. elegans* hypodermis. *Development* **124** (15):2889-901.
- Wong, L. L. and Adler, P. N. (1993). Tissue polarity genes of *Drosophila* regulate the subcellular location for prehair initiation in pupal wing cells. *J Cell Biol* **123** (1):209-21.
- Xu, G., Kemp, P. S., Hwu, J. A., Beagley, A. M., Bayly, P. V., and Taber, L. A. (2010). Opening angles and material properties of the early embryonic chick brain. *J Biomech Eng* **132** (1):011005.
- Yamaguchi, Y., Shinotsuka, N., Nonomura, K., Takemoto, K., Kuida, K., Yosida, H., and Miura, M. (2011). Live imaging of apoptosis in a novel transgenic mouse highlights its role in neural tube closure. *J Cell Biol* **195** (6):1047-60.
- Ybot-Gonzalez, P., Cogram, P., Gerrelli, D., and Copp, A. J. (2002). Sonic hedgehog and the molecular regulation of mouse neural tube closure. *Development* **129** (10):2507-17.
- Ybot-Gonzalez, P. and Copp, A. J. (1999). Bending of the neural plate during mouse spinal neurulation is independent of actin microfilaments. *Dev Dyn* **215** (3):273-83.
- Ybot-Gonzalez, P., Gaston-Massuet, C., Girdler, G., Klingensmith, J., Arkell, R., Greene, N. D., and Copp, A. J. (2007a). Neural plate morphogenesis during mouse neurulation is regulated by antagonism of Bmp signalling. *Development* **134** (17):3203-11.
- Ybot-Gonzalez, P., Savery, D., Gerrelli, D., Signore, M., Mitchell, C. E., Faux, C. H., Greene, N. D., and Copp, A. J. (2007b). Convergent extension, planar-cell-polarity signalling and initiation of mouse neural tube closure. *Development* **134** (4):789-99.
- Zamir, E. A. and Taber, L. A. (2004). On the effects of residual stress in microindentation tests of soft tissue structures. *J Biomech Eng* **126** (2):276-83.
- Zhao, Q., Behringer, R. R., and de Crombrughe, B. (1996). Prenatal folic acid treatment suppresses acrania and meroanencephaly in mice mutant for the *Cart1* homeobox gene. *Nat Genet* **13** (3):275-83.
- Zheng, L., Zhang, J., and Carthew, R. W. (1995). *frizzled* regulates mirror-symmetric pattern formation in the *Drosophila* eye. *Development* **121** (9):3045-55.
- Zhou, J., Kim, H. Y., and Davidson, L. A. (2009). Actomyosin stiffens the vertebrate embryo during crucial stages of elongation and neural tube closure. *Development* **136** (4):677-88.
- Zhou, J., Kim, H. Y., Wang, J. H., and Davidson, L. A. (2010). Macroscopic stiffening of embryonic tissues via microtubules, RhoGEF and the assembly of contractile bundles of actomyosin. *Development* **137** (16):2785-94.
- Zohn, I. E. and Sarkar, A. A. (2012). Does the cranial mesenchyme contribute to neural fold elevation during neurulation? *Birth Defects Res A Clin Mol Teratol* **94** (10):841-8.